On the interplay between steering and interlayer diffusion in Cu(001) homoepitaxy

Frits L. W. Rabbering

Samenstelling promotiecommissie:

prof. dr. Klaus Boller, voorzitter
prof. dr. ir. Bene Poelsema
dr. ir. H. Wormeester
prof. dr. T. Michely
prof. dr. J. Wollschläger
dr. ing. A.J.H.M. Rijnders
prof. dr. ir. H.J.W. Zandvliet

This thesis is the result of work performed in the MESA+ Institute for Nanotechnology, Solid State Physics group, Faculty of Science and Technology at the University of Twente, The Netherlands.

This work has been funded by the "Stichting Fundamenteel Onderzoek der Materie" (FOM).

F.L.W. Rabbering
On the interplay between steering and interlayer diffusion in Cu(001) homoepitaxy
ISBN 978-90-365-2627-2

Published by the Solid State Physics Group, University of Twente

Printed in The Netherlands by PrintPartners Ipskamp B.V., Enschede

Author email: `Frits@bracque.nl`

ON THE INTERPLAY BETWEEN STEERING AND INTERLAYER DIFFUSION IN Cu(001) HOMOEPITAXY

Proefschrift

ter verkrijging van
de graad van doctor aan de Universiteit Twente,
op gezag van de rector magnificus,
prof. dr. W.H.M. Zijm,
volgens besluit van het College voor Promoties
in het openbaar te verdedigen
op donderdag 29 februari 2008 om 16.45 uur

door

Frederik Lambertus Wilhelmus Rabbering
geboren op 29 december 1975
te Ermelo

Dit proefschrift is goedgekeurd door de promotor:
prof. dr. ir. Bene Poelsema
en door de assistent-promotor:
dr. ir. Herbert Wormeester

Hallo opa,

Op de foto weer een stukje mooi schotland. De plek waar de foto van genomen is heet: "Rusten ben dankbaar". De oude weg was vroeger erg stijl en vele hadden moeite om de top te bereiken.

Hier in Glasgow is momenteel geen sneeuw meer te bekennen. Zonnetje schijnt weer lekker.

Helaas moet ik examens leren, maar misschien heb ik aan het eind van de maand nog tijd om te genieten. Groet Frits

SOP

Opa Gebbing
Kees van Dongenpleingg
4707 HVE Roosendaal
NETHERLANDS

GLASGOW MAIL CENTRE
18 JAN 2001

Lyrical
SCOTLAND

BY AIR MAIL
Royal Mail
30p

LS249 Glen Croe,
Loch Restil & the Rest & Be Thankful.

Photo: Allan Wright © Cauldron Press Ltd Castle Douglas DG7 3NB. 01644 470260 Web site: www.lyricalscotland.com

CONTENTS

CHAPTER 1

Introduction

1.1 The interplay of steering and diffusion

In 1966 Nieuwenhuizen reported a new type of thin film growth: depositing atoms at oblique incidence resulted in the growth of a columnar structure. These columns have an inclination angle with the normal of the substrate that depends on the polar angle of the deposition beam [1]. The column formation at oblique incidence deposition has been attributed to shadow effects: incoming particles are assumed to follow ballistic trajectories: As a result the loss of flux on the shadow sides is compensated by an enhanced flux on the illuminated sides. Nowadays, oblique incidence deposition has matured to a widely used deposition technique for the preparation of thin films with a wide variety of magnetic and optical properties [2–4].

Meanwhile, in 1997, the group of professor Poelsema started fundamental research on the influence of the polar deposition angle on growth. Grazing incidence deposition of a few tens of monolayers of Cu on Cu(001) was also found to result in a change in film morphology compared to normal incidence deposition [5–8]. At normal incidence a growing Cu film exhibits the fourfold symmetry imposed by the Cu(001) substrate. For grazing incidence deposition, the fourfold symmetry has vanished and only mirror symmetry with respect to the plane of incidence of the deposition beam is found.

Slightly later, in a seminal experiment, it was shown that the change in symmetry already occurred in the submonolayer growth stage [6]. Only one monolayer high adatom islands are formed in this stage, having an average elongation perpendicular to the deposition plane. It cannot be explained with shadow effects, because this

would only result in a change of the center of mass position of the adatom islands towards the deposition beam.

The experimental observation was qualitatively explained with an attractive interaction between the incoming particle and the substrate. The attractive interactions change the impact position of a particle compared to that expected from a ballistic trajectory. Protrusions on the surface are attractors, focussing the atoms from its shadow to its top side. The resulting change of the incident flux of atoms was coined steering.

In the past, dispersive forces were simulated with a Lennard Jones (12,6) potential. Sanders and DePristo used the potential to study impact positions of gas phase adatoms on crystal surfaces [9]. Recently, the strength of the long range part of this potential was made subject to discussion. Amar proposes a five times weaker strength, which will enhance the steering effect [10]. Yu and Amar also showed that incoming gas phase adatoms which have an impact position at the step have a significant change of upfunneling, i.e. are incorporated on top of the island instead of funneling down [11].

Steering leads thus to an enhanced deposition of adatoms on already existing adatom islands, especially near the illuminated side. An Ehrlich Schwoebel barrier on the edge limits interlayer diffusion, causing this surplus of adatoms to diffuse more equally across the top of these islands before descending. As a result of this interplay between steering and interlayer transport, elongated growth of the islands occur.

The anisotropy in the submonolayer growth stage as a result of this interplay is still small. But when the islands grow bigger, steering gets more effective. At the same time, the changing shape of the stepedges of the islands affects the interlayer transport. The heterogeneity of the flux changes dramatically with time as also the morphology of a film grown changes with increasing deposition. This results in a very different morphology at grazing incidence deposition compared to normal incidence deposition.

1.2 This thesis

The aim of this thesis is to obtain a more quantitative understanding of the effect of the interplay of steering at oblique incidence deposition and interlayer transport on film morphology. Steering depends on the dipolar interaction strength between gas phase atoms and the surface. A large part of the presented work is dedicated to establish reasonable values for interlayer mass transport and a determination of the dipolar interaction strength.

The work in this thesis is based on a comparison of experimental results obtained

with high resolution surface diffraction with results from simulations with a kinetic Monte Carlo (kMC) program. Additional experiments on the deposition of Cu on Cu(001) are done. The used setup is described in the next chapter.

The steering effect depends both on the angle of incidence of the growth beam as well as on the velocity of the atoms. Therefore the possibility to create a rather monochromatic beam of Cu atoms and the possibility to vary their velocity was studied. The design and development of a velocity selected deposition beam is described in chapter 3 of this thesis.

Chapter 4 describes extensively the basics of the kMC program and the evaluation of trajectories of incident particles. To describe multilayer homoepitaxial growth on Cu(001) a precise determination of the additional diffusion barriers for interlayer mass transport has to be done. In chapter 5 a determination of the activation barrier for two interlayer mass transport pathways is described. Considered are the barriers associated with the straight $\langle 110 \rangle$ step edge and the via kink positions in this step edge. The value of these barriers ultimately determines the surface roughness. The surface roughness after deposition of 1 and 2 ML of Cu at normal incidence for temperatures between 200 and 290K was recorded with Thermal Energy Atom Scattering (TEAS). The experimentally found roughness was compared to values from a simulation in which the two barrier heights are varied.

The elongation of adatom islands observed with high resolution Low Energy Electron Diffraction (HR-LEED) is a direct result of dipolar interaction. The amount of elongation is used in chapter 6 to determine the strength of the dipolar interaction. The elongation of adatom islands as a function of coverage is recorded with HR-LEED. The growth was simulated with the kMC program described in chapter 4 with the correct interlayer barriers found in chapter 5 and with varying strength of the dipolar interaction. A comparison of the experimental and simulated data allows to determine the dipolar interaction strength.

Multilayer growth at grazing incidence is the subject of chapter 7. With the ingredients for the interlayer mass transport and the dipolar interaction strength derived in chapters 5 and 6 an overall good agreement between results from diffraction measurements and simulations is obtained. This agreement allows to use the simulation results to study the effect of steering at grazing incidence for multilayer growth in more detail. As a function of temperature and polar angle of deposition, a widely varying morphology is observed. This involves clear ripple formation, a 90° change in orientation of the elongated features as well as extreme roughening of the surface.

CHAPTER 2

Experimental Techniques

The experiments were performed with an Ultra High Vacuum (UHV) system that has been used for 3 previous PhD projects. Details of this system and the (diffraction) techniques used can be found in the PhD thesis of Jorritsma [5], Van Dijken [8] and Ovsyanko [12]. The data acquisition by Spot Profile Analysis Low Energy Electron Diffraction (SPA-LEED) has been described by Esser [13]. A short description of the main features of the experimental set-up is given below.

2.1 UHV

An ultra-high vacuum chamber with a base pressure of less than 10^{-10} mbar was used in the experiments. This pressure was obtained through a combination of a turbo molecular pump and a liquid nitrogen cooled titanium sublimation pump. Figure 2.1 shows a schematic drawing of the apparatus. It includes the following techniques:

- Spot Profile Analysis Low Energy Electron Diffraction (SPA-LEED), manufactured by Omicron (Germany).
- Thermal Energy Atom Scattering (TEAS), home built with a Balzers QMG112 Quadrupole Mass Spectrometer as detector.
- Auger Electron Spectroscopy (AES), manufactured by Riber.
- Argon ion gun, manufactured by Leybold (IQ12/63). A focus lens and high pressure stage were added to the ion gun.

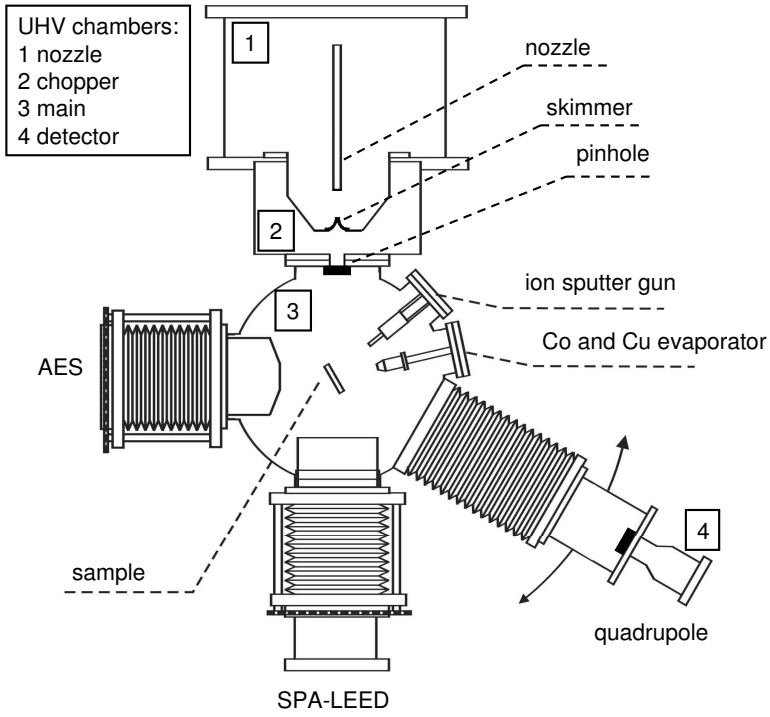

Figure 2.1: Schematic illustration of the experimental set-up.

- Quadrupole Mass Spectrometer (QMS), manufactured by Riber.
- Home built copper and cobalt evaporators.
- Velocity selector for deposition of a monochromatic beam of particles. This device is extensively described in chapter 3.
- The sample temperature can be varied by cooling (liquid nitrogen) and heating facilities. This gives access to temperatures roughly from 100 K up to 900 K.

2.2 TEAS

Thermal Energy Atom Scattering (TEAS) was used to *in-situ* monitor the deposition of material deposited close to normal incidence. TEAS is a diffraction technique that uses a monochromatic beam of He atoms. The kinetic energy of these atoms is equal to the thermal energy, that is set by the temperature of the nozzle. In the set-up used, the nozzle is at room temperature, which gives an energy of 67 meV. This

is equivalent to a wavelength of 0.56 Å. The low energy of the He atoms allows them to approach the surface up to a distance of 3-4 Å[14–16], before they are reflected as a result of repulsive interactions. The scattered He atoms will have an angular distribution pattern determined by the atomic structure and for close packed metal surfaces as the Cu(001) case mostly by the morphology of the surface. TEAS is very surface sensitive and the intensity distribution of the scattered beam can be described well with the kinematic approach for diffraction, see also [17, 18].

The He beam is produced through adiabatic expansion of He gas in a nozzle with an aperture of 30 μm. Part of the He beam will pass through a skimmer to the adjoining vacuum chamber called the chopper chamber, see fig. 2.1. The skimmer has an aperture of 0.21 mm that selects the central part of the beam. The beam is further collimated with an aperture separating the chopper chamber from the main chamber. This aperture with a diameter of 0.2 mm determines the size and the angular spread of the beam. It is positioned 57 mm away from the nozzle and 200 mm in front of the substrate. The beam has thus a divergence angle of 0.2°. After diffraction at the substrate surface, the intensity of the scattered He at a specific angle is monitored by a quadrupole. This quadrupole is positioned in a differentially pumped chamber separated from the main chamber by an aperture with a diameter of 2 mm at a distance of 600 mm from the substrate. A bellow allows to move the quadrupole detector in the horizontal plane over an angle of 34°. For a sufficient signal at the quadrupole, a pressure in the nozzle above 1 bar is required. The He background pressure in the main chamber is kept within bounds by a differential pumping system between nozzle and substrate. Table 2.1 outlines the pumping speeds and pressures in these chambers during TEAS operation.

Chamber	Pumping speed (l/s)	Pressure (mbar)
Nozzle	3000	$3.0{\cdot}10^{-4}$
Chopper	150	$4.1{\cdot}10^{-6}$
Main	220	$6.8{\cdot}10^{-9}$
Detector	150	$< 4.0{\cdot}10^{-11}$ (He partial pressure)

Table 2.1: Pressures in the various vacuum chambers during TEAS operation. Listed is also the pumping speed of the pump used to evacuate the chamber. Helium pressure in the nozzle is 2.2 bar.

2.3 SPA-LEED

Low energy electron diffraction was used as principal technique for the investigation of the surface morphology of patterned Cu(001) surfaces. With high resolution

Low-Energy Electron Diffraction (LEED) one obtains information regarding symmetry, surface unit cell dimensions, periodicity of structure, atomic roughness of a surface and facets. The diffraction pattern contains information averaged over a macroscopic surface area of about 1 mm^2 (the size of the electron spot on the surface). High resolution diffraction is used in this work in order to obtain information on morphology with a length scale up to several hundreds of atoms.

To obtain sufficient surface sensitivity the energy of probing electrons is typically chosen between 50 and 500 eV. A price has to be paid by the occurence of multiple scattering effects on the intensity of the diffraction peaks. To extract information from electron diffraction patterns there are two major methods known as the kinematic and the dynamic approach: The kinematic theory is an approximation of the complete scattering process as a single scattering event. The dynamic theory accounts for multiple scattering events and involves the total scattering intensity as a function of energy [19, 20]. These multiple scattering effects are strongly electron energy dependent. However, the angular dependence of this multiple scattering feature is only small. Therefore, the shape of the diffraction peak at a specific energy can be quite well described with a kinematic approach [21]. This shape contains information on the surface morphology. As a consequence only the diffraction spot positions and their intensity profile $I(k_{\|})$ at a specific energy are analyzed.

Inelastic scattering of electrons breaks the phase and k-vector relations between the incoming and outgoing electron. This process thus limits the probing depth in electron diffraction. For the low energy regime, up to 300 eV, only electrons scattered from the first few surface layers will be scattered elastically and contribute to the diffraction pattern. More detailed information can be found in the cited literature sources [19, 20, 22, 23].

In the middle of the eighties of the last century Henzler and coworkers started the development a new instrument for increased resolution Low Energy Electron Diffraction [24]. The advantage of a High Resolution Low Energy Electron Diffraction (HR-LEED) apparatus over a conventional LEED set-up is the possibility of spot profile analysis. The transfer width of the used commercial High Resolution LEED - Omicron SPA-LEED amounts to about 1200 Å (the transfer width of a conventional LEED set-up is approximately one order of magnitude smaller).

A schematic drawing of the cross-section of the SPA-LEED instrument is shown in fig 2.2. The SPA-LEED can be operated in two modes. In the first mode like with conventional LEED, the diffraction pattern is visible on a fluorescent screen. This visual mode is mainly used to adjust the position of the sample in front of the SPA-LEED and to find the approximate focus conditions for the electron beam. In the second mode, the diffraction pattern is swept across a channeltron positioned

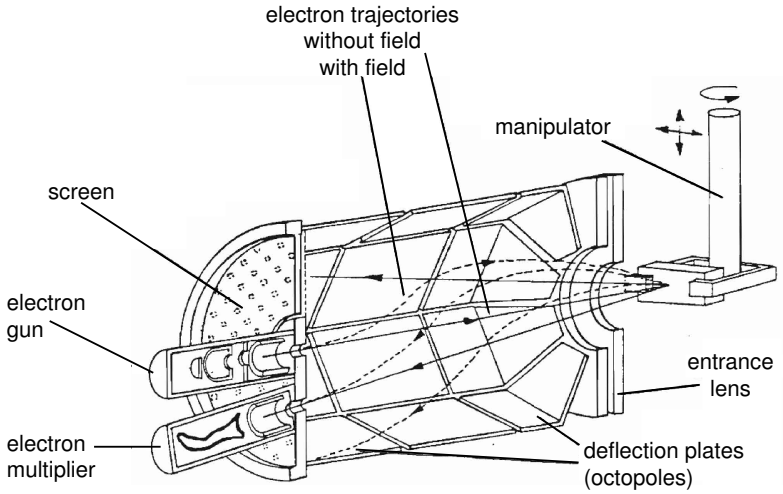

Figure 2.2: Schematic SPA-LEED set-up: the electron gun, the channeltron detector, the deflection unit, and the sample position are indicated. The path of the electrons from the gun to the detector is illustrated. The angle of incidence is varied by the voltage at the octupole deflection unit. The spot position on the sample remains constant during scanning.

behind a narrow aperture. This provides both a high angular resolution and a high dynamic range. Instead of a mechanical rotation of the sample, the reflected electron beam is moved across the entrance aperture of the channeltron by means of octupole fields. The octupole also deflects the incident electron beam on the surface before the reflected beam is recorded at the channeltron (see fig. 2.2). The octupole is constructed in such a way that during a scan the electron beam stays at the same position on the sample. The angle of incidence of the electron will change during a scan. The angle of incidence is also electron energy dependent, which makes this set-up unsuitable for evaluation of electron diffraction intensities using dynamic LEED theory. Irrespective of the high resolution, the big advantage of the SPA-LEED compared with a conventional LEED is the possibility to determine quantitatively the scattered electron intensity distribution.

The octupole deflection system does show several non-linearities like cushion and barrel distortion [13]. Especially for larger voltages on the octupole, i.e. outside the first Brillouin zone, the distortions can be quite dramatic. However, the measurements presented here are performed in proximity of the specular reflected beam and therefore do not suffer from these deformations. The sample is typically placed in such a position that the specularly reflected beam is monitored by the channeltron without a voltage on the octupole.

2.4 Sample Preparation

The Cu-sample is cut out of a Cu-crystal rod along the (001)-plane with an accuracy of $\leq$ 0.1°, after which it is mechanically polished. Prior to mounting into the UHV system the sample is heated to 900 K in a H_2/Ar environment for a few days. This treatment results in a very low level of sulphur in the sample. The sample is further cleaned in vacuum, initially by prolonged sputtering with 800 eV Ar^+ ions at 600 K. When no impurities can be detected anymore on the surface with AES, the sample is simultaneously sputtered and annealed at 900 K. This treatment is needed to prevent sulphur, which segregates to the surface at temperatures above 800 K, of pinning of the step edges. When the sulphur impurity level on the surface is below the detection limit of AES ($\leq$ 1%), an average terrace width of $\gtrsim$ 1000 Å is usually obtained with this treatment. The average terrace width has been deduced from the width of the anti-phase specular SPA-LEED peak. After every growth experiment, the grown layer is completely removed by sputtering at 500 K. After this sputtering process the sample is annealed during a prolonged period to 750 K. This procedure results in reproducible conditions for all growth experiments.

CHAPTER 3

Design and realization of a compact, high transmission, velocity selector for thermal atom beams

3.1 Introduction

Since the discovery of the steering effect, the velocity of incoming particles and the polar angle of incidence are interesting parameters in a deposition experiment. Fundamental growth experiments are usually conducted with so-called thermal atom evaporators, such as Knudsen cells that emit atoms with a broad velocity spectrum. In these evaporators, a material is heated close to or even above the melting temperature, to provide a sufficiently high vapor pressure. This vapor can condense on a substrate resulting in the growth of a (thin) film on this substrate. An aperture-set in front of the evaporator usually limits the angular distribution of the sublimated atoms. The energy of these atoms is typically a few tenths of an eV, i.e. small compared to the condensation energy. The velocity distribution of N particles in the gas phase atoms is described by the Maxwell-Boltzmann distribution [25]:

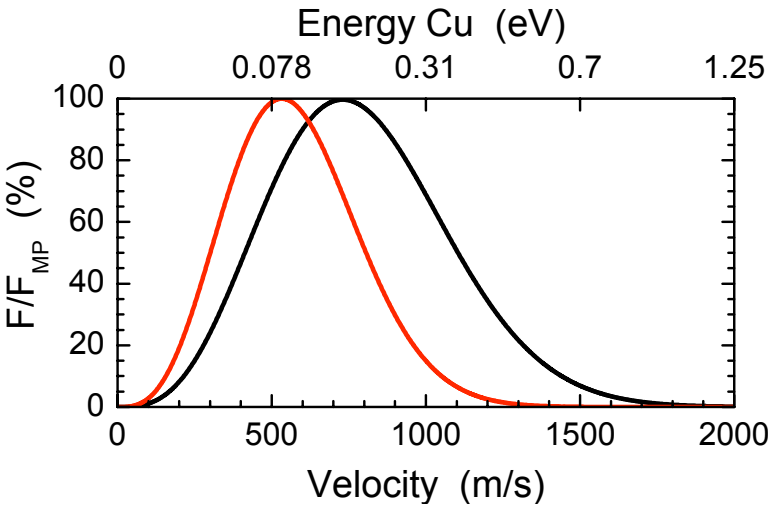

Figure 3.1: Normalized Maxwell-Boltzmann distribution of the velocity distribution F for Cu (black) and Ag (red) at their melting temperatures. Note that the top energy scale applies for Cu. Particles with velocities between $\frac{1}{2}v_{mp}$ and $2v_{mp}$ are highly abundant in the beam, with v_{mp} being the most probable speed.

$$N(v) = A_{MB} \exp^{-B_{MB}v^2} 4\pi v^2 \tag{3.1a}$$

$$A_{MB} = \left(\frac{m}{2\pi kT}\right)^{3/2} \tag{3.1b}$$

$$B_{MB} = \left(\frac{m}{2kT}\right) \tag{3.1c}$$

in this m is the mass of the particles and T their temperature, i.e. the temperature of the thermal atom source. The velocity distribution of the flux $F(v)$ on a substrate of this gas is given by [25]:

$$F(v) = A_{MB} \exp^{-B_{MB}v^2} 4\pi v^3 \tag{3.2}$$

Micro reversibility dictates that the velocity distribution of the flux is equivalent for impingement on a substrate, desorption from a substrate or flow through an aperture. Figure 3.1 depicts the velocity distribution of the flux for copper and silver. For Cu, Ag and Mo the melting temperatures T_m and the vapor pressures P_v at this temperature are listed in table 3.1, as well as the most probable velocity $v_{mp} = \sqrt{3kT/m}$ and the kinetic energy E_k of the particle at this velocity.

Symbol	T_m (K)	P_v (torr)	v_{mp} (m/s)	E_k (meV)
Ag	1235	10^{-3}	535	160
Cu	1358	10^{-4}	730	176
Mo	2896	10^{-2}	868	375

Table 3.1: Values of deposition parameters of Ag, Cu and Mo thermal atom sources. Provided are the melting temperature T_m and the vapor pressure P_v at this temperature. Also given are the most probable velocity v_{mp} and the associated kinetic energy E_k [26]

This chapter describes a velocity selector suitable for thermal atom beams, i.e. that is capable of velocity selecting neutral particles with a mean velocity of 500 - 1500 m/s. Velocity selection of neutral particle beams is routinely performed in scattering experiments employing neutral atoms and neutrons. In these cases a multi-disk configuration is employed. Such a set-up usually requires a quite long distance between source and sample resulting in a very substantial reduction of the deposition flux on the substrate. Before introducing the velocity selector concept used, the Fizeau type velocity selector will be discussed and the requirements are defined for the velocity selected evaporation source.

3.2 Requirements of the evaporator

The velocity selected atomic beam from an evaporation source must meet the following requirements.

1. The atomic beam should allow the study of the influence of the velocity of arriving atoms on the growth morphology. The desired monochromaticity of the beam is quite modestly and somewhat arbitrarily set at around 10%, predominantly determined by the need for sufficient flux.

2. The deposition rate should allow a growth rate of one monolayer in a period of typically a few tens of minutes at grazing incidence.

3. The deposition source must fit on the existing UHV system. This limits the available space.

4. The deposition source has to be UHV compatible so that the substrate experiences a pressure of $< 10^{-10}$ mbar.

5. The deposition source should have an experimental lifetime of at least 4 years, i.e this implies that expensive (time- and money consuming) parts should not have to be replaced within this period.

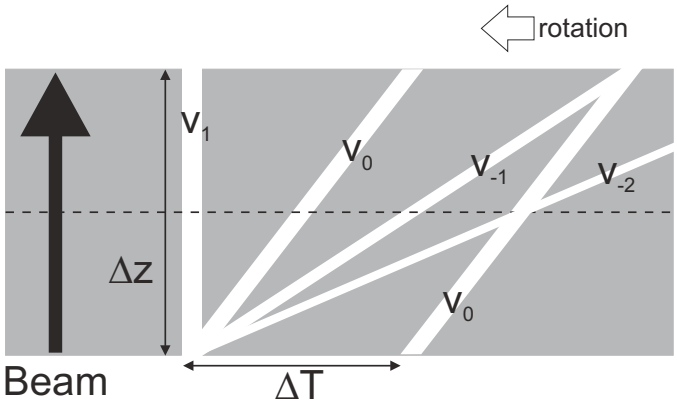

Figure 3.2: Particle paths through a double disk filter plotted in a z, t figure. The particles with the desired velocity v_0 pass the second disk at distance Δz in ΔT seconds. Also faster and slower pathways which lead to transmission are plotted: v_1 corresponds to $v = \infty$, v_{-1} and v_{-2} correspond to velocities of $v_0/2$ and $v_0/3$, respectively. Incorporating a third boundary (dashed line) blocks the pathways belonging to v_k with k=-1,1,3...

6. The total source has to comply with safety regulations.

3.3 A Fizeau type velocity filter

The simplest concept of a velocity filter is based on two synchronously rotating slotted disks. The individual chopper wheels are identical in shape, have one slit each, and open and close at the same time. The open and close times per cycle are, respectively, δt_o and δt_c. The delay time $\Delta T = \delta t_o + \delta t_c$ between the open-close cycle of the two choppers and their distance Δz determines the velocity of the particles that is passed without obstruction. The pathways for various velocities that are selected by such a set-up are shown in fig. 3.2.

The velocity selected, v_0 is given by

$$v_0(f) = \frac{\Delta z}{\Delta T} = f \cdot \Delta z \tag{3.3}$$

and can be changed with the rotation frequency f of the chopper. However, also faster and slower particles can pass this configuration, as depicted in fig. 3.2. The velocities v_k that can pass this two disks system are:

$$v_k(f) = f \cdot \frac{\Delta z}{(1-k)}, \text{with } k = -\infty..1 \tag{3.4}$$

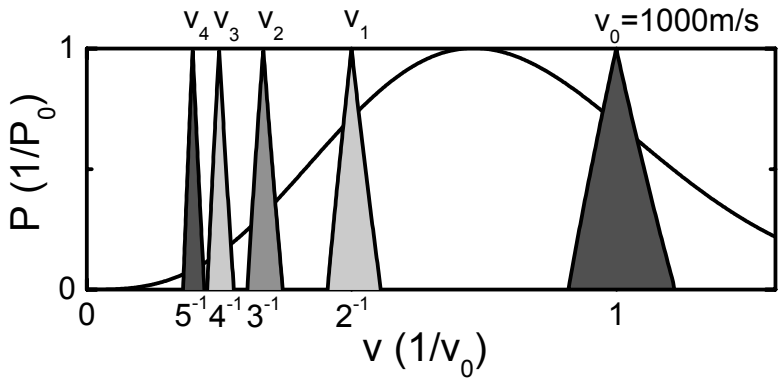

Figure 3.3: Transfer function of a two disks velocity selector of fig. 3.2. The desired velocity v_0 and four lower order side peaks (v_{-1}, v_{-2}, v_{-3}, v_{-4}) are shown. Insertion of a third disk at the half way position blocks the odd peaks (colored light gray). The v_{-2} peak (gray colored) can be blocked by inserting a fourth disk at one fourth position. The solid line reflects the Maxwell-Boltzmann distribution for Cu of fig. 3.1

The slower particles ($k = -1, -2, ...$) pose a problem (especially when selecting high velocities). The broad Maxwell-Boltzmann distribution, see fig. 3.3, gives a significant probability for these unintended velocities.

For an infinitely short open time ($\delta t_o \to 0$) faster particles ($k = 1$) have to travel at infinite speed to be able to pass. For a finite open time very fast particles with a velocity $v > \Delta z/\delta t_o$ can also pass. The presence of particles with such velocities is quite limited as long the open time is significant smaller than the delay time.

The slower velocities can be eliminated by systematically adding additional chopper disks. The addition of a third chopper halfway, indicated by the dashed line in fig. 3.2 will block the slower velocities with odd k index. A further elimination is achieved by adding choppers at 1/4, 1/8 etc. Do note that not only 1/8, but also 3/8, 5/8 and 7/8 are positions that eliminate v_{-4}, but one of these positions suffices to block these velocities. For particle beam velocity selectors, a quite large number of disks is usually used to eliminate the unwanted velocities with the Fizeau approach.

The performance of the velocity selector can be quantified by two numbers, the monochromaticity and the transmission. The monochromaticity A of this velocity filter is defined as:

$$A = \frac{\delta v}{v_0} = \frac{\delta t_o}{\Delta T} \tag{3.5}$$

The transfer function of a Fizeau type velocity selector with a monochromaticity

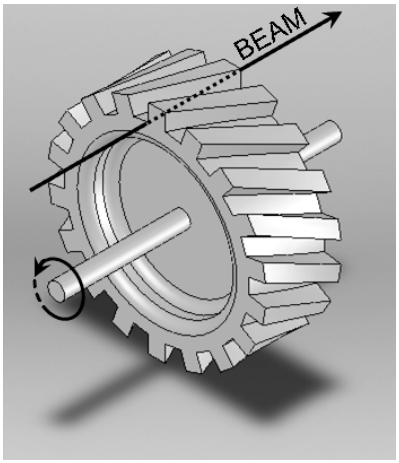

Figure 3.4: Sketch of a velocity selector with inclined channels.

of 10% is depicted in fig. 3.3 for a desired velocity of 1000 m/s.

The transmission ϵ of a velocity selector is defined as the effective open time of the selector:

$$\epsilon = \frac{\delta t_o}{\delta t_o + \delta t_c} = A \tag{3.6}$$

For the Fizeau velocity selector the transmission is equal to the monochromaticity. In growth experiments, a sufficient growth rate is required. With a Fizeau velocity selector, a 10% monochromaticity and thus a 10% transmission results in a reduction of the flux of the original evaporation source by at least two orders of magnitude. This hampers its application for the envisaged experiments.

3.4 Inclined channel velocity selector

The one-to-one relation between monochromaticity and transmission can be removed with an infinite number of Fizeau disks running at a locked phase. This infinite number of Fizeau disks results in inclined channels, see fig. 3.4 and only particles with the desired velocity will be able to pass through the channels. All particles outside the selected velocity window are caught by either the front or back side of the channel, see fig. 3.5. The transmission of such a device can be quite high as a large number of channels can be positioned next to each other. Note that this consideration only holds if particles hit and stick on the wall, like atoms from metal sources.

The delay time ΔT between the "entrance" and "exit" side of the selector, as a

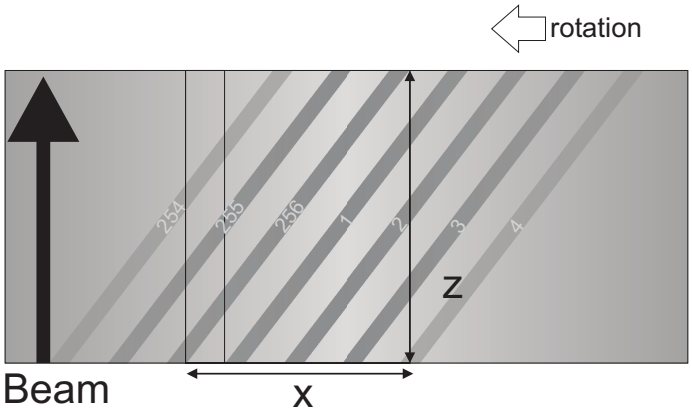

Figure 3.5: A number of inclined channels on a rotating cylinder. The 256 blades (only seven are shown) have a pitch of $\Delta x/\Delta z$.

function of rotation frequency f is now given by:

$$\Delta T(f) = \left(\frac{\Delta x}{2\pi R}\right)\frac{1}{f} \tag{3.7}$$

R is the outer radius of the cylinder and Δx is the displacement of the inclined channel measured along the circumference of the cylinder. The walls separating the inclined channels have a pitch $\gamma = \Delta x/\Delta z$ where Δz is the length of the cylinder. The selected velocity is:

$$v_0(f) = \frac{\Delta z}{\Delta T} = \Delta z\left(\frac{2\pi R}{\Delta x}\right) f = \left(\frac{2\pi R}{\gamma}\right) f \tag{3.8}$$

The monochromaticity A is determined by the ratio of the width of the inclined channel δx_o and the displacement Δx:

$$A = \frac{\delta x_o}{\Delta x} = \frac{\delta x_o}{\gamma \Delta z} \tag{3.9}$$

while the transmission is:

$$\epsilon = \frac{\delta x_o}{\delta x_o + \delta x_c} = \frac{1}{1 + \delta x_c/A\gamma\Delta z} \tag{3.10}$$

In this velocity filter, the monochromaticity and transmission are coupled by the pitch parameter γ, cylinder length Δz and the wall thickness δx_c which are design parameters. In principle a high monochromaticity and a high transmission are both

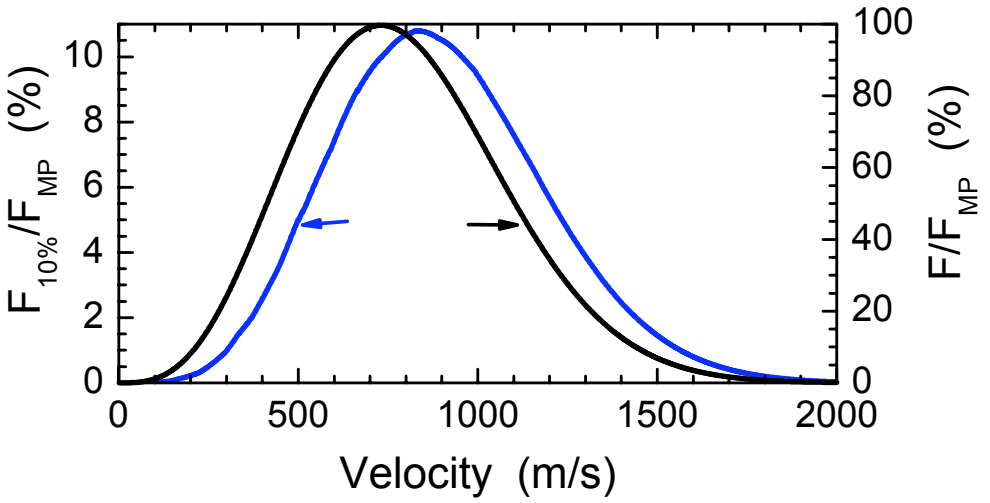

Figure 3.6: Flux of a Maxwell-Boltzmann Cu beam at the melting temperature as a function of velocity when applying a velocity selector with a monochromaticity of 10% (blue line). Also shown is the Maxwell-Boltzmann distribution of fig. 3.1 (black line).

possible with sufficient pitch and/or large enough thickness Δz.

3.5 Design of a velocity filter

3.5.1 Deposition Rate

The actual deposition rate on the substrate is governed by five parameters:

1. Monochromaticity A
2. Transmission ϵ
3. Distance source - substrate L
4. Deposition angle on substrate ϑ
5. The vapor pressure $p(T)$ in the sublimation/evaporation source with area A_S

The flux at the substrate $F_L(v_0, \vartheta)$ for a selected velocity and incidence angle is given by:

$$F_L(v_0, \vartheta) = f_A(v_0)\ \epsilon\ cos(\vartheta)\ \frac{p(T)\ A_S}{\pi\ L^2 \sqrt{2\pi\ m\ k_b\ T}} \tag{3.11}$$

In this $f_A(v_0)$ is the convolution of the transmission function and the Maxwell-Boltzmann distribution function of the metal source. This function is shown in fig. 3.6 for a monochromaticity of $A = 10\%$. This function now indicates the flux for a selected velocity. Note that the maximum of the flux has shifted towards higher velocity. A transmission of at least 50% is aimed at with the inclined channel velocity selector. A polar deposition angle of $\vartheta = 80°$ is typically used in grazing incidence deposition experiments. These 3 factors will reduce the flux at the substrate by a factor 100 compared to a deposition source without velocity selector at normal incidence and at the same distance. Our current sublimation sources ($A_S = 20$ mm^2) are capable of deposition rates of typically 1 ML/min at normal incidence at a distance of 200 mm, with a temperature close to the melting temperature. The desired deposition rate is about 0.067 ML/min, i.e. an additional factor 7 increase of the source has to be achieved by increasing the flux of the deposition source. This can be achieved by using a deposition source in which the temperature can be raised above the melting temperature. The numbers mentioned above illustrate and underline the importance of a high transmission velocity selector.

3.5.2 Motor

The maximum velocities of the particles are of the order of 1500 m/s. From eq. 3.8 the rotation frequency can be evaluated with some rough numbers for the disk size. A disk with a radius of $R = 100$ mm would still fit inside the space available, while a length $\Delta z = 50$ mm should not be exceeded to ensure a sufficiently small distance between source and substrate. A pitch of 1/5 requires a rotation frequency with a maximum of 500 Hz. Such rotation frequencies are typically realized in turbo molecular pumps (TMP). The rotor mass of a large TMP happens to be of the same order of magnitude as that of the velocity selector. The motor of a TMP can thus be used to rotate the velocity selector with the additional advantage of well established TMP-technology.

In standard pumps, especially the bearings of the motors show a large gas production at the fore-pump side. The outgassing of motors is in principle limited substantially for magnetically levitated pumps due to reduced friction and thus temperature. A recent development in these pumps is the MAG1300 by Leybold, with a maximum rotation frequency of 600 Hz. The rotor of this motor is stabilized with five independent degrees of freedom. This implies that a rotor balanced at relatively low frequencies can be used. Unbalance at operating frequencies can be actively compensated for by the five axis active magnetic levitation. The frequency of this motor can also be varied over a range between typically 200 and 600 Hz. A higher frequency would allow a smaller disk, but would also imply a strong increase in the stress in the

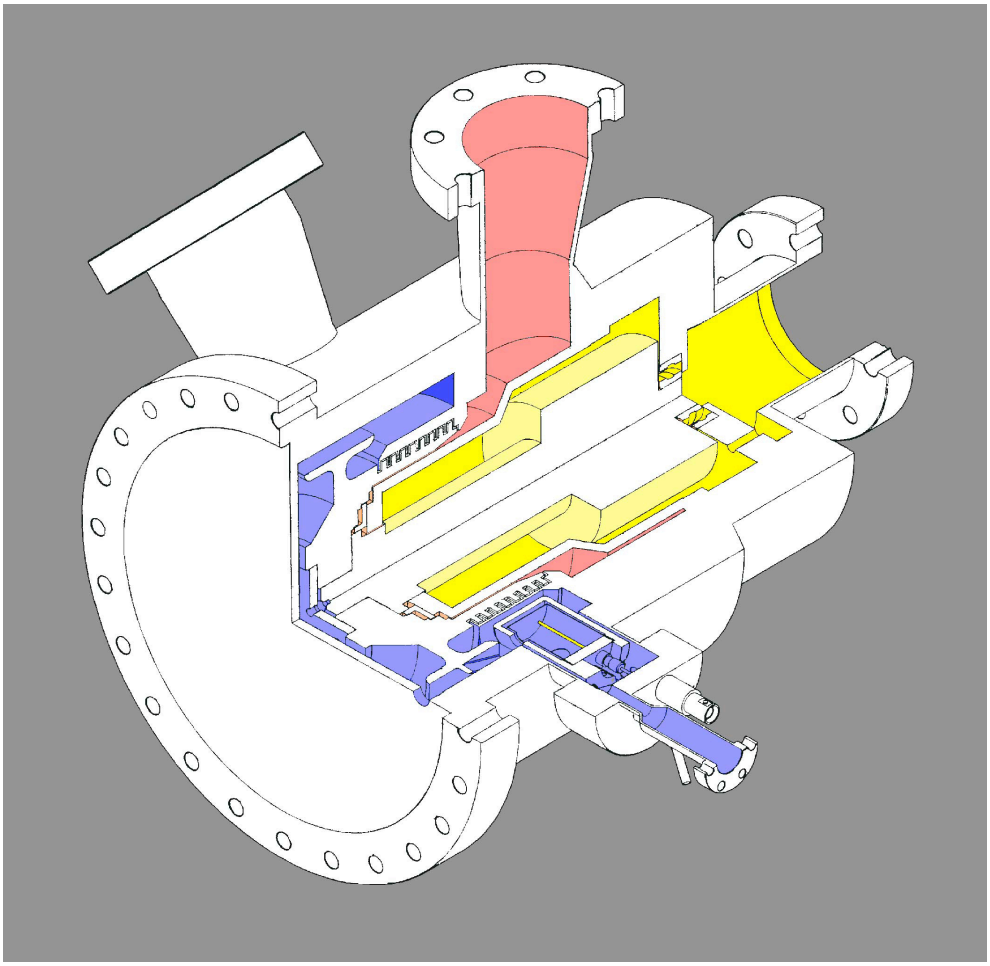

Figure 3.7: Differential pumping scheme of the velocity selector. Degassing of the coils (yellow region) results in a gas production that leaks to the other parts of the velocity selector. The main part of this gas production is evacuated by a turbo pump directly connected to the back side of the coils (also yellow region). A narrow fit of the velocity selecting wheel to the motor axis results in a high pump resistance to the differentially pumped chamber (pink). This chamber is separated from the source chamber (blue) by a labyrinth of which one part is not moving, while the counter labyrinth is on the rotating disk.

material due to the centrifugal forces. To use this motor, the dynamic properties like mass and inertia of the velocity selector should preferably be similar to the rotor used in this type of pump. The use of this motor also puts a constraint on the minimum radius of the selector, i.e. 80 mm $< R <$ 100 mm. The principle design with this motor is shown in fig. 3.7.

3.5.3 UHV compatibility

The magnetic levitation of the TMP limits strongly the outgassing of the low vacuum part of the pump compared to a standard TMP. However, by using the motor of the MAG1300 as such, places parts of the pump originally not intended for UHV use, in direct contact with the UHV surrounding of the substrate. The main gas production of this type of motor results from the degassing of the magnetic levitation coils in the *degassing coils chamber*. To establish the gas production, a TMP 50 l/s pump was mounted to the rough vacuum port of the TMP1300. A leak rate towards the *source chamber* containing the velocity selector and source of $Q = 1{\cdot}10^{-8}$ mbar·l/s was measured in this configuration.

The *source chamber* is pumped by a TMP with a pumping speed $S = 200$ l/s. To maintain a pressure p in the 10^{-11} mbar range, a maximum gas load of $Q = p \cdot S = 2 \cdot 10^{-9}$ mbar·l/s can be allowed. A differential pumping scheme is therefore introduced to maintain UHV conditions at the substrate. A considerable part of the gas production is removed with a 50 l/s TMP attached to the bottom of the MAG1300. Sufficiently large openings connect this bottom side to the *degassing coils chamber* and reduces the effectiveness required for the differential pumping at the *source chamber*. The differential pumping scheme is obtained by introducing two restrictions in conductance between the *degassing coils chamber* and the *source chamber*, see fig. 3.7. The first restriction limits the conductance between the *differentially pumped chamber* and the *degassing coils chamber*. It consists of a close fit of the velocity selector on the cartridge hood. A terrace structure in the hood and velocity selector effectively reduces the conductance. A second labyrinth forms a restriction between the *differentially pumped chamber* and the *source chamber* and is designed in such a way that its conductance is below 1 l/s. The *differentially pumped chamber* is pumped by a 50 l/s TMP and the ratio of the conductance through the labyrinth and this TMP, as well as by the introduction of the first labyrinth should ensure a gas leak of the motor towards the substrate well below 10^{-9} mbar·l/s.

The second labyrinth also has a positive effect on the rotor dynamics. The shape of the velocity selector is transformed from a disk like to a cylinder shape around the cartridge, see fig. 3.9. This latter shape and weight are rather close to the original rotor of the MAG1300 turbopump.

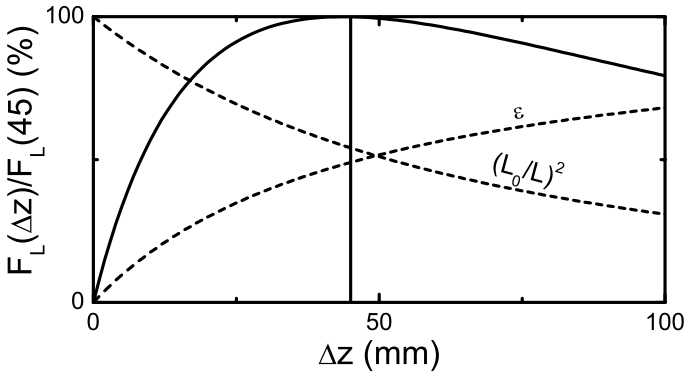

Figure 3.8: Flux as function of the thickness of the disk Δz (solid line). The flux depends linearly on the product $\epsilon \cdot \left(\frac{L_0}{L}\right)^2$, with ϵ the transmission, L_0 the distance required to fit the substrate holder and non rotating parts and L the source sample distance ($L = L_0 + \Delta z$). At Δz = 45 mm the product is maximal. (Evaluated for a velocity selector with properties: R = 85 mm, f_{max} = 600 Hz, L_0 = 125 mm, δx_c = 1 mm and A = 10%.)

3.5.4 Disk design

The weight of the aluminum rotor in the MAG1300 is about 3 kg. The approximate dimensions of the velocity selector, i.e $R = 100$ mm and $\Delta z = 50$ mm result in a total volume with a weight much lower than the original rotor if made from aluminum. The small volume allows the possibility to use a titanium alloy, a light weight material that possesses high strength. The alloy of choice is LT31, commonly used in surgery and space, because of its good wear and strength properties. Table 3.2 displays the relevant properties of LT31. Titanium has also the advantage over aluminum that it can be chemically cleaned from copper (or silver) used in the deposition experiments, so that the life time of a disk is increased. This titanium alloy also suffers less from low fatigue due to many operation cycles and baking cycles. Repeated change in frequency and operation at elevated temperatures is known to limit the operation lifetime of turbopumps. Such material wear is expressed in so-called Wöhler diagrams [27]. As the velocity selector is operated at room temperature and the number of operating cycles is expected in the range of 1000, this material wear is not an issue.

The velocity disk was made by spark erosion, which allows the creation of details as small as 0.1 mm. This size gives the lower limit of the channel width. However to ensure enough strength of the channel walls, the thickness of these walls is set at

Property	Value
Material description	TiAl6V4
Density	4430 kg/m^3
Elastic modulus	110 GPa
Proof stress ($R_{p0.2}$)	> 830 MPa
Tensile stress	> 900 MPa

Table 3.2: Properties of titanium alloy "LT31" used for the disk in the velocity selector.

$\delta x_c = 1$ mm. The maximum frequency and radius are $f = 600$ Hz and $R = 100$ mm respectively, and according to eq. 3.8 the pitch is the quantity that determines the maximum velocity for which the selector can be used. With a maximum particle velocity of 1500 m/s, the pitch is 1/4.

The thickness of the disk Δz is chosen to optimize the flux on the substrate. An increase results in enhanced transmission, see eq. 3.10. However, an increase in source - substrate distance L also decreases the deposition rate, see eq. 3.11. Without velocity selector, a distance $L_0 = 125$ mm is required to fit the substrate holder and non rotating parts of the velocity selector. Figure 3.8 shows the normalized deposition rate as a function of the thickness of the disk. Also shown are the influence on transmission and distance separately. An optimal length Δz = 45 mm is found. Note that the broad optimum leaves space to vary the path length. Setting the monochromaticity to 10% gives a transmission of $\epsilon = 49\%$.

These values are the starting values for a stress optimization calculation of the disk. This stress optimization has been performed with a finite element method by the Bunova company. The amount of stress is evaluated as the von Mises stress [27]. The optimization resulted in the von Mises stress for the design shown in fig. 3.9. Especially the stress in the center of the disk determined the design boundaries. The maximum stress was reduced by decreasing the radius to 85 mm. The maximum stress was finally lower than half the tensile stress, used as the standard low risk safety factor. The final design parameters are listed in table 3.3, as well as the mass and inertia of this design.

3.5.5 Safety and Lifetime

The kinetic energy stored in the velocity selector at full speed is in the range of 70 kJ. This implies that safety measures have to be taken in order to release this energy along a rather safe path in case of emergency. In a crash situation, the channel structure will touch the wall. Their relative brittleness helps to release some of the

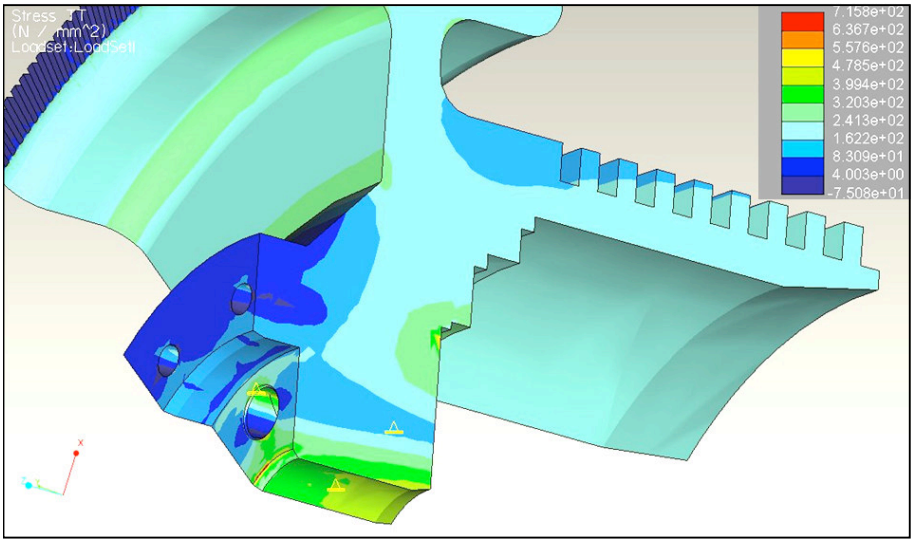

Figure 3.9: Von Mises stress calculated with a finite element method by Bunova for the velocity disk at a rotation frequency of 600 Hz. High stress areas are located in the bolt holes. Plastic deformation is expected to decrease the actual stress in these areas.

energy. Further safety is obtained by a three centimeters thick steel housing around the velocity selector.

The effect of the lifetime is simulated by a hit and stick deposition of atoms with the "wrong" velocity on the blades. Not only the channels become smaller as a result of this deposition, but also the weight of the rotor and its inertia changes, causing an unbalance of the dynamical bearing system. Even after 10.000 hours of operation, no substantial effect is expected from the simulation, providing ample research time. A shutter located between the source and the rotating disk enable to avoid deposition on the rotorblades when no growth is taking place.

3.5.6 Realisation of the velocity selector

The disk for the velocity selector and the housing were manufactured by VacuTech. All parts were assembled in house and shipped to Leybold, Cologne, for balancing the disk and a first test of the dynamical behaviour of the velocity selector in a safe environment. Figure 3.11 shows the properties before balancing. The results show that balancing is not necessary, e.g. the disk is sufficiently symmetric. Only a minimal current of 0.3 - 0.4 A is needed during operation at constant speed.

The velocity selector is mounted beneath the existing UHV setup as outlined

Parameter	Symbol	Value	Unit
Particle speed	v_0	[500-1500]	m/s
Frequency	f	[200-600]	Hz
Selectivity	A	10	%
Wall thickness	δ_c	1.00	mm
Channel width	δ_o	0.96	mm
Radius	R	85	mm
Displacement channel	Δx	9.6	mm
Thickness disk	Δz	45	mm
Transmission	ϵ	49	%
Number of blades	N	272	blades
Mass	m	3.02	kg
Inertia	$I_{x,y}$	$6.9{\cdot}10^{-3}$	kg·m^2
	I_z	$1.1{\cdot}10^{-2}$	kg·m^2

Table 3.3: Design parameters of velocity selector. The z axis coincides with the rotation axis. x, y axis are perpendicular to the z axis.

in fig. 3.10. Sample preparation and the analysis of the surface morphology with High Resolution Low Energy Electron Diffraction (HR-LEED) is done in the main part of the UHV system located above the velocity selector. At the level of the velocity selector, two UHV flanges (P) at near normal view during grazing incidence deposition are located that allow the mounting of an electron gun and a fluorescent screen. Together they allow the monitoring of the deposition process. A quartz crystal micro balance can be inserted at the place of the substrate to monitor the flux of the source.

Baking is a standard procedure to obtain a UHV environment. The maximum allowed temperatures of the magnetic bearings and motor (100 and 140 °C, respectively) and the limited pumping speed due to the incorporated labyrinths require special attention during the baking process. While the rest of the system is already baked, the cooling circuit of the magnetic bearings (coils etc.) of the velocity selector remains switched on. After typically 10 hours both the cooling circuit and the heating of the velocity selector is switched off. The temperatures at the center of the velocity selector where the motor and bearing magnets are located, increases. When the temperature as monitored by the motors temperature reading reaches 85 °C, both cooling circuit and heating are switched on again. The cooling of the motor is much more efficient and a steep decrease in motor and bearing temperature results. After a few minutes both are switched off again. This cycle is repeated three times. The fourth cycle is different. Instead of switching on both heating and cooling, only all heaters (of the velocity selector and UHV system) are switched off. These cycles are

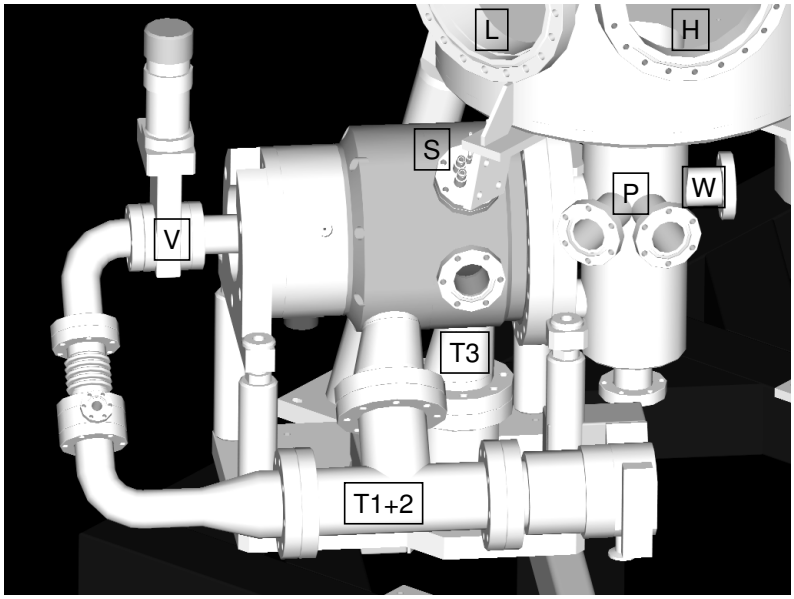

Figure 3.10: Velocity selector mounted beneath the UHV system. The source (S) deposits towards the window (W). With a combined LEED gun and phosphor screen (P) growth at the sample can be monitored during growth. After growth, the substrate is raised in order to enable the study of the surface morphology with HR-LEED (L). The different chambers of the velocity selector are pumped with TMP's: (T3) 200 l/s connected to source chamber, (T1+2) connected to cartridge and in between chamber chamber. Initially a valve (V) is used to control the pumping speed ratio between these chambers. To obtain better vacuum conditions, both T1 and T2 are pumped by a 50 l/s TMP each. The pressure in front of each TMP is measured separately.

repeated for about 8 hours. The next day (16 hours later) the temperature has stabilized around 45 °C. Cooling is switched on resulting in an operating temperature, with the disk rotating, of 35 °C.

After preparation of the velocity selector, the source can be calibrated with a quartz crystal is mounted in front of the velocity selector. The first test runs resulted in depositing a few monolayers with a rate of 0.1 ML/min. Experimental time is, however, still limited due to rapid heating of the source environment.

3.5.7 Deposition source

A high rate deposition source as shown in fig. 3.12 was designed and home-built. The Knudsen cell made of molybdenum and surrounded by filaments as shown in fig. 3.12 b) and d). A combination of radiative heating and electron bombardment

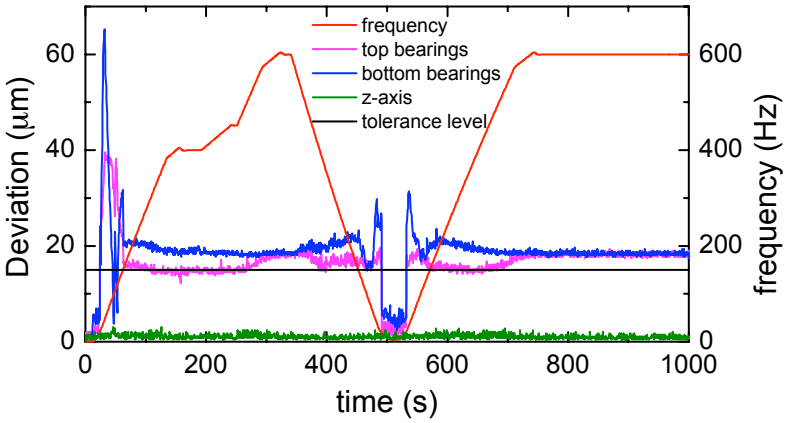

Figure 3.11: Results of the balance test of the selector mounted on the MAG1300 cartridge. Below the lower working limit of 200 Hz increased instabilities are visible due to eigen-frequencies of the velocity selector. The lateral position of the axis near the top and bottom bearings show a small surplus of deviation in the working range (200 - 600 Hz), which provides no danger at all. The tolerance level is within the high security standard for MAG1300 TMP's dealing with continuous operation and high temperature cycles. The test has been performed within a safety box at Leybold Test Facility in Cologne.

is used to achieve a temperature of the Knudsen cell above the melting temperature of copper. A sapphire tube is inserted through all three heat shields and fits around the opening of the molybdenum cell. This prevents evaporation on the heat shields surrounding the source. The inner shield is electrically isolated and works as a Wehnelt cylinder. The outer shield has a direct conductive contact with the base of the source, which is water cooled. After assembly, the source was first cleaned and tested in a separate system. A quartz crystal to monitor the rate is placed 16 cm from the source, i.e., at the same distance to the substrate as in the actual velocity selector. The filaments are operated at a current of 3.25 A and a high voltage of up to 1 kV can be supplied for electron bombardment heating. The maximum power for heating the Knudsen cell is limited by the cooling efficiency. The source can currently be operated at its maximum heating power for a few minutes.

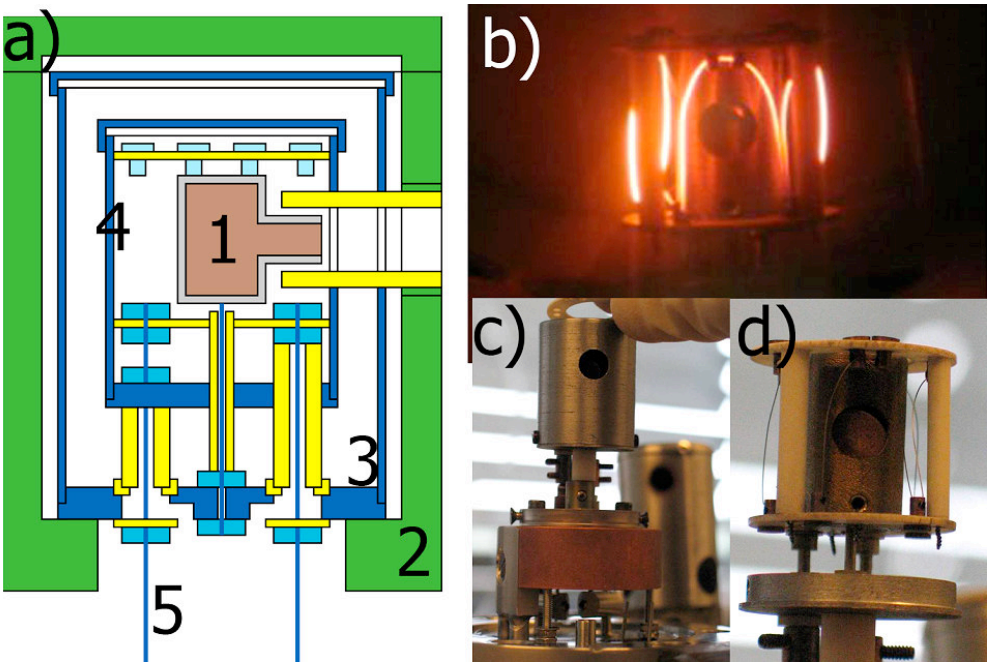

Figure 3.12: The Knudsen cell used for deposition. a) Schematic drawing with indicated (1) the Knudsen cell, (2) the outer heat shield, (3) the second heat shield, (4) the inner heat shield and (5) the contact electrodes. The yellow parts are insulating and made from sapphire. b) Image of the radiating filament showing the lay out of the filaments, c) The source mounted with the inner shield in place on the Cu water cooled base. The second shield is situated in the background. d) Image of the interior of the Knudsen cell with the filaments mounted.

CHAPTER 4

Simulation Methods

4.1 Introduction

To investigate quantitatively the steering effect, experimental results are compared to simulations based on elementary diffusion and deposition processes in copper growth. This chapter describes the simulation software developed for this task. It consists of two very different components: the diffusion processes on the surface, and the trajectory evaluation of atoms deposited. Another important aspect is the implementation of the corresponding algorithms resulting in an efficient simulation software that can be run with a server based system on an arbitrary number of PC's.

4.2 kMC approach to simulate diffusion processes

The atoms that form the surface of a crystalline material spend most of their time in a relatively low potential energy position. In these low energy positions their motion is limited to a small excursion around their lowest energy point at a finite temperature. Only occasionally a diffusion process occurs as a transition of an atom from one low energy position to a nearby low energy position. The initial and final energy of these positions do not have to be equal. The likelihood of such an event is usually described by the activation energy, i.e. the difference between the initial energy and the highest energy on the pathway between the initial and final state. The rate of this process is given by Boltzmann statistics:

$$f_{diffusion} = f_{attempt} \cdot exp\left[-E_{activation}/\left(k_B \cdot T\right)\right] \tag{4.1}$$

where $f_{diffusion}$ is the diffusion frequency of an atom in a certain direction, $f_{attempt}$ is the oscillation or attempt frequency of an atom inside the well (10^{13} s^{-1}), k_B is the Boltzmann constant, and $E_{activation}$ is the activation energy for a hop.

For a crystalline surface, the low energy positions are found on a grid given by the crystal mesh. This implies that relaxation effects are neglected. The diffusion on a crystalline surface can thus be viewed as stochastic processes on a fixed grid. The diffusion processes are implemented through knowledge of the elementary diffusion processes that can occur through the value of the activation energies for these processes. The mapping of stochastic processes on a lattice allows the use of the kinetic Monte Carlo (kMC) method for the evaluation of diffusion on a surface. The basic ingredient is the compilation of a list of all diffusion events that must be taken into account.

Several approaches have been used for kMC simulations. A program cycle in which first an atom on the surface is randomly selected is often used. For this atom it is evaluated whether or not it will diffuse. This works very well if the diffusion processes taken into account are rather similar in rate. However, various diffusion rates on a Cu(001) surface can differ by more than 11 orders of magnitude. Almost all atoms selected will remain at their position and most of the time is spent on waiting until the few atoms that are likely to move are indeed selected. This makes this method highly ineffective. The approach used in this work is to perform a diffusion move in every cycle. This is done by adding the rates of all possible diffusion processes of all the atoms on the surface. The deposition rate is also added to this total diffusion rate. A random number is drawn and this selects the actual diffusion process. Processes with high rates are more likely to be selected, but also processes with a low rate can be drawn in a cycle. The selected move is performed and the new total diffusion rate of the surface can be evaluated for the next cycle. A quick search of the process selected by the random number is essential to keep the CPU time of each cycle within acceptable range. A tree data structure is implemented dividing the surface in regions, sub regions, sub sub regions etc. The deposition flux has a constant rate and serves as the time base for the simulation.

4.2.1 Diffusion processes

The lattice approximation assigns to all atoms a fixed position on a fcc(001) lattice. Their transition to another position is restricted to a nearest neighbour position, i.e. to a single hop. This limits the direction of movement to the four equivalent

$\langle 110 \rangle$ directions. In the approximation used, the activation energy ($E_{activation}$) to each of these positions depends on the occupation of the nearest and next nearest neighbouring sites. Figure 4.1 shows two Cu(001) layers with three adatoms on top. Atom *2* can move in all four directions ($[\bar{1}10]$, $[1\bar{1}0]$, $[\bar{1}\bar{1}0]$ and $[110]$) to positions *a*, *b*, *c* and *e*, respectively. The electronic interaction of atom *2* with atoms *1* and *3* lowers the barrier for diffusion to position *e* compared to a diffusion step to position *a*. The movements of atom *2* are all within the same terrace and are thus called intralayer diffusion processes. Atom *1* can also diffuse to the equivalent positions *g* or *h* at the lower terrace. These diffusion paths give rise to interlayer diffusion.

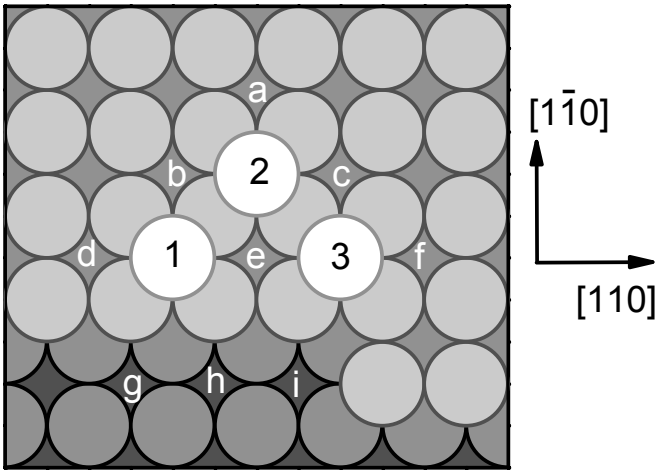

Figure 4.1: Overview of positions (a - i) to which atoms 1-3 can diffuse.

The activation energy of intralayer diffusion processes depends mainly on the occupation of nearest neighbour and next nearest neighbour sites, see Figure 4.2. For transport in the layer in the direction of the arrow, a maximum of 7 of these neighbour positions can be occupied providing 128 possible configurations. Due to symmetry, 72 unique configurations of neighbouring atoms remain that can be assigned a particular activation barrier. Biham and coworkers [28] generated a table of activation barriers of these 72 configurations for Cu(001), see table 4.1. Full dynamic simulations using an Embedded Atom Method (EAM) potential were used to generate this set. The quality of the set was verified by constructing several models with two till four parameters that are accessible to experiment. The models accurately describe the complete set. The reliability of the set was tested further by comparing sub-monolayer growth calculations as a function of both temperature and deposition flux with experiments. An accurate comparison was found over a temperature range of 200 to 500 K [28].

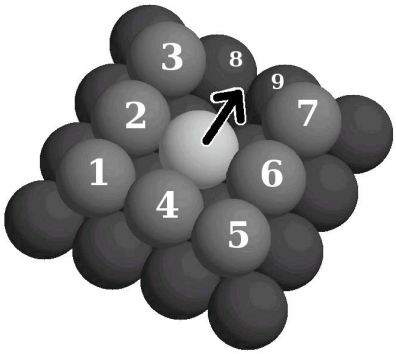

Figure 4.2: The activation energy for diffusion of the atom in the middle in the direction of the arrow depends on the individual presence of the 7 numbered atoms and the absence of atoms 8 and/or 9.

Two possible paths for interlayer diffusion have been implemented, diffusion over the thermodynamically favoured ⟨110⟩ step edge and over a ⟨100⟩ step edge. A kink site in a ⟨110⟩ step edge is treated as the smallest possible ⟨100⟩ step edge. Atom *1* in fig. 4.1 can diffuse to the lower terrace over a ⟨110⟩ step edge and will end up in either position *g* or position *h*. A move of atom *3* in the $[\bar{1}10]$ direction results in occupying position *i*. The local configuration of the stepedge for this transport is a kink position in the ⟨110⟩ step edge, identified as a ⟨100⟩ step edge. These situations are implemented in the simulation routine by not only looking at the nearest - next nearest neighbours as labeled in fig. 4.2 but also by considering the occupation of positions *8* and *9*. If positions 8 and 9 are unoccupied (and consequently positions *3* and *7* as overhangs are not allowed) a ⟨110⟩ step edge is determined in the simulation. If either *8* or *9* is occupied, a ⟨100⟩ step edge is identified. The barriers for these interlayer diffusion paths differ from the intralayer paths. An extra barrier, called the Ehrlich-Schwoebel (ES) barrier [29, 30] is added for these paths. At first glance, this approach neglects pathways involving exchange processes. However, the simulation only observes the initial and final configuration of a diffusion move. Exchange moves provide the same initial and final state configurations, only with other, in homoepitaxy indistinguishable atoms. The actual ES barrier defined in this calculation can therefore well be an effective barrier representing more than one diffusion process that all result in an indistinguishable transition from identical initial to final configurations.

n_1 ↓ / n_2 →		68	76	4	12	0	8
0		0.010	0.340	0.312	0.480	0.480	0.810
1		0.020	0.352	0.340	0.530	0.560	0.850
2		0.020	0.324	0.312	0.440	0.460	0.740
3		0.050	0.340	0.336	0.480	0.540	0.780
16		*(1,68)*	*(1,76)*	0.324	0.500	*(1,0)*	*(1,8)*
17		0.040	0.360	0.352	0.540	0.660	0.890
18		0.050	0.348	0.332	0.490	0.520	0.800
19		0.080	0.356	0.356	0.520	0.610	0.830
32		*(2,68)*	*(2,76)*	0.312	0.480	*(2,0)*	*(2,8)*
33		*(18,68)*	*(18,76)*	0.352	0.540	*(18,0)*	*(18,8)*
34		0.260	0.336	0.352	0.500	0.550	0.780
35		0.272	0.344	0.372	0.490	0.620	0.810
48		*(3,68)*	*(3,76)*	0.352	0.510	*(3,0)*	*(3,8)*
49		*(19,68)*	*(19,76)*	0.372	0.560	*(19,0)*	*(19,8)*
50		*(35,68)*	*(35,76)*	0.376	0.510	*(35,0)*	*(35,8)*
51		0.292	0.352	0.400	0.530	0.700	0.690

Table 4.1: Set of activation barriers (in eV) for all 128 possible configurations involving nearest and next nearest neighbours. The set is taken from Biham et al. [28]. The barriers in the marked region have been artificially increased, see text. Each value in the table belongs to a configuration (n=n_1+n_2) which is a union of two configurations: one at the top row (n_1), and one in the left hand column (n_2). Configurations which are mirror symmetric to another configuration have a reference to it. The extra small increase in the activation barrier of vacancy diffusion (E_{127}) is not added to the value in this table.

4.2.2 Deposition

Deposition events are very rare compared to diffusion events. Deposition events are regarded to take place instantaneously. This is motivated by the fact that a Cu atom evaporated from a Knudsen cell has a most probable velocity of 770 m/s. Relevant interaction between this atom and the substrate takes place over a distance of at most 1 nm. This gives a deposition time of 1.4 ps. At 250 K, such fast processes are associated with a barrier of only 57 meV. All diffusive moves with such low energies are already considered to be instantaneously and as a consequence also the deposition process occurs instantaneously.

Random number generator

A (pseudo) random number generator is at the core for the implementation of a Monte Carlo simulation. Every program cycle that determines a diffusion move or deposition event requires the generation of a random number. The quality of this generator sets the validity of the simulations. Already small regularities in the generator can lead to erroneous results, like for instance a larger deposition at one part of the grid or the preference for one in a set of equivalent directions for diffusion. The random number generator has to meet two constraints to avoid this. First the generation of a large random number, called the width, so that it spans the large variety in different diffusion rates on the surface. This assures that all possible events considered, how unlikely they might be, are included in the determination of the diffusion pathway to be executed. The second requirement deals with the pseudo randomness of the random number generator. This implies that there is always a period after which the same list of numbers is generated again. This period has to be sufficiently long. The default random number generators in operating system libraries are in both respects usually insufficient for scientific purposes.

In this simulation software a modified version of the *ran2* algorithm from Numerical Recipes[31] is used. Each random number is generated from two sequential "calls" to *ran2* and the result combined in a 64 bit integer giving almost $2 \cdot 10^{19}$ different levels. The width of this random number is sufficient. For example, a demanding situation is the occurrence of a thousand trimers at a temperature of 270 K. For a deposition rate of 1 ML/min this results in $2{\cdot}10^{12}$ lots. The span of the random number generator is therefore sufficient. The period of this generator was found to be larger than 10^{18}, more than sufficient for the number of calls in the program (for example, 10^{12} diffusions occur when depositing 40 ML at a temperature of 270 K at a deposition rate of 1 ML/min at a grazing incidence angle of 80^o).

The random number generator is initialised with a seed to assure different start values. This seed is derived from the computers clock and is as such different for each simulation.

4.2.3 Acceleration of the simulation

The activation barriers for some of the diffusion pathways for a Cu(001) surface given in table 4.1 are very different from those listed by Biham et al. [28]. The changed barriers are all of the low barrier processes. The presence of these processes results in a computation time that is not practical for the simulations envisaged. Many of the very fast processes, like stepedge diffusion, can be regarded as a long series of attempts to end up finally in a very limited number of occupation sites.

The important mechanism in the simulation is that this final site is actually selected. To accelerate this process, two different approaches are feasible: All possible sites are determined with their change as a final position. The final position is then determined in one step. Although this is a very fast method, it requires detailed programming of specific situations. A different approach is therefore taken. The fast process is slowed down. The visitation of the limited number of all possible sites still occurs, but at a lower rate. This is achieved by increasing the diffusion energy of fast processes (below 400 meV) in order to slow down these moves:

$$\begin{aligned} E' &= E + \alpha\,(400 - E), && \text{if E} < 400\,\text{meV} \\ &= E, && \text{otherwise} \end{aligned} \tag{4.2}$$

In this E is the original activation energy and E' is the scaled energy barrier as a result of the scaling parameter α.

All processes with barriers below 400 meV were studied separately to study the feasibility for suppressing the rate of the process. The marked barriers are below 400 meV and are suppressed by the above equation. Not all original activation energies below 400 meV are scaled. The ones that have no effect on the total computation time and do not affect the outcome of the morphology, are not modified. These describe configurations that are both statistically rare during growth and have such a low barrier that when they occur, they happen instantaneously. If these barriers would be nonetheless suppressed, physically unreal situations can occur. Even then the changes of an effect on the end result of a growth simulation would be negligible.

There is one special barrier which requires extra attention. After a careful evaluation, a different suppression was found to be needed for the vacancy diffusion barrier E_{127}. The standard change would result in additional creation of vacancies in adatom islands. These additional vacancies change the shape of these islands indicating that vacancy diffusion plays an important role in growth. A careful increase of this barrier is therefore done. The details are described in chapter 5.

The computation time strongly depends on the parameter α and this is illustrated in fig. 4.3. The cumulative number of diffusion steps as a function of the coverage for several values of α are shown. At the right side of the figure, an estimation of the simulation time is given for a personal computer with a pentium 4 3GHz processor. The performance is measured with the LINPACK benchmark. The performance for the above computer is around 700 Mflops. (At least 5000 are currently needed to get a notation on the top 500 supercomputers ranking).

This scaling of the activation energy was proposed by Biham et al, who concluded that the island separation in the submonolayer regime does not depend on α for values below 0.8. Higher coverages are simulated in this work and the limit of α was

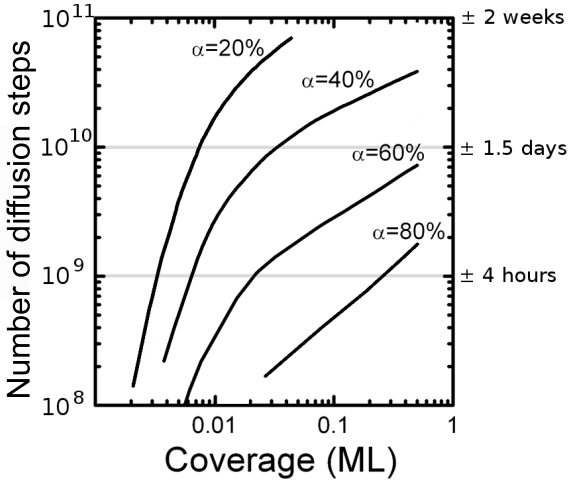

Figure 4.3: Cumulative number of diffusion steps as a function of the coverage for several values of α. The estimated duration of a number of diffusion steps counts for a pentium 4 3GHz computer.

investigated. The criterium for a limit on α is that it should not alter the actual morphology of the surface in a growth simulation. Figure 4.4 shows a snapshot of simulated morphologies for several values of α. The island separation is similar, but for higher values of α more $\langle 110 \rangle$ step edges are observed. As the relative presence of the $\langle 110 \rangle$ and $\langle 100 \rangle$ step edges determines the interlayer mass transport, this limits the value of α to 60%. This is described in more detail in chapter 5

4.2.4 Programming and server based distributed execution

Simulations should not only be correct, but should also be possible to be executed in a reasonable time frame. The different algorithms in the simulation package (diffusion and deposition) were optimized in performance, taken into consideration their relative contribution to the total CPU time. The implementation in the C programming language has given the necessary flexibility for optimizing the code. This language also results in a relatively fast machine language and it is available for virtually any existing operating system. Great effort was spent to structure the program into logical building blocks that allow substitution. For instance the deposition process can be easily exchanged for a sputter block for erosion simulations.

The results of the simulated morphologies are compared to experimental measurements through the extraction of statistical parameters, like island separation distance, island shape, roughness and facets. Sufficient statistics is very often only achieved by

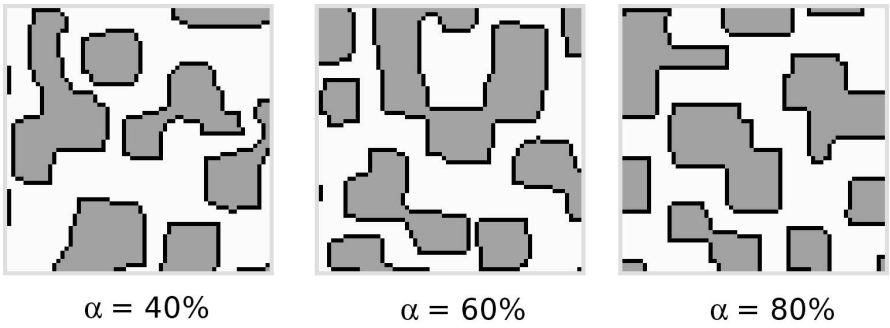

Figure 4.4: Morphology after 50 %ML growth for several values of α.

considering large surfaces consisting of several millions of atoms. To keep substrate sizes within reasonable bounds a maximum grid of 512×512 atoms is used. Larger surfaces are simulated by averaging over a number of simulations. This also allows to distribute the simulation task over different computers. A schematic overview of the server based system is given in fig. 4.5.

The workstations (clients) run a small program that connects to a server. The server sends a specific task to the client, consisting of the simulations executable code, the current state of the task and the settings to be used. While running a task, the client keeps connected with the server. About every five minutes, the output of the task and the new system state is sent back to the server. When a client disconnects, the server will give the last saved state of the task to another client. The time scale of five minutes is a compromise between the lost amount of work and a minimization of information exchange. With this method clients can comprise a wide variety of computers whose idle time is used with the lowest priority to perform a simulation request.

All tasks in the server system are ordered by their specific priority. The user controls in this way the priority of the simulation tasks. This enables the use of clients with very different CPU speeds. Tasks with high priority are given to the fastest machines and a regular redistribution of tasks assures an optimized execution of priority simulations. The server program has been written in the Python programming language. Python is a highly structured language very suited for administration tasks. All administration issues and clients that performed specific simulation tasks are saved in a PostgreSQL relational database. The database is also used for interlocking tasks between clients. The server can be controlled by a PHP web-interface which interacts with the database.

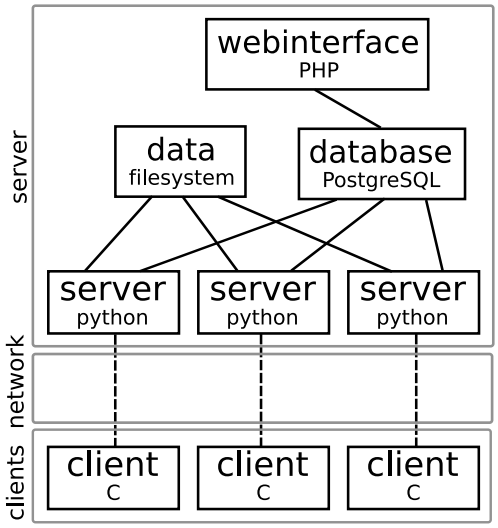

Figure 4.5: Schematic overview of distributed system.

4.3 Steering and heterogeneous flux distribution

4.3.1 Trajectory of an incoming atom

The trajectories of incoming atoms are changed as a result of an attractive force between an incoming particle and the substrate, leading to the steering effect [7, 8]. The condensation energy of atoms on a surface already provides a force that accelerates incoming atoms. Only at normal incidence and for a completely flat surface, the trajectory does not change. Also particles with an energy much larger than the condensation energy do not experience an appreciable change of their trajectory. However, such particles will usually create a sputter event. In any realistic deposition situation a trajectory change always occurs. The change of the trajectory depends on the local morphology and which thus gives rise to a heterogeneous flux on the surface. The change of the trajectory depends on the specific interaction between the incoming particle and the substrate. It can be described by a potential energy landscape which the incoming atom traverses.

4.3.2 Attractive potentials

The incoming atom has neutral charge and at large distance the temporal dipole-dipole or dispersive interaction will be dominant. Very close to the surface the electron overlap will lead to a very strong but short range interaction. The latter is the

predominant contribution to the condensation energy of an incoming atom [11, 32].

The Lennard-Jones (12,6) potential

In the qualitative evaluation of the steering effect [7, 8, 33, 34] a Lennard-Jones (12,6) pair pair potential was used. The parameters of this potential were taken from the work of Sanders and DePristo[9].

$$\phi_{SDP}(r) = \frac{c_{L12}}{(r/\xi)^{12}} - \frac{c_{L6}}{(r/\xi)^6} \tag{4.3}$$

They fitted the value of the parameters c_{L12} and c_{L6} from the cohesive energy of fcc copper and ξ from the nearest neighbour distance between atoms. This gives $c_{L12} = 0.4849$ eV, $c_{L6} = 0.8806$ eV and $\xi = 2.55$ Å and the resulting potential is depicted in fig. 4.6. The attractive part of this potential results from the power 6^{th} term that describes the distance dependence of dipolar interaction. The 12^{th} order term is repulsive. The cohesive energy is given by the binding energy in a kink position on the Cu(001) surface as displayed in fig. 4.6.

The coefficients determined by Sanders and DePristo for the LJ potential are based on the strength of the electronic bond in the crystal. Its dipolar behaviour at long distance only describes the change in interaction strength. This potential overestimates the attractive interaction as pointed out by Amar [10]. On the basis of an analysis of the interaction of the electro-magnetic interaction of a Cu atom with a half infinite surface, he concludes that the dipole-dipole interaction is overestimated by a factor 5. He proposes to use the Zaremba potential [35] with appropriate coefficients to describe the dipolar interaction.

The Zaremba potential

The Zaremba potential [35] ϕ_{Zar} at a height z_a above a half infinite crystal is given by:

$$\phi_{Zar} = -\frac{c_Z \xi^3}{(z_a - 1.4\,\text{Å})^3} \tag{4.4}$$

For Cu $c_Z = 0.6522$ eV and the height z_a of the incoming atom is taken with respect to a plane through the center of the atoms of the flat surface. This semi-infinite crystal approximation neglects surface morphology and is as such not appropriate for studying steering effects.

The LJ pair pair potential can be used to calculate the potential for a semi-infinite fcc(001) surface, $\phi_{SDP,\infty}$. This gives

$$\phi_{SDP,\infty} = -\frac{\sqrt{2}\pi}{6}\frac{c_{L6}\xi^3}{(z_a - 0.9\,\text{Å})^3} \tag{4.5}$$

The Zaremba and LJ semi-infinite crystal equations are almost the same. There only difference is their offset (1.4 vs. 0.9 Å), but this is negligible at a large distances. At small distances, the semi-infinite crystal approximation can not be used as it neglects the local effect of individual atoms. The long range dipole dipole strength for the LJ potential can be taken from this by $c_{L6} = \frac{6}{\sqrt{2}\pi}c_Z$.

A modified potential

A change of the c_{L6} parameter affects the cohesive energy and the lattice constant. With this new value, they are no longer appropriate to describe the short range interaction. Sanders and DePristo used the LJ shape only as this provides a convenient mathematical formulation for the potential shape. A correct cohesive energy and lattice constant can be obtained by adding an additional attractive term to the long range 6^{th} term. Short range behaviour is obtained with a larger power and for computational reasons, a term with an even power is preferred. We explored a power 8^{th} term to describe the short range interaction, while for the repulsive part a power 10^{th} term is used. This provides the modified potential ϕ_M

$$\phi_M = \frac{c_{A10}}{(r/\xi)^{10}} - \frac{c_{A8}}{(r/\xi)^8} - \frac{c_6}{(r/\xi)^6} \tag{4.6}$$

where $c_6 = 0.1689$ eV, $c_{A10} = 1.843$ eV and $c_{A8} = 2.118$ eV. This pair-pair potential as well as the change in potential energy is shown in fig. 4.6.

A short range potential

The LJ potential developed by Sanders and DePristo, ϕ_{SDP}, was parameterized on the nearest neighbour distance and the condensation energy. These values are determined by the electron overlap interaction as also taken into account by an EAM potential that comprises only short range interaction due to electron overlap. This limited range behaviour can be simulated with an LJ potential by using a cut-off function that limits the interaction range of the ϕ_{SDP} potential. The interaction potential is multiplied by the cut-off function f_{co} determined by the pair-pair distance r.

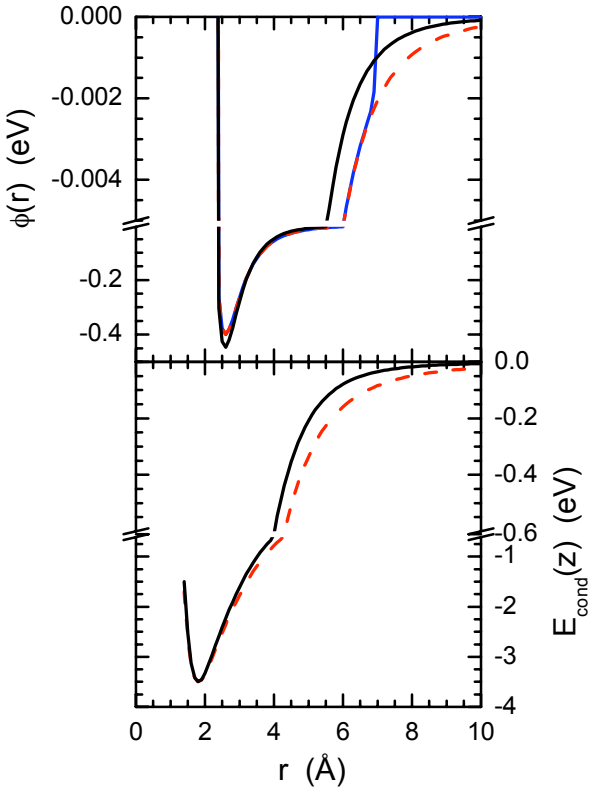

Figure 4.6: (Top panel) Pair-pair potentials for the Sanders and de Pristo potential ϕ_{SDP} (red dashed line), the modified potential ϕ_M (solid black line) and the short range potential ϕ_{SR} (blue solid line). (Bottom panel) The potential energy of a kink atom above its condensation position on a Cu(001) surface for the two potentials ϕ_{SDP} and ϕ_M. The modified potential is similar to the Zaremba potential above 6 Å.

$$r \leq r_c \qquad f_{co} = \frac{\left(r^2 - r_c^2\right)^2}{(r^2 - r_c^2)^2 + Q^2} \tag{4.7}$$

$$r > r_c \qquad f_{co} = 0 \tag{4.8}$$

A cut-off distance $r_c = 7$ Å is used and for the factor $Q = 0.65$ Å^2 is used. The method and the value of the factor Q are similar to reference [36]. The cut-off distance is slightly higher than the value in reference [36]. Due to the relative strong long range steering of the ϕ_{SDP} a significant loss (10%) of condensation energy occurs if the cut-off is set to 5 Å. The loss at the used cut-off distance is 3%.

4.3.3 Trajectory calculations

The influence of an attractive potential on an atom's trajectory is illustrated in fig. 4.7. It highlights the change in angle of incidence for an atom approaching a half infinite crystal. A change in incidence angle starts already far away from the surface. The influence of a lateral variations in the morphology is washed out at a large height above the surface and all particles experience a similar change in velocity towards the surface. At a height of 40 Å above the surface this has resulted in a reduction of the polar angle of incidence of 0.2° for a particle starting at a velocity of 770 m/s at an angle of incidence of 80° from the normal calculated with the ϕ_{LSD} potential which has a relative strong long range strength. Below typically 40 Å the local variation in potential becomes important. The trajectory below this height is based on the summation of the energy contribution given by the pair pair potential of all atoms in the semi-infinite crystal. The substrate is divided in three segments as shown in fig. 4.8 for the summation of the potential energy: the *environment* segment, the *local correction* segment and the *semi-infinite crystal*.

The largest contribution to the potential energy is from the half infinite crystal. Unlike the other segments, the individual dipolar interactions are not calculated, but the potential for the whole semi-infinite crystal is used, according to eq. 4.5. This potential provides the general perpendicular attraction of the bulk of the material. No lateral force acts on the incoming particle as a result of this potential.

The height above the surface is taken with reference to the deepest exposed layer within the environment segment. This environment segment is a $2R_{\mathbf{environment}} \times 2R_{\mathbf{environment}}$ area around the incoming atom. It changes with each new position evaluated and contains the details of the local morphology. Especially the lateral force acting on the incoming atom is obtained from this layer.

The local correction layer is only present if the height of the atom is less than z_{cor}. This layer assures that also for a relatively flat surface a lateral corrugation

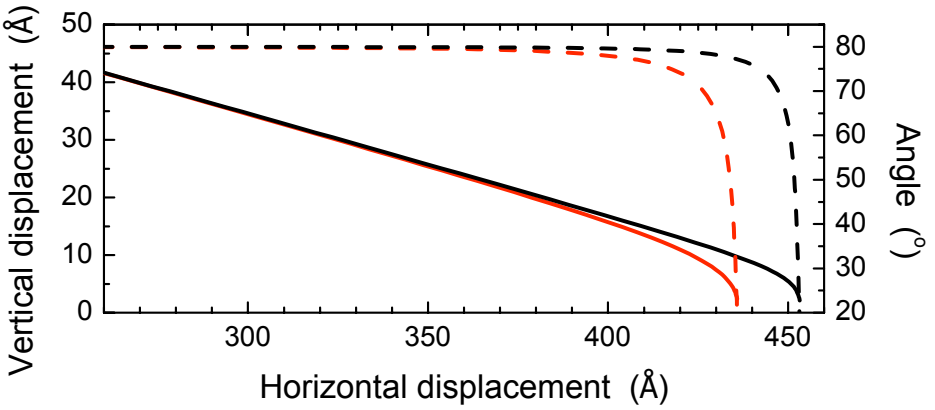

Figure 4.7: Track of an incoming atom above a flat Cu(001) surface evaluated for the modified potential ϕ_M (eq. 4.6) (black solid line) and the Sanders and DePristo potential ϕ_{SDP} (eq.(4.3)) (red solid line). The dashed lines indicate the angle of the velocity of the particle with the normal. Start velocity 770 m/s. Maximum velocity approximately 2300 m/s. Original angle of incidence 80°.

Parameter	Value	Unit
$R_{environment}$	23.0	Å
z_{cor}	7.2	Å
R_{local}	10.0	Å
Δz_{dalcor}	1.8	Å

Table 4.2: Deposition window settings.

given by the periodicity of atoms is present. This lateral corrugation is absent in the evaluation of the semi-infinite crystal layer. The local correction layer has a lateral extension of $2R_{\mathbf{local}} \times 2R_{\mathbf{local}}$ and a thickness of Δz_{dalcor}.

Table 4.2 gives the values for the parameters used. It was found that a larger window does not lead to a different condensation site of an atom. This provides the relevant criterium for these parameters.

The actual trajectory is calculated with the Verlet algorithm. This is an efficient and accurate fourth order algorithm for Newtonian dynamics ($F = m \cdot a$). The time efficiency is important and one trajectory evaluation with this scheme costs only 1ms. A simulation of a deposition of 40 monolayers requires the evaluation of about 10 million trajectories. The trajectory evaluation is a small contribution to the total evaluation time. The reasons for this efficiency are threefold: The simulation approximates the surface as a rigid lattice. This leaves only one dynamical motion, the incoming atom. Furthermore, it approximates the bulk atoms as a semi-infinite

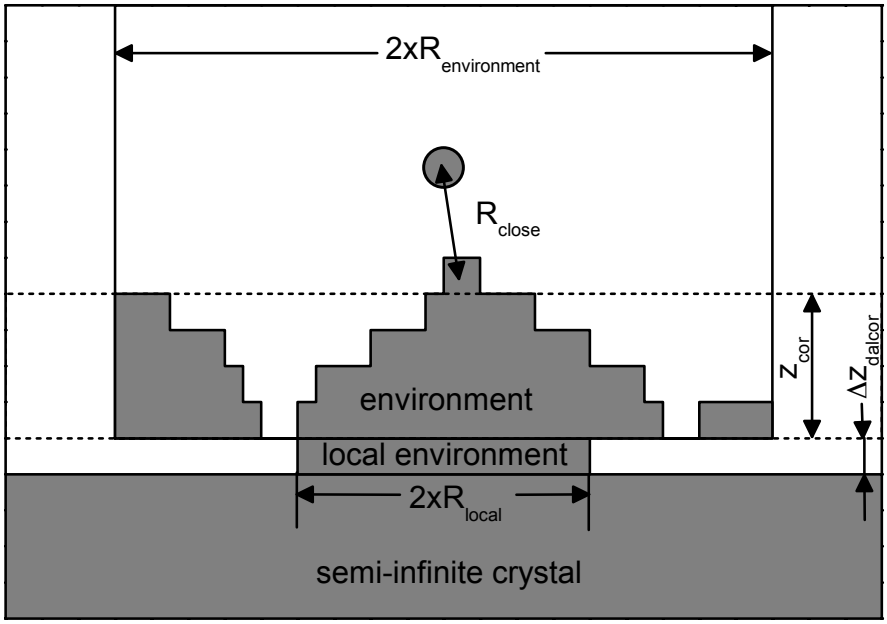

Figure 4.8: Semi-infinite crystal and included atoms for track calculation. Three different areas are shown: 1) the heterogeneous growth front denoted *environment*, 2) the $semi-infinite\ crystal$ represented by a potential that only depends on the height z, and 3) *local environment* which is a local correction for the corrugation of semi infinite crystal.

crystal. The use of dynamical time steps provides the final efficiency step. The time step is adjusted to the local change in potential. A large change in potential occurs near the surface, resulting in a decrease in the time step size in the evaluation of the trajectory. Just in front of the surface, the strong short range is important and also the full dynamics of the lattice can influence the eventual condensation position. This possibility has been evaluated with full Molecular Dynamics simulations. The results of these are presented in chapter 6. It is concluded that the condensation position can be evaluated for a rigid lattice using a simple condensation rule.

4.3.4 Flux distribution

The influence of steering can be made visual by calculating the local flux and image the flux heterogeneity for a specific morphology. A homogeneous distribution several tens of atom heights above the surface is used as a starting point. For each atom area at this height, typically some 100 homogeneously distributed trajectories are evaluated. A predeposited 5 ML film is used to illustrate the flux heterogeneity as a result of grazing deposition, see fig. 4.9. For normal incidence only the step edges have a slightly higher flux as a result of a 1.5 times larger capture zone for a condensation position in front of the stepedge. For grazing incidence a large enhancement of the flux at on top of the ascending edge is noticed. The enhanced capture zone for this flux is on the high terrace side of the step edge. Behind descending edges a large depletion of flux is observed for grazing incidence deposition. This depletion is larger behind higher mounds.

4.3.5 Conclusion

This chapter describes a simulation model for homoepitaxial growth of Cu. The model needs a priori information, like a complete set of activation barriers, and a description for the steering force calculation applied by the morphology on the incoming atom. Biham and coworkers provided the necessary intralayer diffusion barriers for Cu. With this set sub monolayer growth can be simulated between 200 and 500 K. To simulate thicker film growth, additional interlayer barriers are needed. Various values are found in literature, but so far none gives a reasonable morphology. In the next chapter a precise value for these barriers is obtained by combining experiment and simulations. Having then a complete set of activation barriers, a new study is applied to find the correct long range interaction strength between morphology and incoming atom. As a result a complete model plus the needed input is created to simulate growth at different temperatures, flux, and deposition geometries for homoepitaxial growth of Cu. The above scheme to produce a working model plus input parameters,

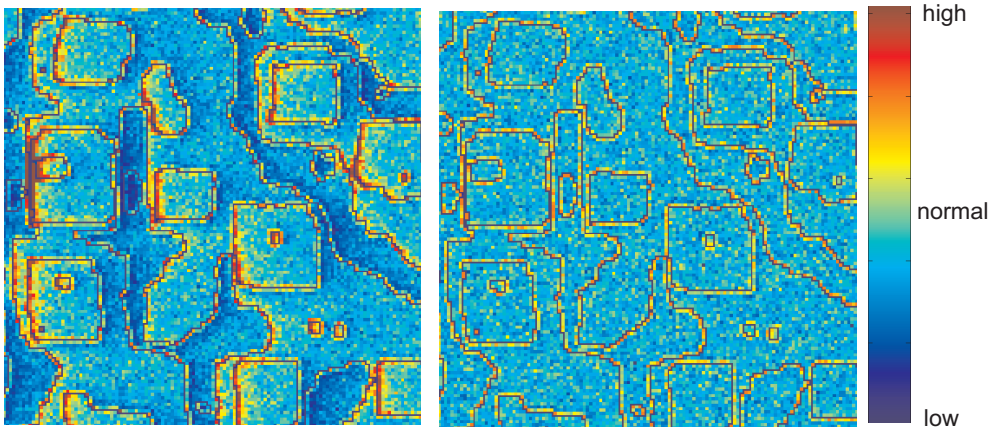

Figure 4.9: Flux heterogeneity on a surface with a predeposited 5 ML film for grazing incidence (left) and normal incidence (right). The calculation is done using the modified interaction potential.

can also easily be applied for similar metals like Ag, Au and Ni.

For doing research with the simulation model, suppression techniques for fast processes are necessary to get the simulation done within reasonable times. A carefully selected algorithm is given by Biham which works fine for submonolayer growth. It is further optimized for accurate simulations of thicker film growth. The suppression technique is expected to work equally well for homoepitaxial growth of Ag, Au and Ni.

CHAPTER 5

Determination of the step and kink Ehrlich Schwoebel barriers on Cu(001)

5.1 Introduction

A large variety of diffusion processes on surfaces is at the basis of various kinetic growth modes and film morphology. Homoepitaxial growth provides an excellent playground for the study of the relation between the elementary diffusion processes and their collective outcome. The deposition of the same material assures the development of largely strain-free adlayers or multilayer films. Even in the case of homoepitaxial growth adatom- (or vacancy-) structures may result in strain effects and as a result electronic consequences [37–40]. Although there is some experimental evidence for strain in homoepitaxial systems [12, 41], these effects are quite minor. Therefore, we neglect these features and consider the fcc lattice model, i.e. the atoms at/near the surface occupy bulk-continued lattice sites, as a realistic framework for modeling the growth dynamics. In this approximation the diffusion processes are modeled as attempts to move an atom from one position to a neighbor position with a rate depending on its local surrounding (see chapter 4). Two specific activated diffusion processes have to be distinguished, see fig. 5.1, intra- and interlayer diffusion processes. These determine to a large extent the morphology of the growing film (growth

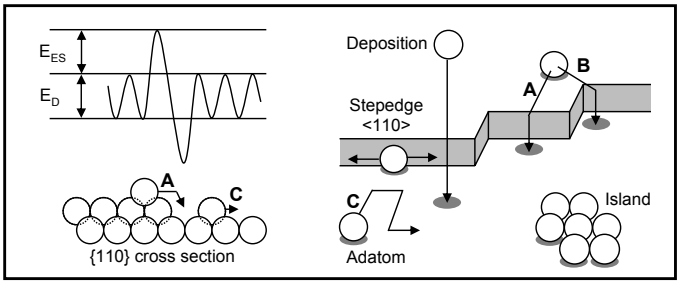

Figure 5.1: Schematic picture of diffusion processes on a surface. The image on the right shows next to adatom and step edge diffusion also the two relevant interlayer diffusion pathways: via the close packed step edge or via kinks. The bottom left depicts the situation near a step edge. The top left image shows the potential surface near this step edge, where E_{dif} represents the activation barrier for the intralayer diffusion of an adatom and E_{ES} the extra barrier for an interlayer diffusion.

front). We distinguish three kind of growth modes: rough or multilayer growth and smooth growth or layer-by-layer growth and step flow growth. Precise knowledge of the rates of the various diffusion processes is required to understand the observed growth behaviour at a specific temperature and deposition flux.

Only a few very elementary diffusion barriers are accessible for direct experimental observation. The barriers for most diffusion processes are obtained from calculations. Usually molecular dynamic simulations, employing an embedded atom method potential are used for their theoretical evaluation. In this, the minimum energy path of a diffusion process is simulated from the start position of an atom to its final position, while allowing the system to fully relax. The diffusion barrier is found from the difference between the highest energy along this path with respect to the initial energy. Furman and coworkers [28, 42] used this method to produce a complete set of intralayer diffusion barriers for Cu on Cu(001) and other similar surfaces. This set of barriers was used in a kinetic Monte Carlo (kMC) simulation of the diffusion and deposition process. They obtained a good correspondence between these simulations and the island shape and density in the early stages of submonolayer growth as observed in experiments over a wide range of temperature and flux. Long jumps as reported on Pt(110) [43], may in principle exist on Cu(001). However, such events are not expected for the (low) temperature range considered here.

Since the experimental work of Ehrlich [29] and the theoretical work of Schwoebel [30] the diffusion process across a step edge is known to differ from diffusion on a terrace. Such interlayer diffusion processes are usually characterized by an additional

barrier, the Ehrlich Schwoebel (ES) barrier, added to the activation energy for diffusion on a terrace, see fig. 5.1. Usually this barrier is positive and typically of the order of 60 meV [44, 45] for (001) terraces up to a value of a few hundred meV for close packed terraces. It has been noted that the ES-barrier may be negative, implying that descent across the step may require less thermal activation than migration back onto the terrace [44].

The interlayer mass transfer processes are crucial in the balance between rough growth and layer-by-layer growth. Without mass transfer between terraces, a rough growth front develops with a characteristic length scale set by the intralayer processes during very early stages of growth. Only if this length scale is similar to or larger than the step-step distance determined by the (local) vicinality of the surface an extremely smooth growth front can develop, i.e. the growth proceeds by step flow. The homoepitxial growth on Cu(001) is known to show all three kinetic growth modes, depending on the deposition temperature and deposition rate, see [46] and references therein [47–51]. This implies that temperature dependent paths for interlayer mass transport are available. Two of these, see fig. 5.1, are the transport across the thermodynamically favored ⟨110⟩ step edge, as well as across the ⟨100⟩ step edge. The latter is also associated with diffusion processes across kink sites in a ⟨110⟩ step edge. The relative importance of these two processes depends on both the energy barrier for diffusion as well as the abundance of the actual pathways. The latter implies that the shape of adatom islands, i.e. the relative presence of ⟨100⟩ step edges also influences the growth dynamics. The influence of shape was used first to explain the reentrant layer-by-layer homoepitaxial growth on Pt(111) [52]. The combination of these factors leads to complex interlayer mass transport in which the barrier for diffusion itself is not the only relevant parameter.

In their STM study of the decay of a large 3D-island with predominantly ⟨110⟩ steps, Li et al [53] showed that on the Cu(001) surface the kinks in the ⟨110⟩ steps are the preferred sites for interlayer mass transport. This selective side descent mechanism occurs on a surface on which at least two different paths for interlayer diffusion are present, the straight ⟨110⟩ step edge and the kinks in this step. However, the latter pathway is associated with a much lower ES barrier than the first one. The theoretical study by Trushin et al [44] shows a similar difference. An ES barrier of 60 meV has been evaluated for diffusion across the close packed ⟨110⟩ step, while a negative barrier of -160 meV was obtained for diffusion paths across a kink site. This negative barrier implies that the presence of kinks facilitates the interlayer mass transport. The difference in mass transport across the ⟨110⟩ and ⟨100⟩ step edges was also found to explain the orientation of the etch pit structures on Cu(001) [54]. Similar etching behaviour was previously found for Ag(001) by Teichert et al. [55]. The ES barriers

on the Ag(001) surface were also evaluated with molecular dynamic simulations also providing a negative ES barrier for kink sites [56]. Alternatively, the ES barrier of the close packed step edge was determined by comparing kMC simulations and the experimental film width (roughness) as obtained with STM [57]. With the assumption that the ES barrier of a kink site is zero, an ES barrier of the close packed step edge of 70 $\pm$ 10 meV [57] was found for Ag(001). This value was verified with a different experimental approach in which the amount of material in the second layer after deposition of one monolayer (ML) was used [58].

The reported energy values for the different interlayer transport paths agree qualitatively, all exhibiting that diffusion via kinks is easier than via steps. Quantitatively, the different values result in different roughness of the simulated film. The lowest values of the ES barriers reported result in smooth layer by layer growth at $T = 250$ K for homoepitaxial growth of Cu(001), while the highest values result in a rough growth front. A precise determination of these barriers is mandatory to understand multilayer growth. Experimentally the evolution of the growth front is easily measured with an *in-situ* diffraction technique as it provides directly a measure of the surface roughness. Thermal Energy Atom Scattering (TEAS) probes only the very surface and is in this case the best choice. Around 250 K, Poelsema et al [51, 59] showed, that in an out-of-phase condition, the specular reflected peak height shows oscillations with several maxima and minima. A gradual turn over from layer-by-layer growth towards rough growth was found. The developed film roughness depends on the temperature and deposited amount of material. In this chapter we will compare the growth front evolution recorded experimentally with detailed simulations. In these simulations both the ES barrier across the close packed $\langle 110 \rangle$ and the open $\langle 100 \rangle$ step edge are varied. This approach offers a powerful way to set a quantitative window for both barriers.

5.2 Experimental setup

All experiments were performed in an UHV setup with a base pressure $< 10^{-10}$ mbar. The sample was cleaned by sputter anneal cycles using 800 eV Ar ions and annealing at an annealing temperature of 750 K. This resulted in an impurity level below the Auger Electron Spectroscopy (AES) detection limit. Further cleaning was checked with High Resolution Low Energy Electron Diffraction, which ultimately showed an average terrace length above 100nm [5, 6, 8, 12, 41, 51]. The homo-epitaxial growth experiments were in-situ monitored with Thermal Energy Atom Scattering (TEAS) [51, 59]. A thoroughly desulfurized thermal evaporation Cu source was used. The TEAS system has a transfer width of about 25 nm and contamination by the He beam was minimized by using 6.0 He that was further purified

by a liquid nitrogen trap. Under these conditions the contamination level remained below the detection limit of AES.

5.3 Experimental results

The intensity change of a He atom beam has been used in several studies of the homoepitaxial growth of Cu(001) [5, 48, 50, 60–62]. The temporal evolution of the height of the He specular beam under out of phase conditions during deposition is a sensitive monitor for the development of the roughness of the growth front. Figure 5.2 shows the profile of the specular beam for a clean surface and after deposition of 1 ML at 270 K. Both profiles are normalized to the maximum height recorded. The profile of the Bragg peak recorded after 1 ML deposition is indeed very similar to that of the clean surface. The similarity implies that the height of the specular He beam can indeed be used as a measure for the integrated Bragg intensity.

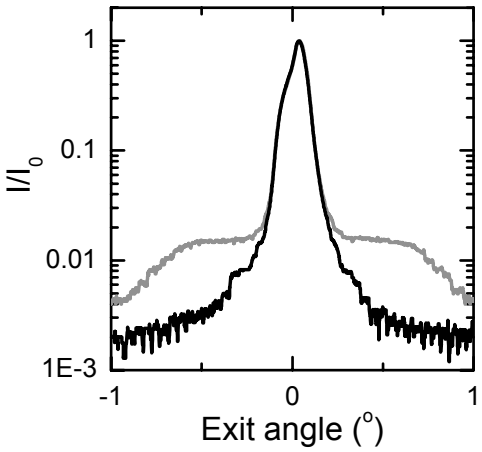

Figure 5.2: Normalized He specular beam profiles of the initially smooth Cu(001) surface (black curve) and after deposition of one monolayer at 270 K (gray curve). The profiles are measured at an out-of-phase condition. The exit angle indicated is relative to the out-of-phase condition. The peak shape reveals some mosaicity of ($< 0.1^\circ$) the substrate within the illuminated spot.

The normalized height, I/I_0 of the specular reflected He beam under an out of phase condition depends on the balance between the exposed surface fractional integrated areas of the odd and even layers. If, for the moment being, we disregard the influence of diffuse scattering from point or line defects this intensity is normalized

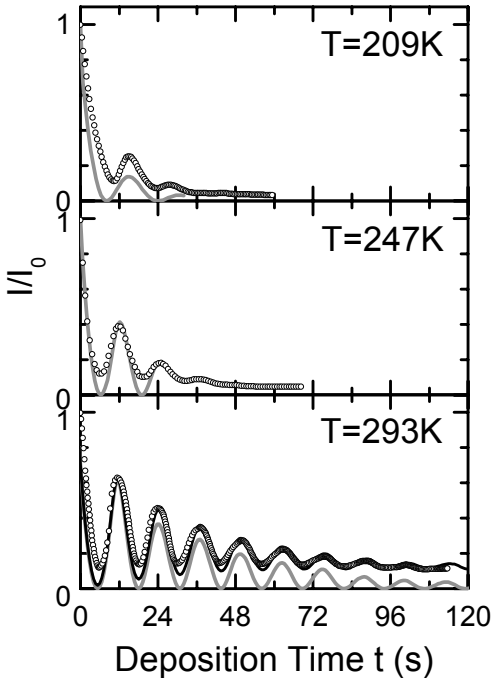

Figure 5.3: Temporal evolution of the normalized specular He peak height I/I_0 during homoepitaxial growth of Cu(001) at substrate temperatures of 209, 247 and 293 K (∘) and the result of simulations (gray line). For 293 K also the simulation result corrected for the finite instrumental resolution is shown (black line).

to the intensity of the initially smooth surface I_0

$$\frac{I}{I_0} = (\sum_{i=even}(\theta_i) - \sum_{i=odd}(\theta_i))^2$$

with $\sum_i(\theta_i) = 1$. Figure 5.3 shows some representative variations of the height of the specularly reflected He-peak during deposition in the temperature range studied. The deposition rate amounts to about 5 monolayers per minute. At low temperature (209 K) only two small maxima can be discerned. The low value of the first maximum indicates that already substantial nucleation of adatom islands in the second layer has occurred before completion of the first layer. The interlayer mass transport channels are substantially activated at 247 K. Around room temperature up to nine oscillations can be observed indicating a more pronounced layer-by-layer growth mode.

The values of the first and second intensity maxima were used as a measure of the initial roughening of the interface. For the temperature range of 210 - 310 K the

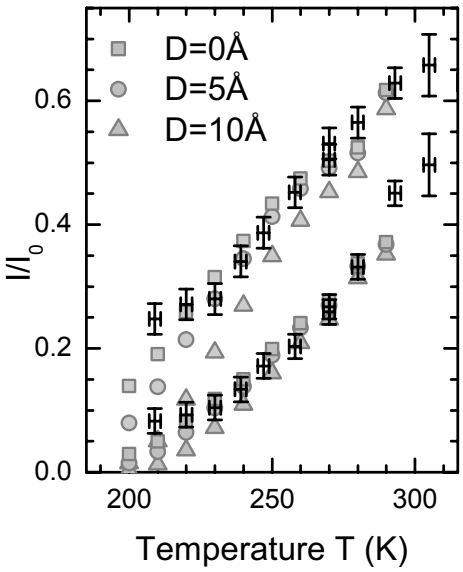

Figure 5.4: Intensity of the first and second maximum in the He reflectance curve as a function of temperature (+). The values are normalized to their value for the smooth surface at the respective temperature. Also indicated are the simulated specular He reflectance data with and without taking into account diffuse scattering by step edges, see text. (□) no diffuse scattering, (○) a 5 Å and (△) a 10 Å wide zone along the step edge is regarded to contribute to diffuse scattering.

height of these maxima is depicted in fig. 5.4. Above 230 K the growth proceeds in a more smooth way with increasing temperature. Below 230 K much less temperature dependence is observed, indicating that the roughness of the surface after 1 ML deposition does not depend strongly on temperature in this range. This indicates a reduced activity of diffusion processes on the surface. If one makes the reasonable assumption that around monolayer completion (i.e. around the first and second maxima) one is dealing with effectively a three exposed layers system we can determine the layer distribution of deposited material. At the first maximum the amount of material in the second layer follows from the deficit of the normalized specular He peak height by:

$$\theta_2 = \frac{1}{4}\left(1 - \sqrt{\frac{I}{I_0}}\right)$$

The amount of material in the second layer is thus only about 9% at 247 K and 5% at 293 K, illustrating the sensitivity of this method on surface roughness.

Figure 5.5: Calculated morphology after deposition of 80% of a monolayer. The images shown are 16x16 nm^2. The used suppression factor α is: 0.4 (left), 0.6 (center and right), respectively. For the calculated morphology in the middle panel additional vacancy suppression has been used as discussed in the text.

5.4 Growth Simulation Scheme

The presence of activated diffusion paths on the Cu(001) surface allows to simulate the growth with a lattice model in the kinetic Monte Carlo (kMC) scheme. The growth is simulated on a substrate with 512x512 lattice sites per Cu(001) layer and periodic boundary conditions. For a given morphology, the rates of all diffusion pathways are added to the deposition rate and a random number generator determines whether a deposition process and if not so which diffusion process is performed. The rates of the diffusion processes are determined by their activation barrier, assuming a fixed frequency factor of 10^{13} s^{-1}. For intralayer diffusion processes Biham et al. [28] evaluated activation barriers by comparing experimental results and kMC simulations. Their tabulated activation energies on Cu(001) depend on the presence of the nearest and next nearest neighbor atoms in the same layer. Due to symmetry, a set of 72 independent energy barriers was obtained (see also chapter 4). To facilitate multilayer growth two interlayer diffusion barriers are added to the simulation. These two diffusion paths describe the likelihood of mass transport across the $\langle 100 \rangle$ and $\langle 110 \rangle$ step edges. An additional barrier is introduced for both pathways, simulating the presence of an Ehrlich Schwoebel barrier. Kink sites frequently present in the energetically favoured $\langle 110 \rangle$ step edge, are treated as $\langle 100 \rangle$ microfacets. To prevent overhangs, an immediate downfunneling process is incorporated.

This simulation scheme is already quite demanding for submonolayer growth at a relevant temperature of 250 K [28]. At this temperature interlayer transport becomes significant, i.e. growth becomes smoother, which can be concluded already directly from the presence of the first and second maxima in the He oscillation shown in fig. 5.3. It is thus important to be able to simulate at this temperature and a few tens of Kelvin higher. At these higher temperatures, most of the simulation time is spent on fast processes that do not alter surface morphology like step edge diffusion.

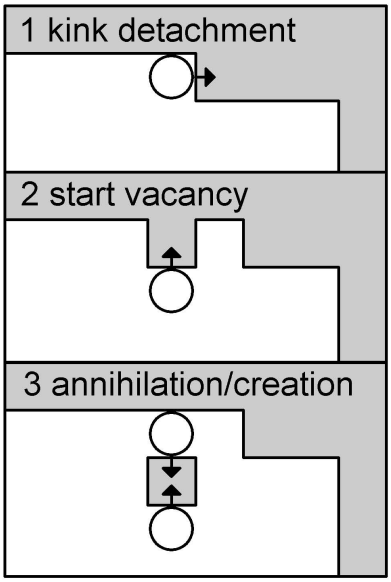

Figure 5.6: Vacancy creation/annihilation process near a kink site. The first step is a kink detachment move, followed by the outward move by the atom indicated. The actual vacancy is created or annihilated in step 3. The kink detachment has a relatively high energy barrier and limits the number of vacancy creation attempts.

Therefore, we follow Biham et al [28], who incorporated an artificial suppression of paths with an energy barrier below 400 meV to suppress spending too much time on these fast processes. The diffusion energy E of these paths is artificially increased with a factor α $(400\ -E)$ meV. This suppression has to be done with great care as the change of some processes may influence the morphology of the grown film. As an illustration, fig. 5.5, shows the influence of the suppression parameter α. The left and right hand image show a distinct difference in the relative number of $\langle 110 \rangle$ and $\langle 100 \rangle$ step edges. The difference in morphology as a result of the suppression of fast processes is not due to a change in island density in the early stages of growth, but is the result of a change in island shape. This is the result of a decreasing kink density with increasing suppression, i.e. the islands become more compact. The reduction in kink density will alter the balance of the two pathways for interlayer mass transport in the simulation scheme and thus change the roughness of the grown interface. This decrease in kink density can be traced back to a change in the creation/annihilation balance of vacancies. A vacancy can be created by a detachment of a kink atom to a step edge position, see fig. 5.6. This detachment step is almost always followed by the opposite move, a vacancy annihilation process. However, the vacancy can also

survive and as a result the initial kink has moved one position towards the island corner. The vacancy creation and annihilation are fast processes with respective energies of 280 meV and 50 meV. At 250 K the annihilation is 43.000 times more likely to occur and as a consequence hardly any vacancies are produced. For $\alpha = 0.6$ this preference has diminished to a factor 71 and the artificial creation of vacancies becomes a more important factor. A gradual movement of the kink results in more compact islands, changing also the pathways for interlayer mass transport and explain the differences observed in fig. 5.5. Note that these findings also illustrate that for elevated temperatures vacancies can be an important ingredient in the growth process. Their role in growth has been suggested previously [63]. The increase of the various energy barriers for a more efficient algorithm has thus to be done with great care in regard to the balance of creation and annihilation of vacancies. This is achieved by reducing the probability of vacancy creation and restoring the more than 10.000 times larger change for annihilation than creation. The effect of the suppression with and without vacancy creation suppression is illustrated in fig. 5.7. The density of atoms in all step edge positions is shown as a function of coverage for suppression with and without additional vacancy suppression. The density of step edge atoms shows a maximum at 0.5 ML coverage in the first layer and for islands in the second layer around 1.5 ML. A similar number of step edge atoms in the first and second layer occurs around 1 ML. This indicates that the vacancy islands in the first layer are of about the same average size and shape as the adatom islands in the second layer. The different suppressions show a very similar density of steps. However, a difference in the density of kink atoms is found for the different suppression schemes. This difference in density is especially critical near the completion of a layer. At this stage a deviation in the ratio between both availability of transport paths, affects the growth front. The situation of $\alpha = 0.6$ without vacancy suppression shows a lower density of kink sites between 0.8 and 1 ML than with vacancy suppression. The latter situation is quite similar to suppression with $\alpha = 0.4$. The influence on the morphology of these three situations is depicted in fig. 5.5. Without vacancy suppression and $\alpha = 0.6$ longer straight step edges are observed. A higher value like $\alpha = 0.8$ as used by Biham et al [28] can only be used for the study of island nucleation in the initial stage of growth. For the simulations used in this study we used a value of $\alpha = 0.6$ with vacancy suppression.

An important test of the validity of the simulation results is given by the average island separation L. This characteristic length can be obtained experimentally as a function of temperature after deposition of 0.5 ML with HR-LEED measurements from the radius of the diffraction ring [5, 64]. The measured average island separation is shown in fig. 5.8 as well as those obtained from the simulations. The calculated

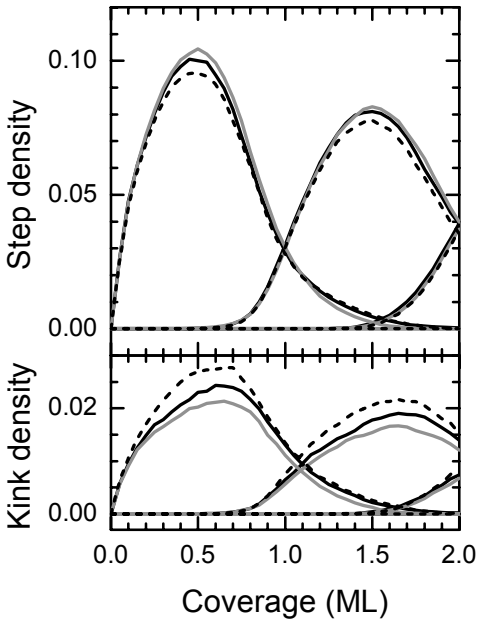

Figure 5.7: (top) Evolution of the density of step edge atoms on the simulated lattice with coverage for suppression factors $\alpha = 0.4$ (gray line) and $\alpha = 0.6$ (dashed line) at a temperature of 250 K. Also shown is the influence of vacancy suppression for $\alpha = 0.6$ (solid black line). Indicated are the densities in the first, second and third layer. (bottom) The same but now for the density of kink atoms.

values were obtained from diffraction images evaluated for the simulated morphologies. This provides an equal base for the length scale determination. The similarity between experimental data points and simulations is within statistical error margins. Such a similarity is not very surprising. Figure 5.8 also shows a solid line that depicts the relation between the island separation L and temperature T based on nucleation theory [65, 66]. The adatom diffusion energy, i.e. 0.48 eV and the assumption that a dimer is a stable nucleus provides the slope of the shown curve. The offset is chosen to give the best fit. Although the simulation contains a manyfold of diffusion processes, the adatom diffusion plays a dominant role in the determination of the $L - T$ dependence. However, many other diffusion processes determine the offset and this interplay is well represented by the kMC simulations.

The deposition process is simulated taking into account the attractive interaction between an incoming atom and the substrate. The incorporation of these forces gives rise to enhanced flux on protruding parts and accordingly reduced flux on indented parts. This steering effect is especially noteworthy for grazing incidence deposition

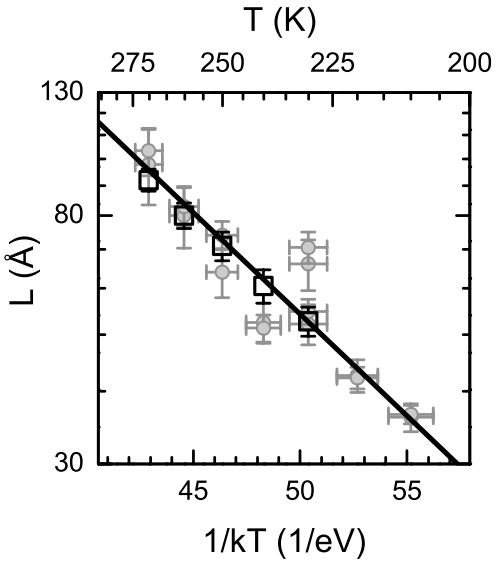

Figure 5.8: Average island separation L after 0.5 ML deposition versus substrate temperature evaluated from HR-LEED experiments ∘ and from diffraction patterns of the simulated morphologies □. The solid line indicates the distance - temperature dependence predicted by rate equations based on the adatom diffusion energy and assuming a dimer as stable nucleus [65].

[6]. At normal incidence this effect is also present but small [11, 33] and results in an upward funneling contribution. Yu and Amar [11] only considered short range interaction and propose to incorporate this upfunneling by an additional capture zone around an island with a size of 30% of the nearest neighbor distance. With both short and long range interaction taken into account an effective capture zone of 15% is found. In the present simulation this phenomena is dealt with through a trajectory calculation for each deposited atom, starting the deposition at a random position 20 Å above the surface and the attractive potential as discussed in chapter 6. The other potentials considered in this chapter hardly affect the results reported for the ES barriers in the present chapter.

5.5 Simulation results

The morphology evolution as a function of both the step and kink ES barriers was simulated. These simulated morphologies were compared with experimental observations by calculating the height of an out of phase specularly reflected He beam. In real

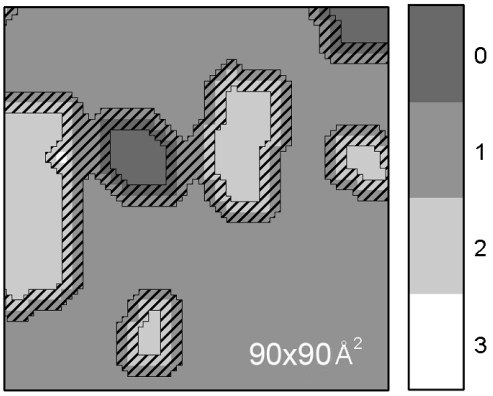

Figure 5.9: Diffusive scattering zone of 5 Å around step edge for a specularly reflected He beam. The settings for the simulated morphology are $T = 230$ K, $E_{ES\,\langle 110\rangle} = 125$ meV, $E_{ES\,\langle 100\rangle} = -3$ meV, coverage is 1 ML. Numbers indicate layer.

experiments, the intensity of this specular beam is attenuated as a result of diffuse scattering from step edges [67, 68]. Note that throughout this thesis the term diffuse scattering is used for wide angle scattering from point or line defects and explicitly excludes diffraction features sometimes referred to as "Henzler" rings.This intensity attenuation can be incorporated in the simulated intensity oscillation by neglecting the contributions from a zone around the step edges, see fig. 5.9. TEAS is very sensitive to disorder on the surface [69, 70] and for Cu(001) the diffuse zone around the step edge was roughly estimated at 13 Å [68]. This value is almost certainly too high since a more reliable value was determined for Pt, ≈ 10 Å [17]. Note that this value for Pt (atomic number Z = 78) is expected to be significantly higher than that for Cu (Z = 29). Therefore, we elected a value of 5 Å to be typically used in the simulations and its influence is discussed below.

Figure 5.10 shows the dependence of the out of phase normalized height of the specular He-peak on the step- and kink-ES barriers on the intensity after the deposition of 1 ML at 240 K. A low He reflectivity is found for a combination of high ES-barriers for both stepedge sites, leading to rough growth fronts. Low ES-barriers result in only a small amount of material in the second layer at the position of the first maximum in the oscillations. Experimentally a normalized He specular peak height of 0.32 ± 0.03 was found for this temperature, see fig. 5.4. This intensity could be reproduced in the simulation by a non-unique combination of the step and kink ES barriers. The width of the intensity areas in fig. 5.10 reflect the combined accuracy of experiments and simulations. The influence of the two ES-barriers on the rough-

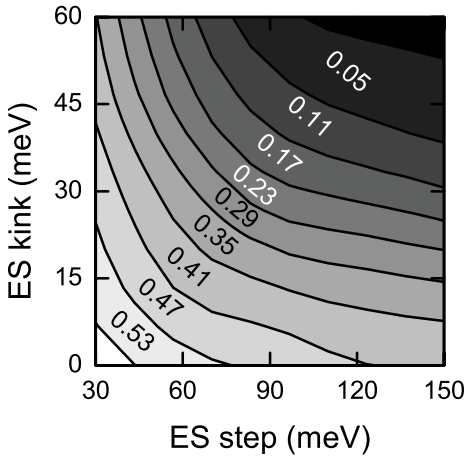

Figure 5.10: Calculated normalized He specular peak height at the first maximum as a function of the two ES barriers after deposition of 1 ML at $T = 240$ K.

ening of the surface depends on the substrate temperature. Therefore, a different combination of the two barriers that provide the experimentally observed intensity is obtained for another temperature. Figure 5.11 shows the ES barrier window that gives rise to an unique agreement between the calculated and measured normalized heights of the specular He-peak at the first maximum in the peak height oscillations obtained at respectively, 230, 240, 260, 270 and 290 K. Also included, denoted with the dashed curves, are the results for the comparison of the simulated and measured intensity at the second maximum in the intensity oscillations for deposition at 260, 270 and 290 K. This combination of simulations and experimental observations allows to determine a narrow window of allowable ES barriers for descent via kink sites and a lower estimate for the ES-barrier for crossing straight $\langle 110 \rangle$-steps. For the close packed $\langle 110 \rangle$ step a lower limit of $E_{ES\,\langle 110 \rangle} = 120$ meV is found. The barrier for the kink site, or $\langle 100 \rangle$ step is determined at $E_{ES\,\langle 100 \rangle} = -5 \pm 3$ meV, i.e. the barrier is slightly negative. The error margin for the kink barrier is quite small as a small change of its value has a large influence on the amount of interlayer mass transport. For the close packed step edge barrier a much larger uncertainty results. The upper limit is actually inaccessible to our present method. Note that under the conditions considered here interlayer diffusion proceeds almost exclusively via kink sites. Mass transport across the $\langle 110 \rangle$ step edges is significant only for temperatures above 290 K. However, this temperature range is at this moment too challenging for computational efforts.

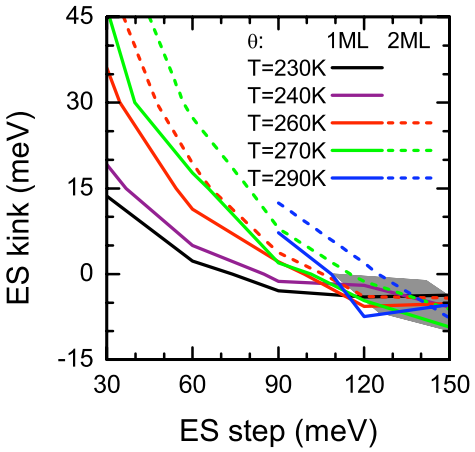

Figure 5.11: Combinations of the two ES barriers that provide the measured specularly reflected He intensity after 1 or 2 ML deposition at a temperature of 230, 240, 260, 270 and 290 K. The shaded area indicates the region of overlap of these curves taking into account the experimental and simulation accuracy.

The influence of the size of the diffuse scattering zone at step edges is also shown in fig. 5.4. The 5 Å wide zone used gives results similar to a vanishing diffuse scattering zone. A 10 Å wide zone, i.e. a zone with a width of 2 atoms on the step up and 2 atoms on the step down terrace do not contribute to the Bragg intensity, gives slightly smaller intensities with larger deviations at lower temperatures. This crude approximation towards the diffuse scattering of step edges shows that for a reasonable length scale for a diffuse scattering of up to 5 Å, the values found for the ES barriers are not influenced. He intensity oscillations at various temperatures were evaluated with the determined barriers and are compared to the experimental results in fig. 5.3. The simulated curves show much more pronounced minima as a result of the fact that the transfer width of the instrument is neglected in eq. 5.3. This shortcoming is more prominent for higher temperatures. This can be mended by a convolution of the simulated He diffraction pattern with a Gaussian broadening function with a FWHM of 1% of the Brillouin zone. This provides a He growth-oscillation curve that is highly similar to the experimentally recorded one. Note that the intensity of the first maximum is hardly affected by this correction. It is therefore not necessary to correct the simulated data for this effect for the derivation of the ES barrier.

All experiments and simulations shown were performed at a deposition rate of 5 ML/min. Figure 5.12 shows a growth experiment and a simulation at 250 K but at with a reduced flux of 0.5 ML/min. A larger number of oscillations is observed at this growth rate. Also at this very different rate, i.e about an order of magnitude lower,

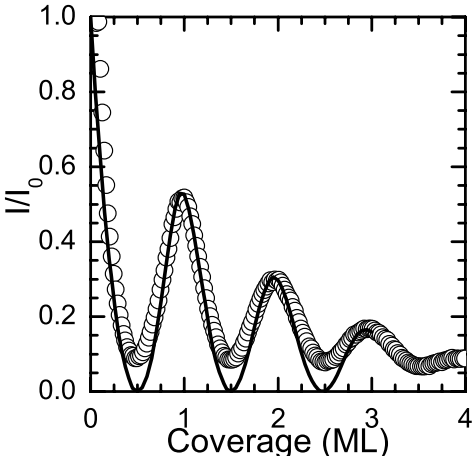

Figure 5.12: Cu uptake curve, i.e. the normalized He specular peak height for Cu(001) as a function of time during deposition at a rate of 0.5 ML/min. and at 250 K. Both experimental points ∘ and simulation results (solid line) are shown.

the simulations reproduce this measurement with remarkable accuracy.

5.6 Coarsening and interface roughening in multilayer growth

The evolution of the local interface height in multilayer growth has been described with continuum theory. Standard ingredients for such an approach are a statistical fluctuation of the deposition flux across the surface and diffusion and coarsening mechanisms. This approach is extensively described in literature and has been analyzed in the context of scaling theories for self-affine growth [71]. The scaling theory formulates three critical exponents that can be used to describe the morphology evolution in multilayer growth. The first exponent describes the shape of the islands and equals one for MBE growth with slope selection [72]. This also applies for Cu homoepitaxial growth at normal incidence. The formation of mounds implies that the morphology is not self-affine, but the two exponents that describe the evolution of the interface roughness and the change in characteristic length scale with coverage can still be used. The evolution of the length scale has been studied experimentally for Cu(001) homoepitaxy by Wendelken and coworkers [42, 64, 73] at a temperature of 299 K. They reported a relation between the separation between mounds L and coverage θ according to $L \propto \theta^n$, with $n \approx 0.23$ from STM measurements. Figure 5.13 a) shows the change in average distance between mounds L for the present simulation results. This distance was determined from the position of the minimum in the autocorrelation function of a surface morphology r_0 as $L = 2r_0$. All simulations in

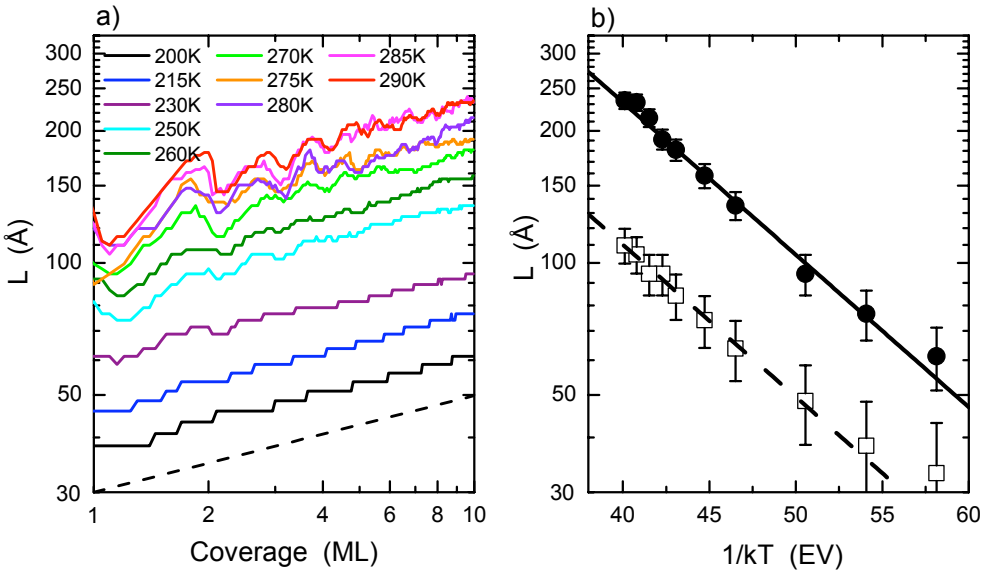

Figure 5.13: a) Change in average distance between mounds L as a function of coverage for temperatures in the range of 200 - 290 K. The distance L is determined as twice the distance of the minimum in the autocorrelation function of the morphology. b) Average distance L at 10 ML (•) and 0.5 ML (□) as a function of temperature. The lines indicate the temperature dependence expected from rate equation analysis, (c.f. fig. 5.8). These lines are fitted to L at 10 ML (solid line) and 0.5 ML (dashed line).

the range of 200 - 290 K show a similar value of $n = 0.22 \pm 0.01$, in good agreement with the experimental value at 299 K. The temperature independent, relative change of L with coverage implies that also after the deposition of 10 ML the average distance between mounds shows the same temperature dependence as adatom islands in submonolayer coverage. This is illustrated in fig. 5.13 b) which shows the relation between the average mound distance and temperature for 10 ML. Note that the latter is quite similar to fig. 5.8, but in the present figure the distance was determined from the autocorrelation of a morphology image. The temperature dependence of the average mound separation at 10 ML can still be described by submonolayer nucleation theory with the activation barrier of an adatom and assuming the dimer as the stable nucleus. This behaviour was already found experimentally by evaluating the temperature dependent mound separation after deposition of 15 ML and 20 ML. [5, 51].

The third critical exponent describes the relation between the Root Mean Square (RMS) roughness w and coverage, $w \propto \theta^{\beta}$. This exponent has been measured by several groups [62, 74] for Cu on Cu(001). Of special interest is the decrease of

this parameter with decreasing temperature below 200 K [62]. A reentrant smooth growth for low temperatures was suggested as an explanation as was first observed for Pt(111) [52]. The correspondence between TEAS data and the simulations presented allows us to use the latter with confidence to explore the temperature dependence of the roughness evolution and thus of the exponent β. Figure 5.14 a) shows the change in roughness with coverage in a temperature range of 200 - 290 K. Already at 215 K a few oscillations in the RMS roughness can be observed. A quite good initial layer-by-layer growth is especially present at high temperatures. A very different increase of roughness with coverage is observed for the various temperatures. The largest relative increase of the roughness is observed for temperatures in the range 250 - 275 K. The roughening exponent β is derived from the high coverage range in this graph. The temperature dependence of β is shown in fig. 5.14 b). An increase of β with temperature is observed between 200 and 250 K, while a steep decrease of β with temperature is observed from 280 to 290 K. The value of β at 250 K is consistent with the experimental observation from X-ray diffraction [74]. These authors noted a decrease to a value of 0.33 at 290 K, i.e. a more gradual decrease of β with increasing temperature is observed experimentally. The difference is probably the result of the polar angle of deposition of around 60° [75]. The lower value of β at 200 K differs from the experimental values of 0.5 [62, 74] at this temperature. We already noted deviations between TEAS results and simulations at this temperature, see fig. 5.4, that suggests the presence of additional diffusion pathways relevant at low temperature.

5.7 Discussion

The detailed comparison of the experimental and simulated growth oscillation curves allows to pinpoint both the ES barriers of the straight step edge and kink sites. The obtained values show that the kink positions (almost) exclusively facilitate the interlayer diffusion process in the temperature range 230 - 290 K. This is consistent with a similar observation of ion induced vacancy structures [54]. STM measurements of island decay also showed a selective site descent mechanism that favours kinks as the pathway for interlayer diffusion [53]. However, these authors used substantially higher values for the ES barriers, with 90 meV for the kink site barrier. Such a value would result in a very rough growth up to room temperature, contradicting the TEAS measurements. They used a difference between the two ES barriers of 100 meV. This study finds a minimum barrier difference of 120 meV. Note that an increase of the kink density in the simulation results in an increase of the kink barrier of only 15 meV. We believe that the kink density obtained in the simulations is well within this margin.

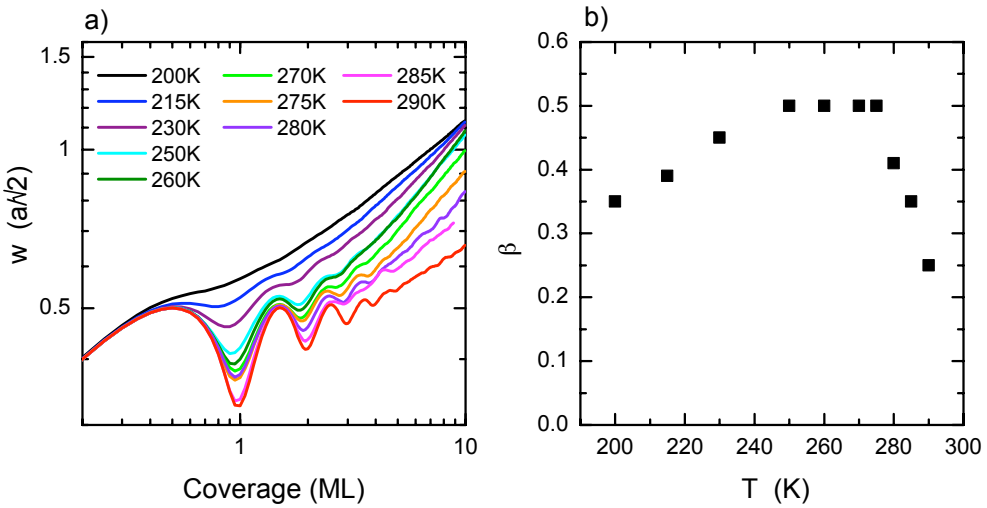

Figure 5.14: a) Increase of the RMS roughness w with coverage in the temperature range of 200 - 290 K. The RMS roughness is normalized to the interlayer distance $a/\sqrt{2}$, with $a = 2.55$ Å the nearest neighbour distance for Cu. b) The value of the critical roughness exponent β as a function of temperature.

An effective ES barrier of 125 meV was experimentally evaluated in a temperature range of 360 - 400 K by Gerlach et al. [76]. These experimental conditions are far outside our present findings. The value of the effective barrier is very similar to the lower limit of the ⟨110⟩ step edge barrier found in this work. It is quite likely that in the high temperature range the interlayer mass transport takes place predominantly across the ⟨110⟩ stepedge. The number of kink sites will be extremely small and the probability for descent across a kink site has become only about 40 times (at 400 K) more probable than interlayer diffusion across the straight step edge. Accordingly, a rough estimate than leads to the conclusion that kink concentrations of less than 1% are completely consistent with our results. Considering the huge adatom structures in the LEEM study of Gerlach et al, this is a very likely situation.

Below 230 K (see fig. 5.4), the simulations show a rougher growth front than experimentally observed. A change in growth mode at this temperature is expected from the work of Dürr et al [73]. They found that below 223 K the variation of the average distance between adatom islands with temperature was different, i.e., slower than above this temperature. A smoother growth front at lower temperatures has also been reported by many authors (e.g. [74, 75, 77]). At these low temperatures, transient mobility has been suggested to provide an additional pathway for interlayer mass transport. However, Molecular Dynamic simulations with an Embedded Atom Method (EAM) potential did not show clear evidence of such an effect [78]. We do

stress that transient mobility confined to one hop can not be excluded and would fully account for the observed deviations between experiments and simulations. Two other effects are potential candidates to explain this behaviour. First, collective effects of clusters of adatoms on the upper terrace near a step edge. Teichert [55] already showed in calculations that such clusters of a few atoms near a kink position yields a reduced ES barrier on Ag(001) compared to the ES barrier for the kink site. With a vanishing ES barrier, this could imply a more favourable interlayer diffusion path compared to adatom diffusion as a result of a collective effect. This would lead to a slightly smoother growth front for temperatures just below the onset of adatom diffusion. A second effect is the kink rounding effect that has been used to explain the results on Ag(001) [45]. This results in a higher densities of kinks. The kink rounding effect was also recently used in a simulation to explain the observed growth behaviour at low temperatures [79]. It has also been reported that ES-barriers may be reduced on smaller adatom islands. Last but not least, small islands have been shown to be contracted [37, 39]. On top of contracted islands the activation energy for diffusion is lower and therefore the attempt frequency for descent increases [80]. This would inevitably lead to enhanced interlayer diffusion. All these effects, individually or combined, and with probably the latter option as the most prominent, give rise to smoother growth fronts. Our simulations do not take these effects in account, which limits their use to a temperature of 230 K and above.

We emphasize that admittedly the simulation of growth is a highly complex enterprise in which a multitude of thermally activated processes may be relevant. The activation barriers for these processes have to be determined quite accurately and where possible individually in order to describe growth reliably. The problem is further complicated by highly entangled processes and their complex interplay with respect to the evolving morphology. Especially dealing with processes with inherently very widely varying rates is definitely hazardous and requires intense attention. Being well aware of a variety of possible pitfalls we have examined internal consistency of our simulated results. With initial surprise and since then ever growing confidence we have performed a large number of comparisons between simulated results and experiments. We stress that with one set of parameters, combining calculated ones with the experimentally determined values for the ES-barriers associated with straight $\langle 110 \rangle$ steps and ($\langle 100 \rangle$ oriented) kink sites, we are able to uniquely describe and understand experimental data quantitatively. This holds for a relatively wide temperature range (230 - 290 K), in which relevant diffusion rates vary by several orders of magnitude, various deposition rates and, above all, a wide variation of film thicknesses. Especially the latter provides a very sensitive benchmark because of the cumulative nature of miss descriptions would lead to strong deviations of layer distributions, adatom sizes

and kink concentrations. The quality of our quantitative description provides a great deal of confidence in the global correctness of our simulations, at least for all relevant processes active in the investigated parameter space.

The evolution of the morphology of Cu(001) homoepitaxy was studied by several groups employing both various diffraction techniques as well as STM. These techniques all provide a different view on this morphology evolution. The specular He reflection (TEAS) data in this work at the highest temperature are quite similar to the ones recorded by Miguel et al. [48] for temperatures of 318 K and above. Ernst and coworkers published TEAS data in the range considered in this work that suggest a slightly smoother growth at 250 K [50]. This smoother growth is in line with the larger distance between islands at 0.5 ML measured by this group [61] and suggests a slight calibration issue on the temperature scale.

5.8 Conclusion

The interface roughening during the homoepitaxial growth of Cu(001) has been monitored with TEAS in the temperature range of 200 - 300 K. The normalized height of the specularly reflected He peak in the first maxima of the growth oscillation curves provides a data set that allows the determination of the Ehrlich Schwoebel barriers of the ⟨110⟩ and ⟨100⟩ step edges. This determination is performed by comparing the experimental interface roughening with growth simulations. Only for an ES barrier of 120 meV (or more) for the straight ⟨110⟩ step edge and -5 meV for the kink ⟨100⟩ step edge the simulations lead to agreement with the experimental results. The barrier for the straight step edge is a lower limit and reflects the fact that under the investigated conditions the interlayer mass transport occurs predominantly via the kink sites. The nine maxima of the specularly reflected He intensity recorded at 290 K are reproduced well by the simulation scheme if the experimental broadening is taken into account. With these parameters we can describe quantitatively the morphology of thin films up to at least 9 ML in a temperature range of 230 - 290 K and for a deposition rate varying by an order of magnitude (0.5 - 5 ML/min.). The simulated interface roughness shows a scaling exponent with respect to the coverage amounting to 0.5 at 250 K and 0.25 at 290 K, similar to previous experiments [74]. Concluding, the developed powerful kMC simulation reliably describes the morphology of the growing Cu(001) surface. We expect that it will do so also for other non-reconstructing metal (001) surfaces, such as Ag(001) and Ni(001).

CHAPTER 6

Shape anisotropy of adatom islands as a probe of dispersion forces in MBE

6.1 Introduction

Nanopatterning has evolved into a vast area of research in which both top - down, bottom - up and combined top down - bottom up approaches are used. Exploitation of the growth kinetics in self-organization is a quite widely used bottom - up approach for the creation of patterns of dots or lines with high symmetry [81]. A sufficient bond between substrate and deposited materials transfers the symmetry of the substrate in the pattern grown, like triangular or hexagonal, square and rectangular islands grown on fcc (111), (100) and (110) surfaces, respectively. Oblique incidence deposition can break this symmetry superimposed by the substrate, as for instance observed in magnetic properties [34, 82] . This result is exploited in many films of technological relevance and has led to the growth of layers with novel optical properties [3, 4].

Homoepitaxial growth provides a suitable research area to investigate the influence of grazing angle deposition on symmetry and morphology. In a seminal series of experiments, van Dijken et al. [6, 7] showed that the deposition of Cu on Cu(001) results in a breaking of the fourfold symmetry in sub-monolayer growth. For the explanation of their results they introduced the steering effect: Due to attractive forces

between an incoming atom and the substrate, the trajectory of the atom deviated from a straight line. Protrusions on the surface modulate the actual impact position with respect to the point of impact estimated from a long distance extrapolation. The result is a heterogeneous flux distribution and the growth of elongated adatom islands. Steering and the sequential diffusion dynamics at the very surface were evaluated theoretically by Montalenti and Voter for Ag(001) homoepitaxial growth [78]. In their accelerated first principle molecular dynamics approach, at normal incidence up to temperatures of 70 K, they used an interaction range limited to 5 Å. Amar et al. [10, 11, 32, 83] argued that the attractive interaction should be divided in a short range and long range part, respectively related to electron overlap interaction and dipole - dipole interaction. Via trajectory simulations near a step edge, they also concluded that at normal incidence only short range interactions are important [11] and that it leads to a significant upfunneling in the deposition process. Amar et al. argued that long range steering becomes important at off-normal deposition angles larger than 50° [10]. They also argued that the long range strength is much weaker than that of the LJ potential of Sanders and De Pristo used in the growth simulations of Seo et al. and Montalenti et al. [78, 84].

The observed anisotropy of adatom islands is the combined result of steering and the kinetics of growth. A quantitative analysis requires both trajectory evaluations based on the evolving morphology and the nucleation and growth of adatom islands, as done in the Voter approach [78]. From the point of computation time this method is not feasible for temperatures in the range of 250 K and the growth of 0.5 ML of material at realistic deposition rates. To model the growth in such a situation, a combination of efficient trajectory calculations and a lattice model for diffusion processes like in a kinetic Monte Carlo (kMC) scheme is required. Seo et al [84] reported such simulations with an LJ potential and a kMC simulation with a limited set of barriers. These simulations showed an anisotropy similar to that observed experimentally. However, their flux distribution on the island with the potential used is markedly enhanced compared to the results with the same potential described in ref. [7, 33]. Both (Seo [84] and Wormeester et al [7, 33]) use an evaluation for the determination of the condensation position at the end of each trajectory calculation. This evaluation of the condensation position is very critical as it determines whether an incoming atom near a step edges condensates in front of the step edge or on top of the adatom island. This different condensation position has much influence on the growth kinetics, leading to smooth or rough growth. A high quality calculation of the condensation of an incoming atom is possible with a full dynamic evaluation of the dynamics of the surface lattice at short range distance. Amar uses this technique in simulating the growth experiments of Ernst at 160 K and 200 K [79].

In this chapter an efficient trajectory simulation will be compared with full Molecular Dynamics simulations. This efficient trajectory calculation routine is later combined with a kMC scheme that enables to evaluate the influence of the long range attraction on the island elongation, which turns out to be significant. These simulation results will be compared to the experimental determination of the change in island elongation with coverage. The actual strength of the long range dipolar interaction will be determined from this comparison.

6.2 Island anisotropy determined with electron diffraction

Homoepitaxial growth experiments on a Cu(001) surface held at 250 K were conducted in an ultrahigh vacuum (base pressure $< 10^{-10}$ mbar). Cu was deposited at a rate of 0.5 ML/min at a grazing angle of incidence (80° from the normal) along the [110] azimuth. The morphology was analyzed with high resolution low energy electron diffraction (HRLEED) after cooling the sample to 100 K.

Figure 6.1 shows a measured diffraction image reported by van Dijken et al. [6, 7] after deposition 0.5 ML at grazing incidence angle of 80° and $T = 250$ K with a deposition rate of 0.25 ML/min. The symmetry of the diffraction pattern is reduced to two plane mirrors. The line scans parallel and perpendicular to the deposition direction differ only by the intensity of the first maximum, $I_{[110]}$ and $I_{[\bar{1}10]}$ respectively, whose position represents the average distance L between islands. This observation indicates that in the [110] and the $[\bar{1}10]$ direction the average distances L and the stochastic variation of the distance are similar. As a matter of fact this comes as no surprise because of the isotropic diffusion on the Cu(001) surface. Therefore, the intensity anisotropy of about 12.5% at 0.5 ML coverage is related to an average island shape anisotropy and is fully decoupled from distance distributions.

The average island shape anisotropy can be determined from the intensity ratio. Assume a surface covered with rectangular islands with average sizes $W_{[\bar{1}10]}$ and $W_{[110]}$ along the two perpendicular directions. The intensity of the diffraction features as a result of their periodic ordering is modulated by the shape function $sinc\,(\pi W/L)$. The intensity ratio $I_{[110]}/I_{[\bar{1}10]}$ can then be approximated by (see appendix)

$$\frac{I_{[\bar{1}10]}}{I_{[110]}} = 1 + 2\left(1 + \frac{W_{[\bar{1}10]}}{W_{[110]}}\right)\left(1 - \frac{\pi\sqrt{\theta}}{\tan\left(\pi\sqrt{\theta}\right)}\right)$$

This shows that the observed intensity ratio is strongly influenced by the coverage (θ). At $\theta = 0.5$ ML the actual shape anisotropy is strongly enhanced by the diffraction method. From the measured intensity ratio of 12.5% at a coverage of 0.5 ML an actual

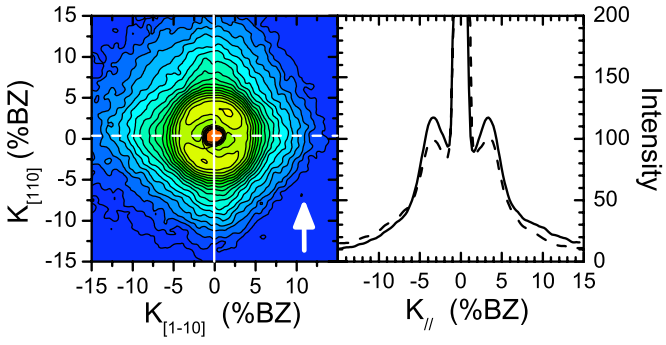

Figure 6.1: High resolution LEED images after just over 0.5 ML grown at grazing incidence deposition of $\alpha = 80^\circ$ at $T = 250$ K with a rate R = 0.25 ML/min (left). The arrow indicates the deposition direction. Line scans parallel (solid) and perpendicular (dashed) to the deposition plane (right).

shape anisotropy of only 1.9% is determined with this analysis. Such small values are hard to access by STM experiments and require diffraction approaches.

6.3 Trajectory simulation

A full Molecular Dynamic simulation of trajectories of incoming atoms is too time consuming to describe growth at realistic substrate temperatures and deposition fluxes. Therefore, a realistic condensation rule (CR) that efficiently determines the position of accommodation on a frozen surface is urgently required. The condensation process is quite subtle and requires specific attention. The landing procedure is illustrated in fig 6.2 for an atom arriving near a step atom. A natural choice is to evaluate the angle of the trajectory direction ($atan(v_x/v_z)$) with respect to the angle of the hart line between the incoming atom and the nearest (substrate) atom ($atan(x/z)$), when they make contact, i.e., their separation equals the atomic diameter $a = 2.55$ Å, see fig. 6.2. The incoming atom shows upfunneling (condensation in capture zone 4 in fig. 6.2) if the angle of the trajectory direction ($atan(v_x/v_z)$) is larger than the angle of the hart line ($atan(x/z)$). Otherwise, the atom shows downfunneling (condensation in capture zone 3 in front of the step in fig. 6.2). The validity of this rule was checked by comparing flux distributions near an up and down step calculated a) with Molecular Dynamic (MD) simulations [85, 86] and b) with the trajectory calculation using

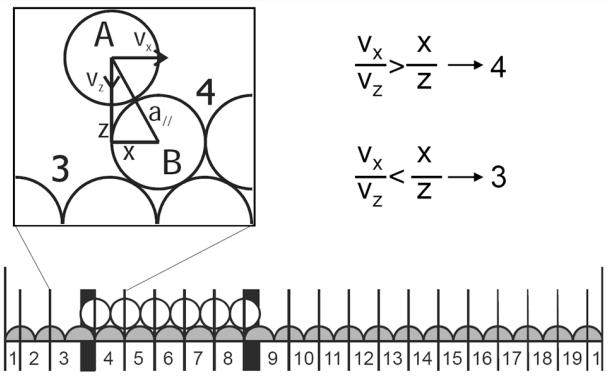

Figure 6.2: (top) Illustration of the condensation rule for the incoming atom A as it gets into contact with a step edge atom B. (below) The substrate surface and an adatom island used in the trajectory calculations. Indicated are the condensation boxes 1 - 19 (see text). The shaded areas refer to non-residence sites.

this condensation rule. The MD method has been successful in reproducing many of the characteristics of bulk and surface systems especially near steps and kinks [87].

The MD cell used consists of a substrate of 8 Cu(001)layers of 20×6 atoms and an adatom island of 6×6 atoms. Periodic boundary conditions were applied parallel to the surface. This implies that the island resembles an infinitely long stripe of 6 atoms wide with an up and down step in the [110] direction parallel to the deposition plane. There is no periodic boundary in the vertical direction. Artifacts due to finite size effects are suppressed by partitioning the substrate in the vertical direction [85, 86]. The lowest 2 layers are kept at fixed position to avoid global motion. The next three layers are held at constant temperature. These so-called sandbag layers absorb the excess energy introduced by the impinging atoms. The top 3 layers and the adatom island follow micro-canonical dynamics. The incoming atoms with an initial velocity of 551 m/s equivalent to a kinetic energy of 0.1 eV and a polar deposition angle ϑ are launched 5 Å above the average vertical position of the adatom island. Note that the cut-off distance of the EAM potential for Cu is 4.8 Å and beyond this range there are no attractive forces. One MD simulation of a deposition event results in the condensation of the incoming atom at one of the fourfold hollow sites on the surface. The condensation sites are labeled by 1-19 in fig. 6.2, depending on their position perpendicular to the stripe. As a consequence of the fcc-structure a "no residence" region is located near the step, occupied by half an atom from the adatom layer. This implies that without any interaction (no attraction and rigid lattice) the condensation sites 3 and 9 will receive 50% more flux at normal incidence deposition. In the x-direction of the cell, i.e. in the plane of incidence, 400 equidistant starting points

were chosen, while perpendicular to this (y-direction), another 11 starting points distributed over half an atom width were chosen. The latter allows an investigation of the influence of the atomic corrugation: only a minor effect was noted.

Figure 6.3 a) shows the results of these simulations for $\vartheta = 80°$ at a temperature of 250 K. The heterogeneity of the flux as a result of the change in trajectory is in the EAM MD calculation remains limited to the condensation point 4 at the up step and 9 - 12 for the down step. The latter region is also the range found for a geometric shadow. The reduced flux behind the island at grazing incidence deposition results in an additional flux on top of the island of almost 4 additional atoms in box 4, just below the geometric limit of the transferred flux, $\Phi = \frac{1}{2}\sqrt{2}tan(\vartheta)\Phi_0$. The amount of flux in front of the island, box 3, is about 1.5, just corresponding to its physical size, and was found to be virtually independent of the incidence angle. The steering effect modelled by the EAM potential redirects the complete flux reduction of the shadow region towards enhanced flux on the **top** of the adatom island.

Long range interaction was incorporated in these MD calculations by adding outside the short range interaction region a r^{-6} tail to the pair-pair potential with the strength of the LJ potential of Sanders and DePristo [9] ϕ_{SDP}. Figure 6.3 c) shows the influence of the long range attractive interaction. The amount of material lacking behind the adatom island and in access on top is similar, but the distribution both on top and in the shadow region has markedly changed. Transient mobility effects were not observed in these MD simulations.

The condensation rule was first evaluated for short range effects (fig. 6.3 b). A cut-off function is used that limits the interaction range of the ϕ_{SDP} potential. For a pair-pair distance r larger than $r_c = 7.0$ Å, the force is set to zero, while below this distance it is multiplied by the function $\left(r^2 - r_c^2\right)^2 / [\left(r^2 - r_c^2\right)^2 + Q^2]$ with $Q = 0.65$ Å^2, see chapter 4. The interaction as a result of this ϕ_{SR} potential is similar to that of the EAM potential. The flux redistribution calculated with this potential is similar to the full MD simulation, fig. 6.3 b). This indicates that short range interaction effects are well represented by a rigid lattice and the condensation rule. Figure 6.3 d) shows the redistribution including long range effects, confirming that also in this case the flux heterogeneity of the full MD simulations can be obtained for a rigid lattice with sufficient accuracy by applying the above described condensation rule.

The LJ potential developed by Sanders and DePristo, ϕ_{SDP}, was parameterized on the nearest neighbour distance and the condensation energy. These values are determined by the electron overlap interaction as also taken into account by the EAM potential. For long range interaction, this pair-pair potential shows the r^{-6} behaviour of the dipole dipole interaction. However, as argued by Amar [10], the strength of this interaction in the dipolar range is overestimated. Based on the optical properties of

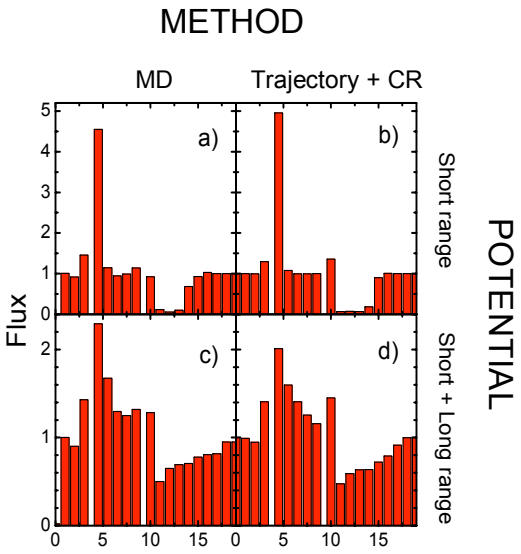

Figure 6.3: Normalized heterogeneous flux on a substrate with an adatom island obtained for atoms incident from left to right at an initial polar angle of incidence of 80° evaluated with: a) EAM, b) truncated potential ϕ_{SR}, c) EAM potential with extended interaction d) ϕ_{SDP} potential (see text). (CR = Condensation Rule)

the materials a 5.7 times smaller dipolar interaction has been evaluated. We accounted for the different strength of the short and long range interaction interaction through a modified LJ pair-pair potential:

$$\phi_M(r) = \frac{c_{10}}{r^{10}} - \frac{c_8}{r^8} - \frac{c_6}{r^6}$$

with $c_{10} = 21.9$ keV/Å^{10}, $c_8 = 3.85$ keV/Å^8 and $c_6 = 47.1$ eV/Å^6. This potential gives the same condensation energy and nearest neighbour distance as ϕ_{SDP}, while the long range behaviour is attenuated by a factor of 5.7. We found that the induced small variation in the shape of the potential in the short range area has negligible influence on the flux distribution. A change in the strength of the long range tail has considerable influence on the flux distribution on top of the island and behind the island as was illustrated already in fig. 6.3.

6.4 Island anisotropy determined from growth simulations

The trajectory calculations have been incorporated in a kinetic Monte Carlo (kMC) scheme that describes the diffusion processes and gives rise to realistic growth

fronts (morphologies as discussed in chapter 5). The intralayer mass transport was modeled using the energy barriers given by Biham et al [28], which provide the experimentally observed density of adatom islands over a wide range of temperatures and fluxes in the initial phase of submonolayer growth. The interlayer mass transport is governed by both step and kink Ehrlich-Schwoebel (ES) barriers, whose values were determined from a comparison of experiments and simulations for normal incidence growth in a temperature range of 230 - 290 K, see chapter 5. The evaluated ES barriers of 125 meV for the step and -3 meV for the kink show that interlayer mass transport occurs mainly via the kink sites. The simulation has been performed on a grid of 512 $\times$ 512 atoms^2 with periodic boundary conditions. A typical simulation result after 0.44 ML deposition at 250 K using the ϕ_M potential showing anisotropy is given in fig. 6.4 a).

The shape anisotropy of the islands was determined from the autocorrelation image obtained from averaging over 64 simulations. The ratio of the slopes of the autocorrelation image at the origin in the [110] and [$\bar{1}$10] direction are a direct measure of the average aspect ratio of the island shape, $W_{[\bar{1}10]}/W_{[110]}$. Figure 6.4 b) shows the gradual increase of the aspect ratio with coverage. The obtained anisotropy using the ϕ_M potential is quite similar to that found experimentally at 0.5 ML, 2%.

The curve is affected by the variation in aspect ratio of islands if the curve is averaged over less than 16 simulations. The variation of individual simulations are of about 1.5% absolute at low coverage, increasing to 2% absolute around a coverage of 0.5 ML. It reflects the large variation in aspect ratios of the islands present on the (512 $\times$ 512) atoms^2 surface at the considered temperature.

Also shown are average aspect ratios obtained from simulations using a strong dipolar interaction (ϕ_{SDP}) and without the dipolar interaction (ϕ_{SR}) (see chapter 4). The latter was found to give a much larger anisotropy and an almost linear increase with coverage. A large dipolar interaction leads to about half the aspect ratio at 0.5 ML coverage compared to the modified interaction potential.

The simulation results were compared with experiments by calculating the diffraction pattern of the simulated morphologies at an out-of-phase condition. A simulated diffraction pattern at 0.5 ML coverage for the modified interaction potential is shown in fig. 6.5 a). The change in anisotropy with coverage was evaluated for the three interaction potentials. The results of these simulations are shown in fig. 6.5 b) as well as experimental results determined from high resolution low energy electron diffraction at various submonolayer coverages. As expected from the difference in aspect ratios, a very different evolution of the diffraction intensity anisotropy is observed for the three interaction potentials. Surprisingly, the short range potential clearly overestimates the experimentally found anisotropy. The ϕ_{SDP} potential on the other

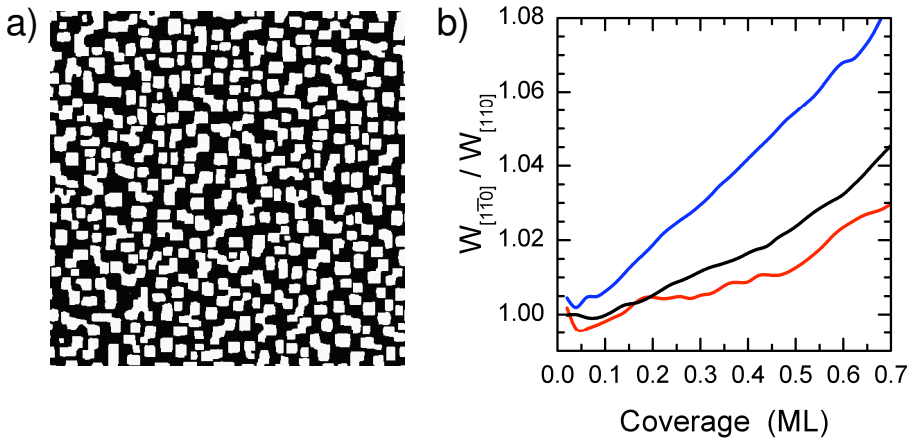

Figure 6.4: a) Morphology after depositing 0.44 ML of material at grazing incidence (80°) at a temperature of 250 K and deposition rate of 0.6 ML/min. b) Change in island aspect ratio as a function of coverage evaluated with the strong dipolar interaction ϕ_{SDP} (red line), the modified potential ϕ_M (black line) and the short range potential ϕ_{SR} (blue line). The results are averaged over 64 kMC simulations at a field of 512 × 512 lattice sites.

hand underestimates the effect around 0.5 ML coverage. The modified potential describes quite well the experimental results. Both in the present experiments as well in previous experiments [6, 7] an intensity ratio around 15% was measured around 0.5 ML coverage. This value corresponds to that obtained with the modified potential. The coverage range is limited to about 0.6 ML. Above this coverage the azimuthal ordening of the islands changes to a checkerboard-like pattern that complicates the determination of the anisotropy. Also strong progressing coalescence prevents the use of higher coverages. The difference in the anisotropy for the three interaction potentials can be explained from fig. 6.3 b) and d). The dipolar interaction does not give rise to an increase of the amount of material deposited on the island, but it has great influence on the distribution over the island. The short range interaction only is already effective in the presence of a two atom wide island. The amount of material on top of the island depends strongly on the island width for small island size as a result of dipolar interaction. This results in a much smaller change in anisotropy at lower coverage, and even an almost isotropic growth of islands for the ϕ_{SDP} potential in this range. The increase of the shape anisotropy with coverage is quite linear.

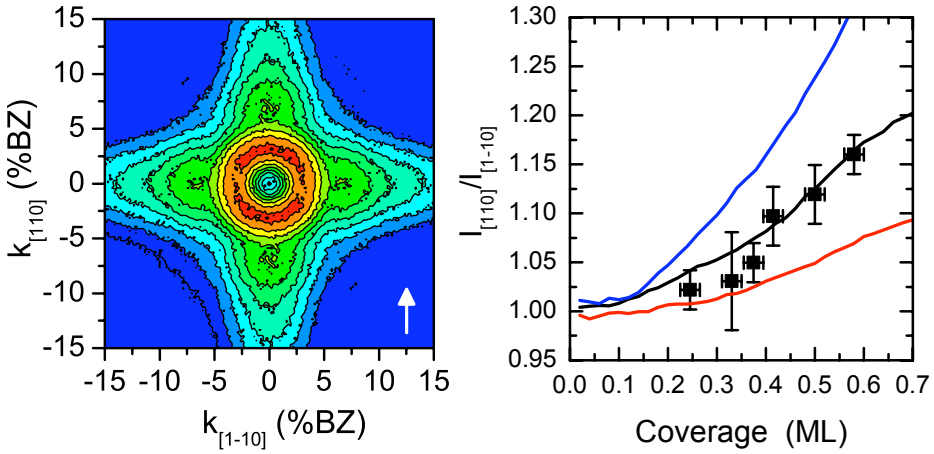

Figure 6.5: (left) Contour plot of the calculated diffraction pattern after deposition of 60 %ML averaged over 128 simulations at grazing incidence of 80° at a temperature of 250 K at deposition rate of 0.6 ML/min. The simulation has been carried out with the ϕ_M potential. The arrow indicates the deposition direction (right). Intensity anisotropy in the diffraction pattern as a function of coverage as measured (■) and calculated for the standard potential ϕ_{SDP} (red line), the modified potential phi_M (black line) and for short range interaction ϕ_{SR} (blue line).

6.5 Conclusion

In conclusion, we have shown that for grazing incidence deposition both the long and short range attractive interaction between the incoming particle and the actual growing surface are of qualitative and quantitative importance for the consequence of the steering effect for the evolving film morphology. A condensation rule that determines the accommodation position on the surface of an incoming atom on the basis of velocity direction of the incoming particle at a very short distance to the surface enables a combined simulation of the surface dynamics with an efficient trajectory calculations. Trajectory calculations and a kMC algorithm for diffusion processes on the Cu(001) surfaces result in the observation of rectangular islands with their long axis perpendicular to the deposition plane, similar to experimental results obtained for submonolayer coverage. The pronounced sensitivity of the obtained island shape anisotropy opens a powerful way to gain insight in the shape of the attractive potential. A modified Lennard-Jones potential, which also accounts properly for the optical properties of Cu, yields results that lead to a convincing quantitative agreement with experimental data in the entire coverage regime. Diffraction measurements are very sensitive to the average island shape anisotropy.

Appendix

Determination of island aspect ratio in diffraction

Both kMC simulations and high resolution electron diffraction experiments are used to determine the island shape anisotropy. In the diffraction experiments performed in the submonolayer coverage regime an intensity ring is observed at the average distance between islands. Anisotropy is observed as a modulation of the intensity of this ring. This modulation can be understood as resulting from the Fraunhofer diffraction pattern due to anisotropic adatom island shapes and can be analyzed analytically. A two level pattern in real space with a periodicity of an island in x and y direction of L_x and L_y respectively is considered. The island width along the x- and the y-direction is given by W_x and W_y. The diffraction pattern of this shape is proportional to the square of the Fourier transform of this pattern, i.e.

$$I = \left(\frac{W_x W_y}{L_x L_y}\right)^2 sinc^2\left(\frac{m\pi W_x}{L_x}\right) sinc^2\left(\frac{n\pi W_y}{L_y}\right)$$

The numbers m and n denote the diffraction order given by the periodicity L_x and L_y. For $n^2 + m^2 = 1$ the intensity of the ring reflecting the periodicity present is obtained. The aspect ratio is obtained from the two orthogonal directions x and y, i.e. $m = 1$ n=0 and $m = 0$ $n = 1$, respectively. If the periodicity is the same, this gives for the aspect ratio:

$$\frac{I_x}{I_y} = \left(\frac{W_y}{W_x}\right)^2 \frac{\sin^2\left(\frac{\pi W_x}{L_x}\right)}{\sin^2\left(\frac{\pi W_y}{L_y}\right)}$$

This expression shows that the measured intensity ratio from diffraction not only depends on the anisotropic shape of the islands, W_y/W_x, but also on the periodicity L, i.e. on the coverage.

This expression can be approximated for small anisotropy with $\Delta W = W_y - W_x$ and $W = (W_y + W_x)/2$ by

$$\begin{aligned}\tfrac{I_x}{I_y} &= 1 + 2\tfrac{\Delta W}{W}\left(1 - \tfrac{\pi W/L}{\tan(\pi W/L)}\right) \\ &= 1 + 2\tfrac{\Delta W}{W}\left(1 - \tfrac{\pi\sqrt{\theta}}{\tan\left(\pi\sqrt{\theta}\right)}\right)\end{aligned}$$

This expression shows that the diffraction anisotropy increases with coverage. At 1/4 ML coverage the diffraction anisotropy is related to $1 + 2\frac{\Delta W}{W}$. Especially for higher coverages a large deviation from this number occurs. It is noted in addition that the analysis also fails, irrespective of the value of ΔW, upon coalescence of the adatom structures.

Determination of island anisotropy from topography images through autocorrelation

The characteristic length scales in a (set of) topography image(s) can be quantified with either a Fourier transform or a height-height correlation method. The height-height or autocorrelation AC of an image f is defined as:

$$AC\left(\bar{x}\right) = \int f\left(\bar{r}\right) f\left(\bar{r}+\bar{x}\right) d\bar{r}$$

in this $\bar{r}$ denotes the lateral position in the image and $\bar{x}$ the applied lateral shift between the two images. For an image with an average periodicity L of a shape of size W, the autocorrelation will typically show a peak at a (multiple) shift distance L. At small shift distance, the value of AC decreases linearly with the shift distance. For a 1D profile, the rate of this decrease only depends on the periodicity L, but not on the size W. The latter no longer holds for the autocorrelation of a 2D topography. This is illustrated by considering a periodic island structure with size W_x and W_y and periodicity L_x and L_y. For an island of unit height, the plane of mean height $\bar{h}$ is located at height $W_xW_y/L_xL_y = \theta$, with θ the island coverage. The autocorrelation at $\bar{x} = 0$ is equal to the square of the RMS if the height used in the evaluation is taken relative to the mean height $\bar{h}$.

$$AC\left(0\right) = \theta\left(1-\bar{h}\right)^2 + \left(1-\theta\right)\bar{h}^2 = \theta - \theta^2$$

The slope rc near $\bar{h} = 0$ can be evaluated by shifting the island by 1 position in the x and y direction. For a shift in the x direction this gives:

$$\begin{aligned}
&AC_x\left(1\right) = \tfrac{\left(W_x-1\right)W_y}{L_xL_y}\left(1-\bar{h}\right)^2 + \tfrac{\left(L_x-W_x-1\right)W_y}{L_xL_y}\left(\bar{h}\right)^2 + \tfrac{\left(L_y-W_y\right)L_x}{L_xL_y}\left(\bar{h}\right)^2 + 2\tfrac{W_y}{L_xL_y}\bar{h}\left(1-\bar{h}\right)\\
&= AC\left(0\right) - \tfrac{W_y}{L_xL_y}\left(1-\bar{h}\right)^2 - \tfrac{W_y}{L_xL_y}\left(\bar{h}\right)^2 + 2\tfrac{W_y}{L_xL_y}\bar{h}\left(1-\bar{h}\right)\\
&= AC\left(0\right) - \tfrac{W_y}{L_xL_y}\left(1-2\bar{h}\right)^2\\
&= AC\left(0\right) - \tfrac{W_y}{L_xL_y}\left(1-4\theta+4\theta^2\right)\\
&= AC\left(0\right) - \tfrac{\theta}{W_x}\left(1-4\theta+4\theta^2\right)\\
&rc_x = AC_x\left(1\right) - AC\left(0\right) = -\tfrac{\theta}{W_x}\left(1-4\theta+4\theta^2\right)
\end{aligned}$$

The slope rc thus depends on the coverage and the width of the island in the orthogonal direction. This gives a simple determination of the island anisotropy from the ratio of the slopes rc of the autocorrelation function:

$$\frac{rc_x}{rc_y} = \frac{W_y}{W_x} = 1 + \frac{\Delta W}{W}$$

This also provides a straightforward determination of island anisotropy from diffraction data.

CHAPTER 7

Oblique incidence deposition: Super roughness and ripple formation

7.1 Introduction

Oblique incidence deposition was found to lead to the development of anisotropic structures like columnar growth. The orientation of these columns has been described phenomenologically by the so-called tangent rule [1]. Material properties like magnetic [2] and optical [3, 4] behaviour can be tuned with oblique growth. The understanding of this growth behaviour is still quite rudimentary, which holds especially for the initial stage of column formation. The oblique deposition of a Co-Ni alloy on a polyethylene terephthalate substrate showed columnar growth for films with a thickness larger than 30 nm. Films with a thickness below 30 nm showed a very different magnetic behaviour compared to the thicker films. In the thick films, a hard magnetic axis was formed parallel to the column orientation, while for thinner films the magnetic hard axis was found to be parallel to the interface and perpendicular to the plane of the deposition beam [34]. The orientation of the uniaxial magnetic axis for these thin films is similar to that found for thin Co films deposited at grazing incidence on Cu(001) [6, 7, 82, 88]. The uniaxial magnetic axis is the result of an anisotropic morphology. The growth of anisotropic structures was explained with an effect coined as steering [6]: Protrusions on the surface act as attractors for incoming material. The trajectories of incoming atoms are changed under the influence of attractive forces

between these atoms and the actual substrate morphology.

Homoepitaxial growth provides an excellent system for the study of the steering effect. Complications as a result of intermixing and lattice mismatch are absent in this case. The influence of steering on sub-monolayer growth was described in chapter 6. For thicker layers, high resolution low energy electron diffraction showed the formation of elongated structures that are well ordered along the plane of incidence of the deposition beam [6, 7]. The facet angles of the mounds on the surface as a function of deposition angle were recorded for 40 ML thick films. These results showed that the facets of the illuminated side, the shadow side and the two side walls develop in a very different manner. The growth of these structures was recently described by Shim and Amar [89]. They reported the development of ripple structures, a change in orientation of these ripples for thick films deposited at grazing incidence and a very rough growth front. These calculations were done with a barrier for interlayer mass transport that is much higher than actually present on the Cu(001) surface, cf. chapter 5. This leads to a quite rough growth front from the very start, while experimentally more layer-by-layer like growth is observed at temperatures of 250 K and higher. For the study of the initial growth of Cu (001) a dedicated growth simulation program for Cu(001) was developed that incorporates the calculation of trajectories of incoming atoms. With this program and adequate barriers for the interlayer mass transport, the multilayer growth at oblique incidence was studied. Already existing high resolution low energy electron diffraction measurements [5–8] were complemented with more extensive measurements of especially the facets formed. The experiments and the simulations show a high degree of correspondence, providing confidence in the use of simulations to investigate the processes involved in the development of the elongated structures. Also the strong roughening of the growth front during oblique incidence deposition can be studied. This leads to the observation of Super Poisson roughening, i.e. the interface roughening is stronger than that resulting from a simple hit and stick deposition process with a homogeneous flux of atoms.

7.2 Experimental and simulation details

Homoepitaxial growth experiments on a Cu(001) surface were performed in an ultrahigh vacuum system (base pressure $< 10^{-10}$ mbar). Cu was deposited at a rate of 0.5 ML/min, under grazing incidence conditions (polar angle typically 80°) along the [110] azimuth. After deposition, the morphology was analyzed with high resolution low energy electron diffraction (HR-LEED). During this analysis the sample was kept at 100 K to avoid posterior coarsening effects.

Oblique incidence deposition was simulated with a kinetic Monte Carlo (kMC)

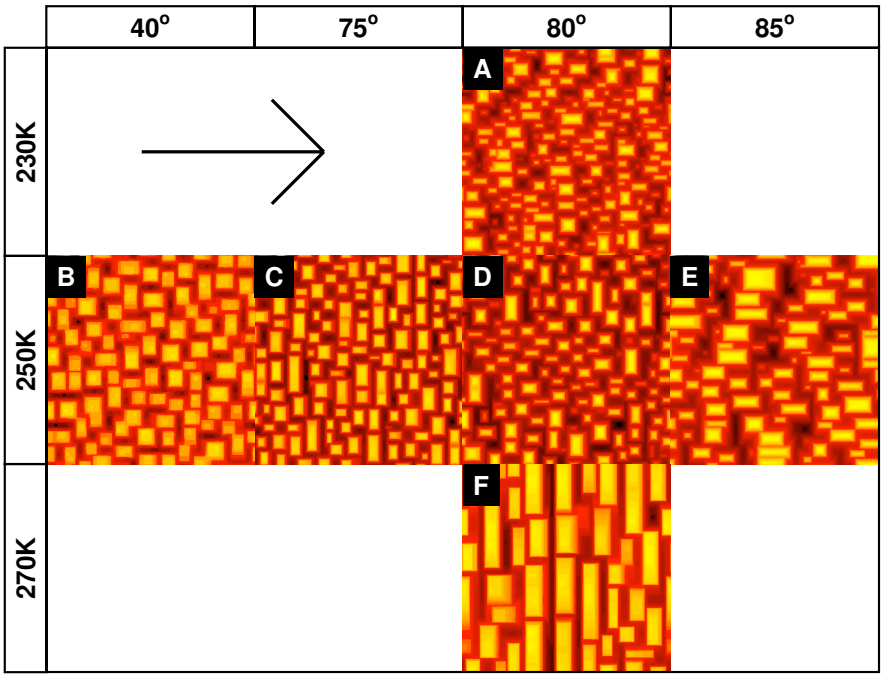

Figure 7.1: Simulated topographic images of the surface morphology after growing 40 ML at a rate of $R = 1$ ML/min at different deposition angles (horizontal) and temperatures (vertical). The temperatures are 230 K (A), 250 K (B-E) and 270 K (F). The polar deposition angles are 40° (B), 75° (C), 80° (A, D, F) and 85° (E). Each window is 120 nm (512 atoms) wide. The arrow denotes the deposition direction.

scheme on a lattice consisting of 512 × 512 atoms. Activation barriers for intra layer processes as determined by Biham et al. [28] were used. Two interlayer diffusion processes were incorporated simulating transport via ⟨110⟩ and ⟨100⟩ oriented step edge segments. Ehrlich Schwoebel (ES) barrier for these processes of > 120 and -5 meV were used, respectively, as derived in chapter 5. The impact position of an atom was obtained from a trajectory calculation. Every incoming atom experiences a potential that mimics both the short range electron overlap effects, as well as the long range dipole-dipole interaction. The parameters have been taken from the results obtained in chapter 6. The potential depends on the actual morphology. Both the experiments and the simulations show an extensive formation of {111} facets. The activation energy for diffusion on a {111} surface is very low compared to a {100} surface [90]. The movement of an adatom on a {111} facet is therefore treated as an instantaneous move down the facet, where the atom is finally incorporated in the

advancing step edge. This treatment corresponds to assuming step propagation on the relatively small facets.

7.3 Oblique incidence homoepitaxial growth

The influence of the deposition angle on the surface morphology was studied by simulating the homoepitaxial growth of 40 ML. The polar angle of incidence was varied from 40° to extremely grazing deposition at an angle of 85°. At small polar angles, the effect of steering is minimal, while at grazing incidence the steering effect is responsible for the experimentally reported formation of a ripple structure [7, 8]. The experimental window for ripple formation after 40 ML deposition is narrow. They are present at 250 K, but absent at 200 and 300 K. The influence of temperature was studied by simulating the growth at 230, 250 and 270 K for the grazing angle of incidence of 80°. All simulations were performed with a deposition rate of 1 ML/min. A (much) lower rate increases the computational time for simulation beyond present capabilities, while a (much) higher rate is not accessible with the current experimental set-up. Figure 7.1 shows a few simulated morphologies after deposition of 40 ML. At a polar angle of 40° and 250 K, the mounds formed are vaguely ordered in a checkerboard-like pattern, similar to normal incidence growth [51]. Around 80° a dramatic change in mound formation is observed. Below this angle rectangular mounds perpendicular to the deposition plane are observed while for very grazing incidence, 85°, the mound orientation has rotated parallel to the plane of incidence. Similar elongated mounds parallel to the deposition plane were also observed for 80° at 230 K and agree with recent reports [89]. In contrast, at 270 K very well defined ripples have developed perpendicular to the plane of incidence. These results show that only small changes in temperature and deposition angle leads to a large variety of simulated morphologies. The preparation of well defined ripple structures requires an elevated temperature of 270 K. At lower temperatures a rotation of the elongated mounds occurs before they can merge in a ripple like structure. The evolution of the simulated morphology and its comparison with experimental data will be done using two characteristic properties: the average slopes of the four sides of the mounds and the overall roughness.

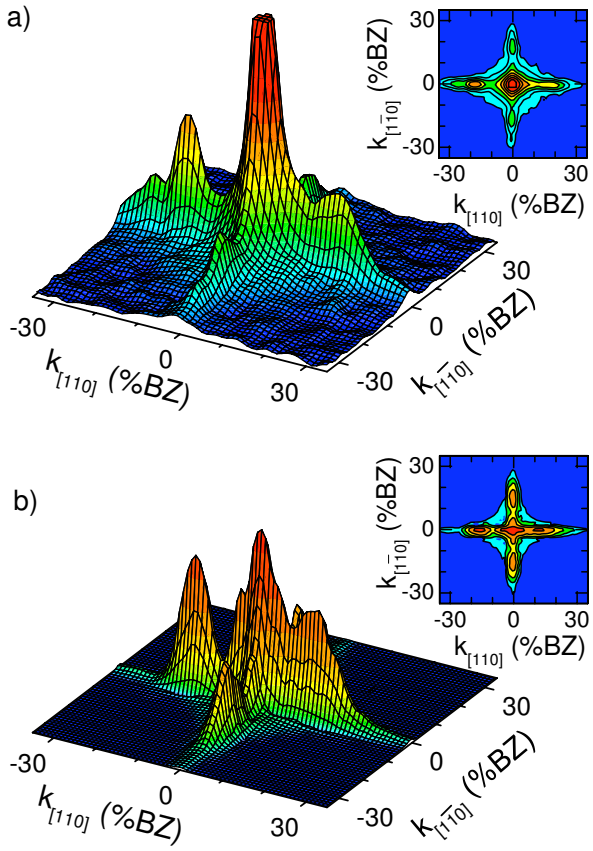

Figure 7.2: Diffraction profiles after depositing 36.5 ML at 80° at $T = 250$ K. (a) The experimental diffraction image and (b) the corresponding simulation result. The phase is $S_z = 3.9$ (176 eV). The plane of incidence for the copper atom beam is along the [110] direction.

7.4 Slopes of the mound facets after depositing ≈ 40 ML at grazing incidence

The experimentally observed diffraction pattern around 40 ML deposited at grazing incidence (80°) is dominated by features related to various slopes of the facets on the different sides of the mounds present on the surface. The diffraction image is mirror symmetric with respect to the plane of incidence of the atomic copper beam. Figure 7.2 a) shows a typical experimental diffraction pattern recorded after deposition of 36.5 ML. Figure 7.2 b) exhibits a simulated diffraction pattern. The simulated diffraction images have been calculated in the kinematic approximation for diffraction

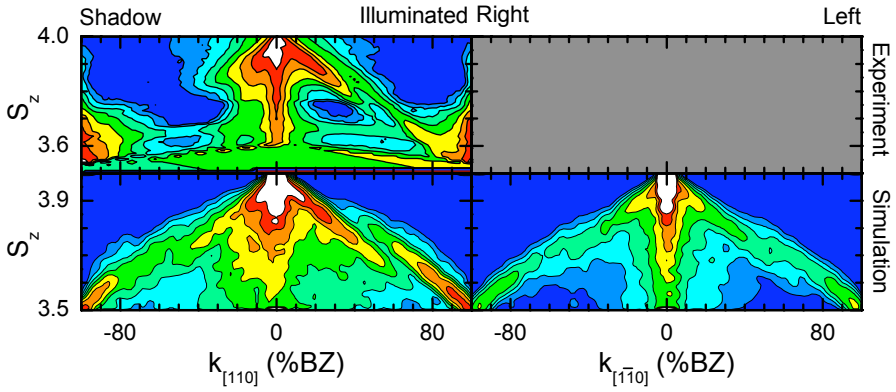

Figure 7.3: Intensity in the $k_{[110]} - S_z$ diffraction plane and in the $k_{[1\bar{1}0]} - S_z$ plane. The intensity rods correspond to the average slope of the mound facets present at the illuminated and shadow side (left images) and the left and right side (right images). The top panels exhibit experimental results, while bottom ones show simulation results. The surface is has emerged after depositing 29 ML at 80° polar angle of incidence at $T = 250$ K.

conditions similar to experimental conditions. The average slopes present in simulated growth fronts as depicted e.g. in fig. 7.1 also become apparent from diffraction images.

The experimental and simulated diffraction images in fig. 7.2 are quite similar. Both images show a two-fold symmetric profile with the plane of incidence as mirror plane. Moreover, the position of the diffraction features is quite similar. The relative intensity of these features differ, which is possibly the result of the neglect of dynamic effects in the calculation of the diffraction patterns, a non ideal quench and flux variations in the experiment across the incident beam spot.

The facet slopes of the different sides of the mounds can be determined from the diffraction image through variation of the electron energy. The close packed directions are the directions of high symmetry and an intensity scan of the perpendicular phase versus $k_{[110]}$ and, respectively $k_{[1\bar{1}0]}$ reveals all slopes present on the surface. Lines of high intensity are oriented perpendicular to facets at, respectively, the illuminated/shadow and the left/right sides of the mounds. We will refer to them as facet truncation rods. Figure 7.3 shows experimental and simulated results obtained after depositing 29 ML at $T = 250$ K at a polar angle of incidence of 80°. Both the perpendicular and parallel phases are represented by their normalized values: $k_{[110]}$ and $k_{[1\bar{1}0]}$ are expressed in % Brillouin zone (%BZ). 100 %BZ corresponds to $2\pi/a$, where $a = 2.55$ Å denotes the in-plane lattice constant. The perpendicular momentum $k_{[001]}$ is represented by the phase S_z relating to $k_{[001]}$ by $k_{[001]} = \sqrt{2}S_z\,(2\pi/a)$.

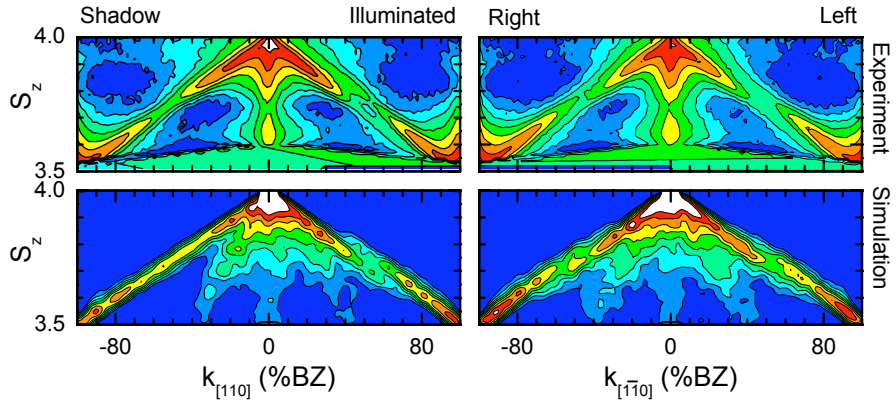

Figure 7.4: The diffracted intensity in the $k_{[110]}$ - S_z (left) and $k_{[1\bar{1}0]}$ - S_z plane (right). The intensity rods represent the average slopes of the mound facets present at the illuminated and shadow side (left images) and the left and right side (right images). The top panels show experimental results, while the bottom ones exhibit simulation results. The surface morphology is obtained after deposition of 35.4 ML at a polar angle of incidence op 80° at $T = 230$ K.

At the illuminated side two quite well defined facet truncation rods can be discerned at an angle of about 50° with the vertical axis. The appearance of these two parallel rods shows that the illuminated slope is a {111}-vicinal oriented facet, with terraces of a well defined width. The overall slope of the illuminated side is 50°. Note that this angle is just below the 54.7° of a {111} facet with respect to the {100} base plane. The terrace width is smaller than the length of the facet. This terrace width can be deduced from the separation between the parallel facet truncation rods. The simulated and the experimentally observed separations ($\Delta k_{[110]} = 13$ %BZ) at the illuminated side are similar within 0.5°, the accuracy of the results. At the shadow side broad intensity rods can be identified close to 54.7° and 25.2°. This shows that no clear slope has evolved at the shadow side. Instead, the slope contains a combination of {111} and {113} micro facets.

Deposition of 35.4 ML at $T = 230$ K (at the same grazing incidence angle of 80°) shows a different development of slopes, as revealed by fig. 7.4. On the shadow side of the mounds a much clearer facet feature evolves. Mounds with well defined {111} facets have developed. Both the parallel and illuminated sides also show a similar {111} oriented terrace structure. The average width of these terraces as deduced from the separation between the two parallel facet truncation rods is larger than the one observed at 250 K. The separation has reduced to $\Delta k_{[110]} = 10$ %BZ, corresponding to an average slope of 52°. It is remarkable that the shadow side has the steepest slope both in experiment and simulation. The intensity of the features

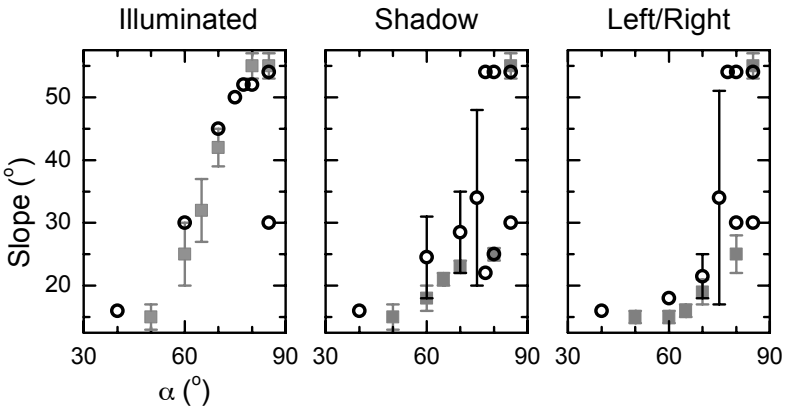

Figure 7.5: Evolved slopes after deposition of 40 ML as function of polar deposition angles. The gray squares refer to the experimental data points from van Dijken (T = 250 K, R = 0.25 ML/min) [6]. The black circles result from the present simulations (T = 250 K, R = 1 ML/min).

differ between the experimentally recorded spectra and the simulated ones, but their position is similar. This close agreement between simulation and experiment indicates that overhangs do not play a major role.

The developed slopes of the mounds can now be derived for different deposition angles. In this way, the dependence of the developed slope at the sides of the mounds on the deposition angle can be found. Figure 7.5 shows the results for a 40 ML thick film grown at T = 250 K. Deposition angles ranging from normal incidence up to 50° result in the formation of {115} facets at all sides. At larger off-normal incidence angles steeper slopes develop. Deposition at grazing incidence angles (above 75°) results in the steepest facets, e.g. {111} facets, at all sides. In the range $60° - 75°$ illuminated slopes develop into steeper slopes compared to the shadow side, while the left/right sides are still close to {115} facets. The slopes derived from the simulations are compared to the experimental results obtained by van Dijken [7, 8]. Figure 7.5 demonstrates a compelling agreement between simulations and experiment.

For grazing incidence, the simulations indicate the presence of a combination of two facets at the shadow and left and right side, a {111} and a {113} facet. The latter is less intense and therefore less clearly present. An analysis of the simulated morphologies shows that these {113} facets are located at the bottom of the mound structures. The presence of two facets is first noted for the shadow site. Experimentally, the presence of two facets was only observed for extreme grazing incidence deposition (85°) [8].

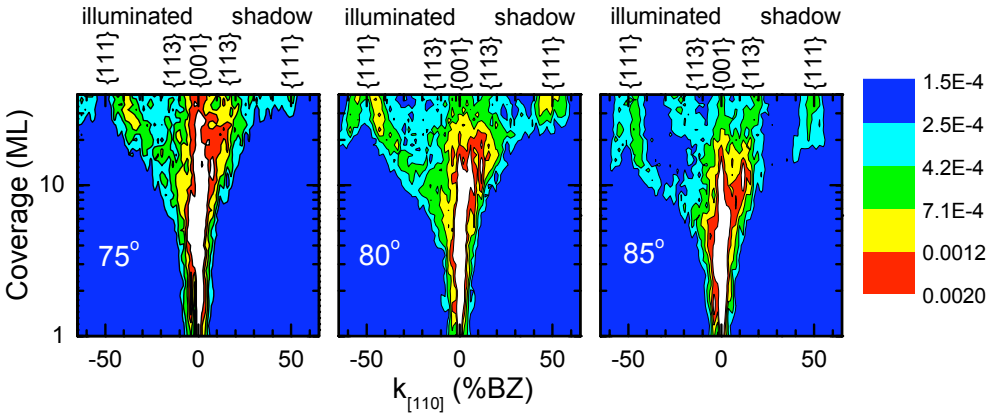

Figure 7.6: Intensity diffraction linescans along [110] direction at a diffraction condition of $S_z = 3.25$ during simulated growth from 1 till 40 ML for different deposition polar angles: 75°, 80° and 85°. Time and thus film thickness increases from bottom to top. The other settings in the simulation are $T = 250$ K and $R = 1$ ML/min. Under these conditions intensity corresponding to {111}, {113} and {115} oriented facets would show up at respectively $k_{[110]} = 50$ %BZ, $k_{[110]} = 33$ %BZ and $k_{[110]} = 17$ %BZ, as indicated along the topside of the panels.

Summarizing the results so far: Our kMC simulation scheme was used with diffusion barriers based on the results obtained for normal incidence growth. The strength of the dipole interaction between the incoming particles and the surface was derived from sub-monolayer deposition experiments. No further adjustment to the simulations presented was made. A very good agreement between the orientation of the facets is observed for experiments and simulations on films grown at different deposition geometries. We conclude from this similarity that our simulation scheme is well suited for describing homoepitaxial growth experiments on Cu(001) up to 40 ML coverage in a temperature regime from 230 - 290 K. This conclusion allows us to inspect more closely the evolution of the surface morphology at oblique incidence by performing extensive simulations.

7.5 Evolution of facet slopes at grazing incidence

The slopes of the four sides of the mounds evolve during growth and consequently the related surface truncation rods emerge in reciprocal space. The development of the facet truncation rods in time can be monitored by plotting $k_{[110]}$ and $k_{[1\bar{1}0]}$ intensity linescans at fixed phase S_z versus the coverage. Figure 7.6 shows the evolution of diffracted intensities at the illuminated and shadow side of the mounds for three

different grazing deposition angles (75°, 80° and 85°) at $T = 250$ K. A diffraction phase condition of $S_z = 3.25$ was used under these conditions. Intensity of {111}, {113} and {115} facet surface truncation rods show up at, respectively, $k_{[110]} = \pm 50$ %BZ, $k_{[110]} = \pm 33$ %BZ and $k_{[110]} = \pm 17$ %BZ. (− for the illuminated side, and + for the shadow side).

After depositing about 5 ML, intensity corresponding to quite well defined slopes on the illuminated and shadow sides are observed in the plots in fig. 7.6. The slopes on the illuminated side develop gradually from a relatively small slope toward a {111}-like facet. Note that the separation of the facet truncation rods seen at the illuminated side in fig. 7.3 at phase $S_z = 3.25$ shows up as intensity on the left and right hand side of the exact position of a perfect {111} facet in fig. 7.6. It is seen that the separation decreases during growth, indicative of a gradual increase of the terraces that form the {111} facets. The shadow side shows a rather abrupt change in the facet orientation around 20 ML for deposition at a polar deposition angle of 85°. For a polar deposition angle of 80° this change towards a {111} facet on the shadow side is also less gradual as observed for the illuminated side and occurs around 28 ML. The observation of {111} facets on the shadow side is accompanied by the appearance of facets on the left and right side of the mounds (not shown). The facets on these sides are initially not as well defined as those on the shadow side. This is a direct result of the elongation of the mounds perpendicular to the plane of incidence of the deposition beam. The left and right side have a relatively small area and hence a lower intensity of the facet rod.

The illuminated side shows as previously discussed, a slightly smaller slope than that of a {111} facet. This phenomena is observed in fig. 7.6 with the development of intensity on both sides of the {111} position ($k_{[110]} = -50$ %BZ at $S_z = 3.25$). A careful inspection of the real space morphology reveals that the illuminated mound side has on average two {111} terraces separated by a monoatomic step edge. We attribute the presence of two large terraces to the particular growth mode at oblique incidence deposition. Steering results in a relatively high flux at the top of the illuminated side. The newly deposited atoms diffuse rapidly over the upper {111} terrace on the illuminated side and become incorporated in the step edge that separates the upper and lower terrace. This stepedge is a virtually impermeable barrier for diffusion to the lower terrace. A diffusion process over this step edge requires a local uphill diffusion step. The lower terrace expands, while the upper terrace shrinks in size. The high flux on the illuminated side results in a very rapid movement of the step edge towards the top of the mound. Only when a step edge approaches the top of the mound, sufficient adatoms will be deposited on the lower terrace to facilitate the move of the next step edge up the hillside. On average, only one step edge will

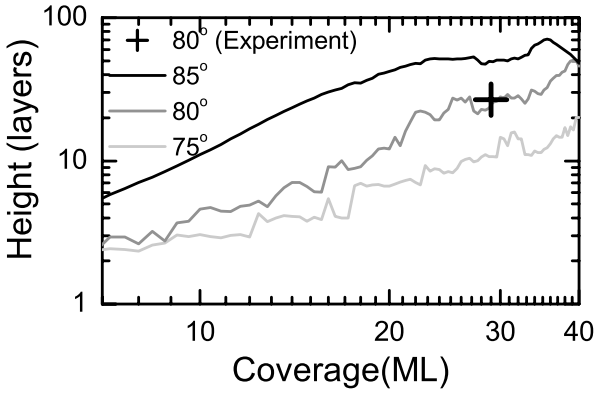

Figure 7.7: Estimated mound height as a function of film thickness in monolayers deposited at $T = 250$ K and at deposition polar angles of 75°, 80° and 85°. The + represents the experimentally determined mound height after depositing 29 ML at a polar deposition angle of 80° and at $T = 250$ K and a deposition rate of 0.5 ML/min.

be present on the illuminated side. In other words, the facet grows in a local step propagation mode. This implies that the average length of the terrace as deduced from diffraction can be used as measure for the average height of the mounds in the plane of deposition. The average height can be calculated from the normalized separation along $k_{[110]}$ of the {111}-like facet rods. (Note that the separation is directly related to the angle of the facet surface truncation rods. After depositing 29 ML at a deposition angle of 80° at $T = 250$ K, the separation is 13 %BZ, which gives $H = 27.8$ interlayer distances (4.8 nm).

This evolution of the mound height as a function of deposition angle is depicted in fig. 7.7. A strong increase of the roughness is observed for especially very grazing incidence (85°) deposition. Only for the very grazing incidence deposition the height of the mounds stabilizes. After about 22 ML deposition a mound height of 50 layers is found and is related to the change in orientation of the mounds as observed in fig. 7.1. For 80° polar angle of deposition the height is expected to stabilize around 40 ML as already a considerable part of the mounds visible in fig. 7.1 have rotated and are elongated parallel to the plane of deposition. Figure 7.7 also contains the measured experimental value after depositing 29 ML at 250 K. This experimental point corre-

sponds well to the simulated values as is also expected from the similarity between the experimental and simulated facet truncation rods in fig. 7.3. The separation between facet truncation rods is an experimentally accessible parameter and can be used to compare simulated and experimental results on the strong roughening of the surface during growth. This roughening will be further analyzed by evaluating the root mean square roughness.

7.6 (Super) Roughening at grazing incidence

The Root Mean Square (RMS) roughness of an interface is probably the most common quantity for providing roughness information. Scaling theory is often used to provide a theoretical context for the behaviour of the interface roughness w [71]. Kinetic roughening during multilayer growth develops according to this theory as $w \propto \theta^{\beta}$, where β is the kinetic roughening or growth exponent. The simulation results in chapter 5 showed that $\beta = 0.5$ for growth at normal incidence and temperatures between 250 K and 275 K. Below and above these temperatures lower values for β were found, indicating smoother growth. Figure 7.8 c) shows the roughness development for growth at a polar deposition angle of 40°. This roughness development is very similar to that for normal incidence growth. Initially a layer-by-layer growth is observed, followed by a regime characterized by an increase in roughness with coverage described by $\beta \approx 0.5$. This value of the growth exponent is very often associated to a Poisson growth mode. The Poisson growth mode is defined as a deposition process on a simple cubic Kossel crystal with on-top adsorption sites and no interlayer transport. This is usually considered as the roughest growth mode possible and the roughness is the result of statistical variations in the deposition flux [91].

The simulated morphologies for grazing incidence deposition show, similar to normal incidence deposition, at first a layer-by-layer like evolution of the RMS roughness, see fig. 7.8. However, already after 3 ML the roughness starts to increase dramatically compared to normal incidence growth. Already at this time the growth exponent is above the Poisson value of $\beta = 0.5$. The growth mode at grazing incidence in this coverage regime is therefore denoted as "Super Poisson" roughening. The increase in roughness is very fast. For very grazing incidence (85°), we find a value of $\beta = 1.8$ around 10 ML coverage. Although initially a layer-by-layer growth is observed, the roughness itself is now larger than the value obtained for continuous Poisson growth at all thicknesses. The growth exponent β can also be derived from fig. 7.7. The height increase with coverage for 85° polar angle of incidence also follows a power law with a value of 1.9 for the exponent. Note that the latter exponent is more easily accessible experimentally compared to an experimental evaluation of the change of

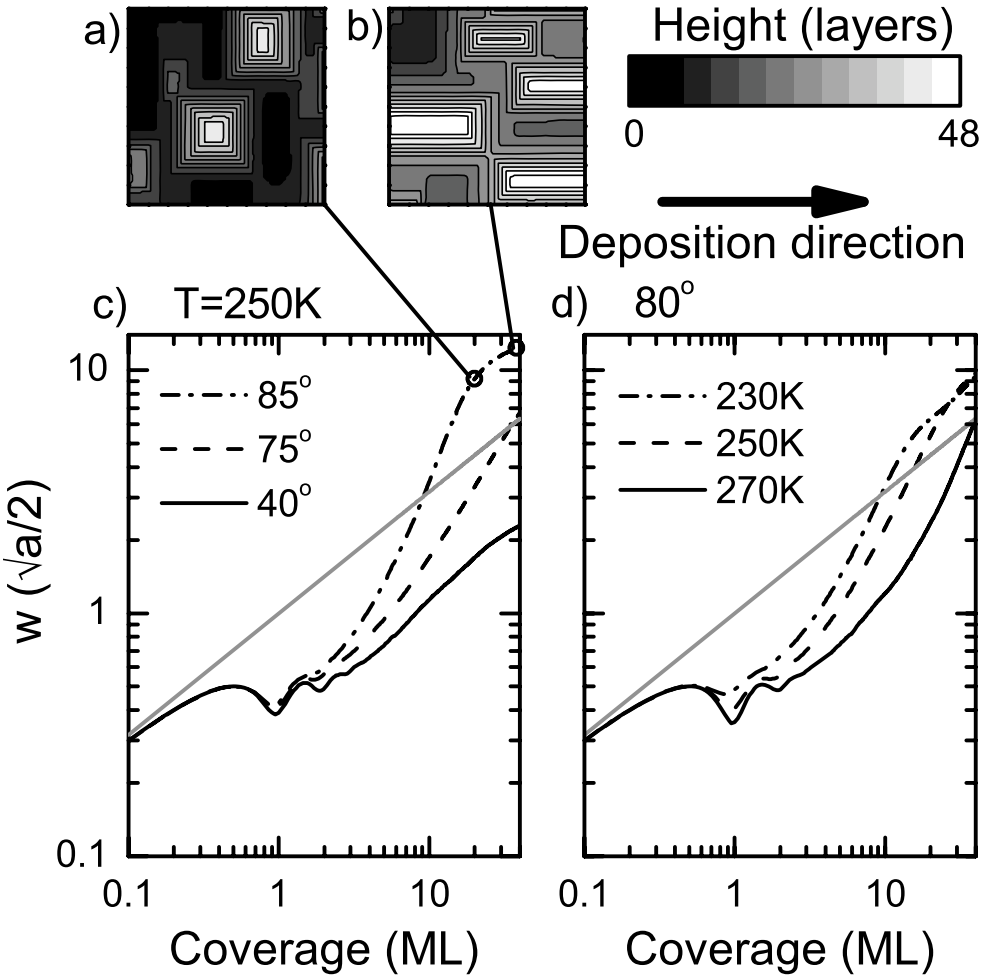

Figure 7.8: Roughness development during simulated growth at different polar angles of incidence for $T = 250$ K and a deposition rate of 0.5 ML/min. (c), and at different temperatures for a polar angle of 80° (d). The gray line indicate the roughness development corresponding to Poisson growth. a) and b) show the morphology at and just after a strong reduction in the value of the exponent β at 85°. The surface consists of pyramid structures at this change in growth exponent, while just after the surface consists of structures elongated parallel to the deposition beam. Both snapshots are 25 $\times$ 25 nm^2.

the RMS roughness with coverage.

The super roughening for very grazing incidence deposition angle (85°) starts to flatten after a deposition of about 20 ML and a more moderate increase of the roughness with coverage is observed, see fig. 7.8 c). This transition coverage is similar to the change in mound height evolution observed in fig. 7.7 and is accompanied by a dramatic change in morphology, as illustrated by the morphology in fig. 7.8 a) and b). At the start of the Super Poisson roughening stage, the surface is covered with mesa structures elongated perpendicular to the deposition beam. However, at the super roughening growth these mesas also transforms into pyramids, which have a growth behaviour different from that of the mesa structures. The pyramids grow mainly toward the deposition source (up-stream), being transformed into structures elongated parallel to the deposition beam. These latter structures have negligibly small top (001) terraces, in contrast to the elongated mesa structures observed before the transition.

The influence of substrate temperature on the roughness is illustrated for a grazing deposition polar angle of 80° in fig. 7.8 d). The coverage at which the roughness enhancement starts is temperature dependent: it occurs earlier at lower temperature. There are two reasons for this. Firstly, the enhanced flux on the top terrace is leveled out over a larger area for higher temperatures. Secondly, interlayer transport is an activated process which is thus much more active at higher temperatures. At a high temperature sufficient thermally generated kinks are present in the top layer during a longer growth time to maintain interlayer transport. Note, that even the highest simulated temperature of $T = 270$ K is not enough high to allow a roughening rate equal to that observed at normal incidence deposition.

For $T = 230$ K and 80°, the roughness evolution is quite similar to the one observed for $T = 250$ K 85° in the super roughening stage. In both simulations their overall roughness extends the Poisson roughness after depositing ∼9 ML. The transition point for $T = 230$ K (80°) is near 11 ML deposition, which is earlier than that for $T = 250$ K (85°). It is caused by the higher adatom island density during sub-monolayer growth at lower temperatures due to reduced adatom mobility. This also leads to the slightly higher density of elongated structures seen after the transition point for $T = 230$ K (80°) compared to $T = 250$ K (85°), see fig. 7.1 A and E.

In the initial stage of grazing incidence growth, the effect of steering is weak, because the already present mounds are small in volume. Gradually these mounds grow in size, and as a consequence steering leads to an enhanced heterogeneity of flux across the surface. Due to steering, small protruding areas receive a relatively high flux, while extended areas in the shadow regions behind islands receive a relatively low flux. As a result an asymmetric distribution of exposed layers arises. Figure 7.9

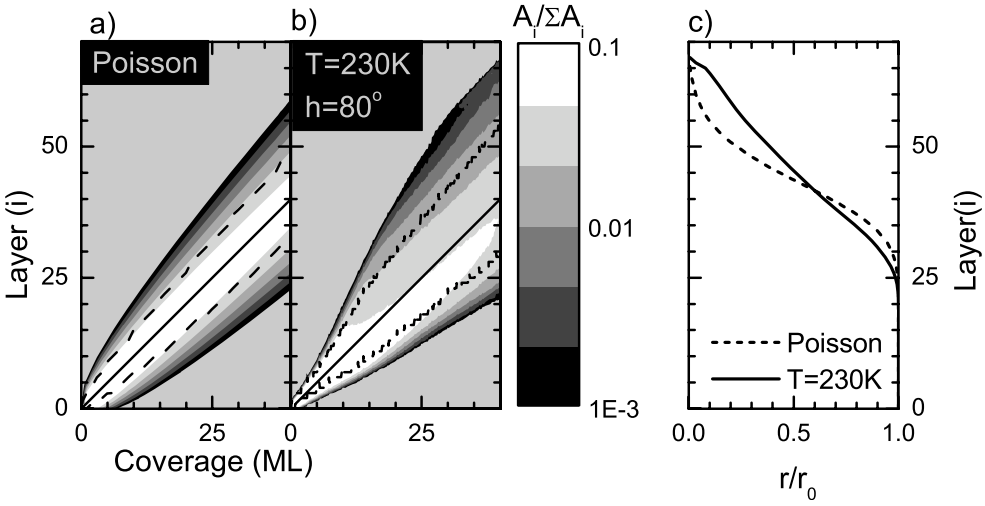

Figure 7.9: Exposed surface area A_i per layer i versus coverage during a) ideal Poisson growth and b) simulated growth at $T = 230$ K and at grazing incidence angle of 80°. The solid line represents ideal layer-by-layer growth and the separation between top and down half of the morphology. The layers per coverage in between the dashed lines represent the middle 90% of the exposed area in the morphology. The average shape of the mounds after 40 ML deposition is shown in c). The average radius r_i of layer A_i for grazing incidence growth (solid line) and Poisson growth (dashed line) is depicted. The radius is normalized to the average radius of the mounds r_0.

shows the distribution of exposed layers for grazing incidence deposition at 230 K. For comparison, also distribution of exposed layers for ideal Poisson growth is shown. In Poisson growth an immediate expansion of the number of exposed layers occurs. The statistical deposition process results in a smaller expansion rate of exposed layers with increased deposition. Eventually the distribution becomes symmetrical, i.e. a Gaussian distribution of the exposed layers evolves and the mean of the distribution is equal to the deposited amount of material. A different behavior is observed for the simulated grazing incidence growth, see fig. 7.9 b). The initial layer by layer growth results in a more condensed distribution of exposed layers due to relevant interlayer diffusion. After deposition of about 3 ML the super roughening stage is entered and this leads to a steep increase of the number of exposed layers. At first glance, the distribution of areas A_i of the lower exposed layers i look similar to that in Poisson growth. The main difference is in the top layers. The present mesa structures in super roughening growth have (001) terraces on top, resulting in larger exposed areas than in Poisson growth. Around 22 ML these mesa structures completely change and one by one they transform in pyramids. This effect is clearly visible in fig. 7.9 b) in the region of 20 to 30 ML. The outermost 5% of the deposited material is compared to the Poisson case, distributed in many more exposed layers. The transition from mesa structures into pyramids elongated parallel to the plane of incidence is gradual because the mesas vary in lateral dimensions. The presence of many exposed layers after the transition is a result of the small top terraces on the pyramids and the presence of {111} facets. These facets provide a much less peaked distribution of exposed layers for the grazing incidence growth compared to the Poisson distribution. Note that fig 7.1 d shows a nice example of the gradual transition. The small mound structures have already been transformed in elongated structures parallel to the deposition beam, while the largest structures are still elongated mesas perpendicular to the beam.

The distribution of layer coverages, and therefore the average shape of the mounds, was studied for the homoepitaxial growth on Pt(111) with the so-called wedding cake description [91–93]. Anisotropy in the mound shape is removed by transforming the layer coverage into circular discs. The average radius of each layer is plotted versus the layer number. For Pt(111) a fair similarity in shape between the actually grown mounds and a Poisson distributed growth was observed. For grazing incidence growth at 230 K, a similar shape analysis is depicted in fig. 7.9 c) for a 40 ML thick Cu film on Cu(001). A much broader distribution is observed for grazing incidence growth. The average shape after grazing incidence growth consists of several straight sections, illustrating extensive facet formation. Compared to Poisson growth, a smaller amount of material is present at the larger radii. This mass has been transferred to islands with a small radius, located at higher layer levels than in Poisson growth. Such a

phenomenon (super Poisson roughening) requires a so-called uphill flux. The required extensive uphill flux is a true signature of a considerably heterogeneous flux distribution, i.e. flux steering to the highest protrusions. The top layer in grazing incidence growth has a relatively small area. The size of the top layer was used for Pt(111) to establish the Ehrlich Schwoebel barrier on this surface. In the present case, the size of the adatom island is too small for such an analysis.

Super Poisson roughening already starts around 3 ML, while up to 1 ML coverage a very similar growth to normal incidence growth is observed. The initiation of the strong roughening has therefore to occur between 1 and 3 ML coverage. At submonolayer coverage, only a slight elongation of the adatom islands takes place, see chapter 6. This elongation is the result of steering. An enhanced flux will impinge on top of an adatom island near the illuminated side. A relatively large part of this enhanced flux will descend over the step edges of the adatom islands as only limited nucleation has occurred in the second layer after 1 ML deposition. Interlayer mass transport will take place almost exclusively via the kinks in the $\langle 110 \rangle$ step edges. The enhanced flux leads to a decrease in the density of kinks and as a result a decrease of the interlayer transport. Simulations around 2.5 ML show indeed a slightly smaller number of kinks at the illuminated side of adatom islands. The reduced interlayer transport initiates a faster nucleation in the next layer which in turn increases the steering effect. In this way a cyclic pattern that accelerates roughening is created. The roughening is limited by the formation of the steepest facet possible, i.e. $\{111\}$ facets. Large elongated islands that lead to ripple formation require a substantial steering effect combined with sufficient interlayer mass transport.

7.7 Conclusion

A wide variety in morphology of mounds evolves depending on temperature, polar angle of incidence of the deposition beam and the coverage. The formation of a well defined ripple pattern is obtained for the higher temperatures studied, i.e. around 270 K. Large elongated mounds perpendicular to the deposition beam and very well ordered parallel to the deposition beam have been found.

The obtained similarities between simulations and diffraction experiments in terms of the formation and evolution of facets, as well as the growth behavior of the illuminated side that results in the formation of parallel facet truncation rods indicate that the simulations quite accurately describe the growth at oblique incidence. The simulated morphologies are the result of an accurate incorporation of interlayer transport and the steering effect. This allows to use the simulation results for a more detailed study of the growth behavior. The illuminated side of the mounds formed after only

deposition of a few layers show a strong increase in slope, while the shadow side and left and right sides show this strong increase much later. This culminates in the development of {111} facets first at the illuminated side, followed later by the other three sides. This growth behavior is observed for the temperatures studied, i.e. 230 - 270 K and for polar angles of incidence above 70°.

The illuminated {111} facet exhibits in a remarkable growth behavior. A large part of the illuminated side is formed by two {111} terraces, separated by a step edge. Material transport over the terrace close to the top of the mound results in incorporation of all material in the ascending step edge, usually referred to as step propagation growth. This step edge will thus move to the top of the mound. Upon arrival, a next step edge has already started its ascent at the bottom of the mound. The presence of the step edge results in a characteristic diffraction pattern of two parallel facet truncation rods. Their orientation or equivalently their separation provides direct information on the average height of the mound structures. Both experiment and simulation show extreme roughening occurring at grazing incidence deposition. The RMS roughnesses evaluated from the simulated morphology support this observation and show a roughening behavior with a growth exponent β much larger than the Poisson value of 0.5. Oblique incidence deposition thus leads to Super Poisson roughening. This extreme growth mode leads to a change of the mound structure in pyramid-like structures. The formation of pyramids also ends the elongation of the mounds perpendicular to the deposition beam with increasing deposition. Increase of coverage therefore results in a change in orientation of the elongation. Large elongated islands parallel to the deposition beam are formed. However, the ordering of the structures remains the same, i.e. the well defined distance in the direction parallel to the deposition beam is conserved.

Summary

The evolution of the morphology of thin films during deposition at grazing incidence leads to the formation of intrinsically anisotropic structures. This phenomenon is of both fundamental and practical interest. In technology this feature is exploited to manufacture tapes for perpendicular magnetic recording and also for producing optical filters with a narrow transmission window. The physical principles underlying the anisotropy of thin films deposited at grazing incidence long remained a mystery. Quite recently, experiments performed in my host group revealed that long range attractive forces, exerted on the gas phase atoms by the substrate, are responsible for the obtained anisotropy. These so-called dispersion forces are responsible for an effect coined as steering. Due to steering protrusions at the surface receive a relatively high flux of atoms while the flux on indentations is relatively low. This thesis deals with a systematic theoretical and experimental study on steering induced flux heterogeneity and its consequences for the evolving morphology of the growth front during deposition. The homoepitaxial growth of Cu(001) has been elected as a prototype system.

First a powerful kinetic Monte Carlo (kMC) code has been developed, suited for a cost efficient investigation of the development of the growth front during (at wish) perpendicular or off- normal deposition. It is based on activation barriers for a variety of diffusion processes as they are available from literature. It encompasses a realistic face centered cubic lattice structure and includes the influence of dispersion forces on the exact shape of the trajectories of the arriving gas phase atoms, thus accounting fully for flux heterogeneity at the actually growing surface by calculating the impact position of each individual atom. A decisive step in the accommodation

of deposited atoms is the final incorporation of the arriving atom in a lattice position. To mimic reality a simple condensation rule has been developed and tested thoroughly by using molecular dynamics, MD, simulations. This work has been done during two extended visits to the group of prof. Rahman, at those times still at her Kansas State University affiliation. A comparison of kMC - with MD results demonstrates a convincing agreement. Several acceleration steps have been implemented subject to continuous scrutiny of unwanted/unrealistic implications. Finally, it turned out to be feasible to calculate the evolution of the growth front during growth of about one monolayer at a deposition rate of one monolayer per second on an average present-day desktop computer in one day. Our kMC code allows simulations at realistic, i.e. experimentally easily accessible deposition rates and temperatures up to 290 K. Considerably enhanced capacity has been organized by setting up a flexible and powerful server-client based network allowing the execution of parallel simulations on a sizeable number of desktop computers. This set-up allows the direct comparison of results of realistic simulations with experimental data.

The first topic is a description of the roughening of the growth front during initial growth stages. This is of particular interest since the activation barrier for interlayer diffusion, the so-called Ehrlich-Schwoebel barrier, is hard to calculate theoretically. In addition, experimental estimates are rather widely spread too. Moreover, it is well known that the Ehrlich-Schwoebel barrier for descent across a straight, close-packed [110] step segment is much higher than that for descending across a kink site associated with a small [100] step segment on the {001} surface. Experimentally the roughness during growth is probed by looking at the height of a thermal energy helium beam, specularly reflected from the growing surface. Layer-by-layer growth gives rise to temporal oscillations and the height of the first maximum, i.e. after deposition of the first monolayer serves as a measure of roughness: a high intensity maximum corresponds to a smooth film and vice versa. Oscillation curves are calculated from the simulations applying the kinematic approximation. Based on the data for the first intensity maximum it appears possible to identify Ehrlich-Schwoebel barriers that allow an accurate description of the experimental results in a relatively wide temperature range from 230 to 290 K. It has been possible to determine the height of the corresponding Ehrlich-Schwoebel barrier: -5meV with unanticipated accuracy. Since the vast majority of interlayer diffusion steps occur through kink sites one can only impose a lower limit of 120 meV for descent across the [110] step. With these obtained values the growth oscillations are described accurately for at least three monolayers and deposition rates varying by an order of magnitude. One therefore can safely conclude that the kMC code contains the essentials of the involved growth physics. This also implies that the used values of the activation barriers for the

relevant processes must necessarily be quite accurate.

Another issue is the shape of the gas phase - substrate interaction potential and especially the range of the involved dispersion forces. This information is accessible by studying the initial growth behaviour, more in particular the anisotropy of the adatom islands during deposition at grazing incidence. The enhanced flux on top of the islands depends strongly on the range of the attractive potential. The redistribution of this flux, which gives rise to shape anisotropy, or more specific elongation of the islands perpendicular to the plane of incidence of the arriving atoms, depends on the just determined Ehrlich-Schwoebel barrier. The results, obtained in the coverage range between 0.25 and 0.7 monolayers, from high resolution LEED experiments have been compared to those obtained by application of the kinematic approximation for simulated morphologies. The three different potentials for the description of the dispersion forces give rise to distinctly different variation of the anisotropy of the islands with coverage. The results clearly show convincing agreement between simulations and experiments for a modified Lennard Jones potential, which also accounts properly for the optical properties of copper.

Obviously flux heterogeneity is not only determined by the actual surface morphology and the deposition geometry, but does depend also strongly on the velocity of the gas phase atoms. Therefore, more detailed information on the exact range dependence of dispersion forces may well be available from experiments with monochromatic beams. Their production, however, poses a major challenge. Please note that thermal particle sources generate atoms with a cosine angular distribution and Maxwellian velocity distribution. The generation of a well defined atomic beam thus requires a double cut from two intrinsically very broad distributions and will give soon rise to low intensities also keeping in mind that the accessible temperature window is quite narrow. Therefore, in order to leave reasonable intensities the velocity selector has to be very compact. The design and manufacturing of the required velocity selector has turned out to be technologically involving. The result is highly encouraging: a compact selector has been realized with a transmission of roughly 50% and a sufficient monochromaticity of 10%. Unfortunately the realization process has suffered from many delays outside of our control. However, the future experiments along the above lines will benefit from the presence of a suitable and devoted velocity selector.

Growth simulations for a wider coverage range up to 40 monolayers have been performed for off-normal deposition geometries and substrate temperatures between 230 and 270 K. The obtained morphology evolution shows a strong tendency for rotation of the anisotropy from initially perpendicular to the plane of incidence to parallel to the plane of incidence at extended growth. This behaviour is most prominent at quite extremely grazing incidence. Its appearance and in particular the film thickness at

which the elongated structures rotate does depend does depend on temperature and deposition geometry. The simulations can be used to identify optimum conditions for, and guidance of, future experimental verification of this feature. The availability of the above mentioned velocity selector will be instrumental in doing so.

Finally, the evolution of the vacuum-film interface of the growing film has been evaluated. For a homogeneous flux distribution and in the complete absence of interlayer mass transport a Poisson distribution of exposed layers is expected. The critical exponent for roughness development then corresponds to 0.5. For off-normal deposition geometries, however, much larger critical exponents have been found. This feature is referred to as super Poisson growth and clearly indicates a strong uphill current. This is strongly favoured by steering effects leading to high fluxes on top of protrusions (mounds) and as such provides additional evidence for the importance of dispersion forces in, especially, off-normal deposition processes.

Samenvatting

Het onder scherende hoek deponeren van materiaal tijdens de groei van dunne films leidt tot het ontstaan van intrinsiek anisotrope structuren. Dit fenomeen is zowel van fundamentele als van praktische interesse. Technologisch biedt dit de mogelijkheid om tapes voor magnetische data opslag te produceren met loodrechte magnetisatie. Een andere toepassing betreft de productie van optische filters met een nauwe bandbreedte. De natuurkundige principes die verantwoordelijk zijn voor het ontstaan van vorm anisotropie bij filmgroei onder scherende inval bleven lang onopgehelderd. Met behulp van recentelijk in mijn vakgroep uitgevoerde experimenten kon aangetoond worden, dat de door het substraat op de gas atomen uitgeoefende krachten, met een lange dracht, verantwoordelijk zijn voor het ontstaan van vorm anisotropie. Deze dispersie-krachten zijn verantwoordelijk voor een effect dat als "steering" is gedoopt. Door "steering" valt op uitsteeksels op het oppervlak een relatief hoge flux atomen, terwijl de flux op putjes in het oppervlak relatief laag is. Dit proefschrift beschrijft een systematisch theoretisch en experimenteel onderzoek aan de door "steering" veroorzaakte flux heterogeniteit en de consequenties daarvan op de zich ontwikkelende morfologie van het groeifront tijdens depositie. Het onderzoek is uitgevoerd voor de groei van Cu op Cu(001), dat we beschouwen als een typisch model systeem.

Allereerst werd een krachtige kinetische Monte Carlo (kMC) code ontwikkeld, die geschikt is om efficiënt de ontwikkeling van het groeifront tijdens (naar keuze) loodrechte of schuine depositie te kunnen beschrijven. Hij is gebaseerd op uit de literatuur bekende activeringsbarriéres voor verschillende diffusieprocessen. Hij is gebaseerd op een realistische vlakken gecentreerde kubische roosterstructuur en houdt rekening met de invloed van dispersiekrachten op de exacte baan van de arriverende atomen

in de gas fase. Met andere woorden, er wordt volledig rekening gehouden met de flux heterogeniteit voor elk momentane morfologie van het groeifront. Een kritische stap wordt gevormd door de definitieve opname van het arriverende atoom in een rooster positie. Om de werkelijkheid te beschrijven, is er een condensatie regel ontwikkeld die grondig is getest met moleculair dynamische (MD) simulaties. Dit testwerk is gedaan tijdens twee langere bezoeken aan de groep van prof. Rahman, destijds nog verbonden aan de Kansas State University. Een gedetailleerde vergelijking tussen kMC en MD resultaten laat zien dat de gekozen condensatieregel uiterst betrouwbaar de in MD berekeningen gevonden incorporatie van atomen beschrijft. Meerdere versnellingsstappen zijn geïmplementeerd, waarbij steeds nauwlettend werd gecontroleerd of er geen ongewilde/onrealistische implicaties ontstonden. Uiteindelijk bleek het mogelijk om, met behulp van een modale hedendaagse desktop computer, in ongeveer een dag de evolutie van het groeifront te beschrijven voor de groei van n monolaag voor een depositiesnelheid van een monolaag per minuut. Onze kMC code kan simulaties doen bij realistische, dat wil zeggen experimenteel gemakkelijk toegankelijke depositiesnelheden en temperaturen tot ca. 290 K. Een sterk uitgebreide capaciteit kon worden verkregen door het opzetten van een flexibel en sterk server-klant gericht netwerk. Dit maakte het mogelijk om parallel simulaties op een willekeurig aantal beschikbare desktop computers te laten uitvoeren. Hiermee konden resultaten van realistische simulaties en experimentele data op een directe manier vergeleken worden.

Het eerste onderwerp is een beschrijving van de verruwing van het groei front tijdens de initiële groeifase. Dit is van bijzonder belang omdat de activeringsbarriére voor diffusie tussen lagen, de Ehrlich-Schwoebel barriére, moeilijk theoretisch te berekenen is. Bovendien blijken de experimentele schattingen voor deze barriére behoorlijk van elkaar te verschillen. Het is algemeen bekend, dat de Ehrlich-Schwoebel barriére voor een [110] stap segment veel hoger is dan die voor een [100] segment. Dat laatste wordt geassocieerd met een kink positie in de [110] stap op een {001} oppervlak. Experimenteel wordt de ruwheid tijdens groei gesondeerd m.b.v. de hoogte van de gespiegelde piek in de verstrooiing van thermische helium atomen. Laag voor laag groei resulteert in een periodiek oscillerende piekhoogte. De hoogte van het eerste maximum, d.w.z. na depositie van de eerste laag, dient als een maat voor de ruwheid: een hoog maximum correspondeert met een gladde film and vice versa. De z.g. groei-oscillaties zijn berekend uit de gesimuleerde groeifronten onder toepassing van de kinematische benadering. Gebaseerd op de data van het eerste intensiteit maximum, blijkt dat het mogelijk is de Ehrlich-Schwoebel barriére te identificeren, waarmee de experimentele resultaten in een relatief groot temperatuur gebied van 230 tot 290 K nauwkeurig worden beschreven. Dit staat een accurate bepaling van

de hoogte van de verantwoordelijke Ehrlich-Schwoebel barrière toe: -5 meV met een onverwachte nauwkeurigheid. Omdat het overgrote deel van de interlaag diffusie via de kinks gebeurt, kan voor een de Ehrlich-Schwoebel barriére voor een rechte [110] stap alleen de ondergrens van 120meV vastgelegd worden. Met de op deze manier verkregen waarden kunnen de groei oscillaties nauwkeurig worden beschreven voor ten minste 3 monolagen en een variatie in de depositiesnelheid van een orde van grootte. Daarom kan men veilig concluderen dat de kMC code de essentile ingredinten van de betrokken fysica betrouwbaar beschrijft. Dit betekent ook dat de gebruikte waarden van de activeringsbarriéres voor de relevante processen noodzakelijkerwijs behoorlijk nauwkeurig zijn.

Een ander thema is de vorm van de interactiepotentiaal tussen een gas fase atoom en het substraat, i.h.b. in het gebied van de betrokken dispersiekrachten. Deze informatie is toegankelijk door bestudering van het initiële groeigedrag en meer in het bijzonder de anisotropie van de atomaire eilanden tijdens depositie onder scherende inval. De versterkte flux boven op het eiland hangt sterk af van de dracht van de aantrekkende potentiaal. De herverdeling van deze flux, welke de vorm anisotropie veroorzaakt, of meer specifiek de uitbreiding van de eilanden loodrecht op het depositie vlak van de inkomende atomen t.o.v. die in het invalsvlak, hangt af van de zojuist bepaalde Ehrlich-Schwoebel barriére. De experimentele resultaten, zijn verkregen m.b.v. hoge resolutie LEED in het bedekkinggebied van 0.25 tot 0.7 monolagen. Deze metingen kunnen direct worden vergeleken met m.b.v. de kinematische benadering uit gesimuleerde groeifronten berekende profielen van diffractiepieken. De berekeningen werden uitgevoerd voor drie verschillende potentialen voor de dispersie krachten beschrijven, welke een duidelijk te onderscheiden variatie van de vorm-anisotropie van de eilanden met de bedekking laten zien. Het resultaat is een overtuigende overeenkomst tussen simulaties en experiment met de gemodificeerde Lennard Jones potentiaal, welke tevens de optische eigenschappen van koper juist beschrijft.

Natuurlijk wordt flux heterogeniteit niet alleen bepaald door de momentane morfologie van het oppervlak en door de depositie geometrie, maar hij hangt ook sterk af van de snelheid van het aanvliegende atoom in de gas fase. Daarom, is het goed mogelijk dat meer gedetailleerde informatie m.b.t. de dracht van de dispersiekrachten te halen valt uit experimenten met monochromatische bundels. Hun productie vormt echter een enorme uitdaging. Daartoe moet men bedenken dat thermische deeltjes bronnen atomen emitteren een cosinus(hoek)verdeling en een Maxwell(snelheids)verdeling. De generatie van een goed gedefinieerde atoombundel vergt dus een dubbele uitsnede van twee intrinsiek zeer brede verdelingen. Dit zal snel in een lage intensiteit resulteren, waarbij men eveneens bedenken moet, dat in de praktijk het beschikbare temperatuurbereik vrij klein is. Om een redelijke inten-

siteit over te houden moet de snelheidsselector zeer compact zijn. Het ontwerp en de productie van de benodigde snelheidsselector bleek een technologisch hoogstandje te zijn. Het resultaat is zeer bemoedigend: een compacte selector is gerealiseerd met een transmissie van ruwweg 50% en een voldoende monochromie van 10%. Helaas kon het device slechts met veel zich buiten onze invloedssfeer afspelende vertragingen gerealiseerd worden en kon er in het kader van dit promotieonderzoek geen nuttig gebruik meer van gemaakt worden. Toekomstige experimenten langs de hierboven uitgestippelde lijnen zullen echter in belangrijke mate kunnen profiteren van de aanwezigheid van de beschikbare snelheidsselektor.

Groeisimulaties voor dikkere films tot ca. 40 monolagen zijn uitgevoerd voor een scheve depositie geometrie en substraattemperaturen tussen 230 en 270 K. Gedurende groei bestaat een sterke tendens voor rotatie van de vorm- anisotropie. Initieel staat de overwegend langere as loodrecht op het invalsvlak en deze roteert langzaam naar parallel met toenemende bedekking. Dit gedrag is het meest prominent aanwezig tijdens extreem scherende inval. Deze rotatie en met name de film dikte waarbij de uitgestrekte structuren roteren, hangen af van de exacte temperatuur en van de depositie geometrie. De simulaties kunnen worden gebruikt om optimale condities voor te identificeren en dienen als gids voor toekomstige experimenten voor het verifiren van dit verschijnsel. De aanwezigheid van de compacte snelheidsselektor zal daarbij instrumenteel kunnen zijn.

Ten slotte is de evolutie van het oppervlak van de groeiende film gevalueerd. Voor een homogene flux verdeling en in complete afwezigheid van massa transport tussen lagen is een Poisson verdeling van de zichtbare telde lagen te verwachten. De kritische exponent die de ontwikkeling van de ruwheid beschrijft komt dan overeen met 0.5. Voor een scheve depositie geometrie, zijn echter nog veel grotere waarden voor de kritische exponent gevonden. Dit verschijnsel wordt ook wel beschreven als super Poisson groei en duidt duidelijk op een sterke "uphill current". Dit wordt zeer versterkt door de effecten van "steering", welke een hoge flux van inkomende atomen boven op bergen veroorzaakt. Deze waarnemingen leveren extra bewijs voor de belangrijke rol van dispersie krachten, in het bijzonder, wanneer de groei onder scheve depositie condities plaats vindt.

BIBLIOGRAPHY

[1] J. M. Nieuwenhuizen and H. B. Haanstra. Microfractography of thin films. *Philips Tech. Rev.*, 27:87, 1966.

[2] L. Abelmann and C. Lodder. Oblique evaporation and surface diffusion. *Thin Solid Films*, 305:1, 1997.

[3] G. Beydaghyan, K. Kaminska, T. Brown, and K. Robbie. Enhanced birefringence in vacuum evaporated silicon thin films. *Applied Optics*, 43:5343, 2004.

[4] H. E. Ruda, J. C. Polanyi, S. Y. Yang, Z. Wu, U. Philipose, T. Xu, S. Yang, K. L. Kavanagh, J. Q. Liu, L. Yang, Y. Wang, K. Robbie, J. Yang, K. Kaminska, D. G. Cooke, F. A. Hegmann, A. J. Budz, and H. K. Haugen. Developing 1D nanostructure arrays for future nanophotonics. *Nanoscale Res. Lett.*, 1:99, 2006.

[5] L. C. Jorritsma. *Growth anisotropy in Cu(001) homoepitaxy.* PhD thesis, University of Twente, 1997. ISBN 90-365-1021-1.

[6] S. van Dijken, L. C. Jorritsma, and B. Poelsema. Steering-enhanced roughening during metal deposition at grazing incidence. *Phys. Rev. Lett.*, 82:4038, 1999.

[7] S. van Dijken, L. C. Jorritsma, and B. Poelsema. Grazing-incidence metal deposition: Pattern formation and slope selection. *Phys. Rev. B*, 61:14047, 2000.

[8] S. van Dijken. *Pattern formation and magnetic anisotropy in thin metal films.* PhD thesis, University of Twente, 2000. ISBN 90-365-1459-2.

[9] D. E. Sanders and A. E. DePristo. Metal homo-epitaxy on fcc(001) surfaces - is there transient mobility of asdobed atoms. *Surf. Sci.*, 254:341–353, 1991.

[10] J. G. Amar. Effects of long-range interactions in metal epitaxial growth. *Phys. Rev. B*, 67:165425, 2003.

[11] J. G. Yu and J. G. Amar. Effects of short-range attraction in metal epitaxial growth. *Phys. Rev. Lett.*, 89:286103, 2002.

[12] M. M. Ovsyanko. *Ion sculpting of Cu(001).* PhD thesis, University of Twente, 2006. ISBN 90-365-2307-9.

[13] M. Esser. *Kinetically controlled Si-epitaxy on Si(100) and Ge(100).* PhD thesis, University of Twente, 2001. ISBN 90-365-1641-2.

[14] N. Esbjerg and J. K. Norskov. Dependence of the He-scattering potential at surfaces on the surface-electron-density profile. *Phys. Rev. Lett.*, 45:807, 1980.

[15] D. R. Hamann. Surface charge densities and atom diffraction. *Phys. Rev. Lett.*, 46:1227, 1981.

[16] J. Harris and A. Liebsch. Interaction of Helium with a metal surface: Determination of corrugation profile of Cu(110). *Phys. Rev. Lett.*, 49:341, 1982.

[17] B. Poelsema and G. Comsa. *Scattering of thermal energy atoms for disordered surfaces.* Springer tracts in modern physics vol. 115, 1989.

[18] E. Hulpke. *Helium Atom Scattering from Surfaces.* Springer Series in Surface Science 27, 1992.

[19] J.B. Pendry. *Low Energy Electron Diffraction.* Academic Press, London, 1974.

[20] M.A. van Hove and S. Y. Tong. *Surface Crystallography by LEED.* Springer, Berlin, 1979.

[21] J. Wollschläger. Simple analysis of spot splitting due to diffraction at surfaces with atomic steps. *Surf. Sci.*, 383:103, 1997.

[22] M. Horn von Hoegen. Growth of semiconductors layers studied by spot profile analysing low energy electron diffraction. *Z. Kristallogr.*, 214:1, 1999.

[23] J.W. Cowley. *Diffraction Physics.* North-Holland, Amsterdam, 1981.

[24] U. Scheithauer, G. Meyer, and M. Henzler. A new LEED instrument for quantitative spot profile analysis. *Surf. Sci.*, 178:441, 1986.

[25] G. Comsa and R. David. Dynamical parameters of desorbing molecules. *Surf. Sci. Rep.*, 5:145, 1985.

[26] L. I. Maissel and R. Glang. *Handbook of thin film technology.* McGraw-Hill, 1970.

[27] J. A. Collins. *Failure of materials in mechnical design.* Wiley, 1993.

[28] O. Biham, I. Furman, M. Karimi, G. Vidali, R. Kennett, and H. Zeng. Models for diffusion and island growth in metal monolayers. *Surf. Sci.*, 400:29, 1998.

[29] G. Ehrlich and F. G. Hudda. Atomic view of surface self-diffusion: tungsten on tungsten. *J. Chem.Phys.*, 44:1039, 1966.

[30] R. L. Schwoebel. Step motion on crystal surfaces. II. *J. Appl. Phys.*, 40:614, 1969.

[31] W. H. Press, B. P. Flannery, S. A. Tuekolsky, and W. T. Vetterling. *Numerical Recipes.* Cambridge University Press, 1986.

[32] J. G. Yu and J. G. Amar. Short-range attraction, surface currents, and mound formation in metal (111) epitaxial growth. *Phys. Rev. B*, 69:045426, 2004.

[33] H. Wormeester and B. Poelsema. Flux heterogeneity through incidence angle and particle energy in steering-enhanced growth. *Phys. Rev. B*, 66:165406, 2002.

[34] A. Lisfi, J. C. Lodder, H. Wormeester, and B. Poelsema. Reorientation of magnetic anisotropy in obliquely sputtered metallic thin films. *Phys. Rev. B*, 66:174420, 2002.

[35] E. Zaremba and W. Kohn. Van der waals interaction between an atom and a solid surface. *Phys. Rev. B*, 13:2270, 1976.

[36] Y. Mishin, M. J. Mehl, D. A. Papaconstantopoulos, A. F. Voter, and J. D. Kress. Structural stability and lattice defects in copper: Ab initio, tight-binding, and embedded-atom calculations. *Phys. Rev. B*, 63:224106, 2001.

[37] O.V. Lysenko, V.S. Stepanyuk, W. Hergert, and J. Kirschner. Mesoscopic relaxation in homoepitaxial metal growth. *Phys. Rev. Lett.*, 89:126102, 2002.

[38] D. Sander, S. Ouazi, V.S. Stepanyuk, D.I. Bazhanov, and J. Kirschner. Stress oscillations in a growing metal film. *Surf. Sci.*, 512:281, 2002.

[39] V.S. Stepanyuk, D.V. Tsivlin, D. Sander, W. Hergert, and J. Kirschner. Mesoscopic scenario of strain-relief at metal interfaces. *Thin Solid Films*, 428:1, 2003.

[40] O.V. Lysenko, V.S. Stepanyuk, W. Hergert, and J. Kirschner. Interlayer mass transport in homoepitaxy on the atomic scale. *Phys. Rev. B*, 68:33409, 2003.

[41] M. M. Ovsyanko, F. G. Stoian, H. Wormeester, and B. Poelsema. Novel local free energy minimum on the Cu(001) surface. *Phys Rev. Lett.*, 93:086103, 2004.

[42] I. Furman, O. Biham, J.-K. Zuo, A. K. Swan, and J. F. Wendelken. Epitaxial growth of Cu on Cu(001): Experiments and simulations. *Phys. Rev. B*, 62:R10649, 2000.

[43] T. R. Linderoth, S. Horch, E. Lgsgaard, I. Stensgaard, and F. Besenbacher. Surface diffusion of Pt on Pt(110): Arrhenius behavior of long jumps. *Pys. Rev. Lett.*, 78:26, 1997.

[44] O. S. Trushin, K. Kokko, P. T. Salo, W. Hergert, and M. Kotrla. Step roughening effect on adatom diffusion. *Phys. Rev. B*, 56:12135–12138, 1997.

[45] J. W. Evans, P. A. Thiel, and M. C. Bartelt. Morphological evolution during epitaxial thin film growth: Formation of 2D islands and 3D mounds. *Surf. Sci. Rep.*, 61:1, 2006.

[46] G. Rosenfeld, B. Poelsema, and G. Comsa. Epitaxial growth modes far from equilibrium. In D. A. King and D. P. Woodruff, editors, *The Chemical Physics of solid surfaces*, chapter 3, page 66. Elsevier, 1997.

[47] L. J. Gomez, S. Bourgeal, J. Ibez, and M. Salmerón. He scattering study of the nucleation and growth of Cu(100) from its vapor. *Phys. Rev. B*, 31:2551, 1985.

[48] J. J. de Miguel, A. Sanchez, A. Cebollada, J. M. Gallegoi, J. Ferron, and S. Ferrer. The surface morphology of a growing crystal studied by thermal energy atom scattering (TEAS). *Surf. Sci.*, 189/190:1062, 1987.

[49] J. Ferron, J. M. Gallego, A. Cebollada, J. J. De Miguel, and S. Ferrer. Epitaxial growth of metals: Experimental results and Monte Carlo simulation. *Surf. Sci.*, 211-212:797, 1989.

[50] H.-J. Ernst, F. Fabre, and J. Lapujoulade. Growth of Cu on Cu(100). *Surf. Sci.*, 275:682, 1992.

[51] L.C. Jorritsma, M. Bijnagte, G. Rosenfeld, and B. Poelsema. Growth anisotropy and pattern formation in metal epitaxy. *Phys. Rev. Lett.*, 78:911, 1997.

[52] R. Kunkel, B. Poelsema, L. K. Verheij, and G. Comsa. Reentrant layer-by-layer growth during molecular-beam epitaxy of metal-on-metal substrates. *Phys. Rev. Lett.*, 65:733, 1990.

[53] M. Li, J. F. Wendelken, Bang-Gui Liu, E. G. Wang, and Z. Zhang. Decay characteristics of surface mounds with contrasting interlayer mass transport channels. *Phys. Rev. Lett.*, 86:2345, 2001.

[54] P. Broekmann, A. Mewe, H. Wormeester, and B. Poelsema. Step edge selection during ion erosion of Cu(001). *Phys Rev. Lett.*, 89:146102, 2002.

[55] Ch. Teichert, Ch. Ammer, and M. Klaua. Step formation on the ion-bombarded Ag(100) surface studied by LEED and Monte Carlo simulations. *Phys. Stat. Sol. A*, 146:223, 1994.

[56] U. Kürpick and T. S. Rahman. Diffusion processes relevant to homoepitaxial growth on Ag(100). *Phys. Rev. B*, 57:2482, 1998.

[57] K. J. Caspersen, C. R. Stoldt, A. R. Layson, M. C. Bartelt, P. A. Thiel, and J. W. Evans. Morphology of multilayer Ag/Ag(100) films versus deposition temperature: STM analysis and atomistic lattice-gas modeling. *Phys. Rev. B*, 63:085401, 2001.

[58] P. A. Thiel and J. W. Evans. Energetic parameters for atomic-scale processes on Ag(100). *J. Phys. Chem. B*, 108:14428, 2004.

[59] P. Bedrossian, G. Poelsema, B. Rosenfeld, L. C. Jorritsma, N. N. Lipkin, and G. Comsa. Electron density contour smoothening for epitaxial Ag islands on Ag(100). *Surf. Sci.*, 334:1 – 9, 2000.

[60] H.-J. Ernst, F. Fabre, and J. Lapujoulade. Observation of dynamical scaling in 'spinodal decomposition' in two dimensions. *Phys. Rev. Lett.*, 69:458, 1992.

[61] H.-J. Ernst, F. Fabre, and J. Lapujoulade. Nucleation and diffusion of Cu adatoms on Cu(100): a helium-atom-beam scattering study. *Phys. Rev. B*, 46:1929, 1992.

[62] H.-J. Ernst, F. Fabre, R. Folkerts, and J. Lapujoulade. Observation of a growth instability during low temperature molecular beam epitaxy. *Phys. Rev. Lett.*, 72:112, 1994.

[63] J. B. Hannon, C. Klunker, M. Giesen, H. Ibach, N. C. Bartelt, and J. C. Hamilton. Surface selfdiffusion by vacancy motion: Island ripening on Cu(001). *Phys. Rev. Lett.*, 79:2506, 1997.

[64] J. K. Zuo and J. F. Wendelken. Evolution of mound morphologies in reversible homoepitaxy on Cu(100). *Phys. Rev. Lett.*, 78:2791, 1997.

[65] J. A. Venables. Rate equation approaches to thin film nucleation kinetics. *Phil. Mag.*, page 697, 1973.

[66] I. V. Markov. *Crystal Growth for Beginners*. World Scientific, Singapore, 1995.

[67] L. K. Verheij, B. Poelsema, and G. Comsa. Investigation of a randomly stepped Pt(111) surface using thermal energy atom scattering (TEAS). *Surf. Sci.*, 162:858, 1985.

[68] A. Sanchez and S. Ferrera. Cross section for diffuse scattering from random steps on Cu(100) determined by TEAS (thermal energy atom scattering). *Surf. Sci.*, 187:L587, 1987.

[69] B. Poelsema, S. T. de Zwart, and G. Comsa. Scattering cross section of low-coverage CO on Pt(111) for thermal He and H_2 beams. *Phys. Rev. Lett.*, 49:578, 1982.

[70] B. Poelsema, S. T. de Zwart, and G. Comsa. Scattering cross section of low-coverage CO on Pt(111) for thermal He and H_2 beams. *Phys. Rev. Lett.*, 51:522, 1983.

[71] A. L Barabási and H. E. Stanley. *Fractal concepts in surface growth*. Cambridge University Press, 1995.

[72] M. Siegert and M. Plischke. Slope selection and coarsening in molecular beam epitaxy. *Phys. Rev. Lett.*, 73:1517, 1994.

[73] H. Dürr, J. F. Wendelken, and J. K. Zou. Island morphology and adatom energy barriers during homoepitaxy on Cu(001). *Surf. Sci.*, 328:L527, 1995.

[74] C. E. Botez, P. F. Miceli, and P. W. Stephens. Temperature dependence of surface roughening during homoepitaxial growth on Cu(001). *Phys. Rev. B*, 64:125427, 2001.

[75] V. Borovikov, Y. Shim, and J. G. Amar. Effects of deposition angle in low temperature metal(100) epitaxial growth. *Phys. Rev. B*, 76:241401, 2007.

[76] R. Gerlach, T. Maroutian, L. Douillard, D. Martinotti, and H.-J. Ernst. A novel method to determine the Ehrlich-Schwoebel barrier. *Surf. Sci.*, 480:97, 2001.

[77] H.-J. Ernst, F. Fabre, R. Folkerts, and J. Lapujoulade. Kinetics of growth of Cu on Cu(001). *J. Vac. Sci. Technol. A*, 12:1809, 1994.

[78] F. Montalenti and A. F. Voter. Normal-incidence steering effect in crystal growth: Ag/Ag(100). *Phys. Rev. B*, 64:081401, 2001.

[79] Y. Shim and J. G. Amar. Growth instability in Cu multilayer films due to fast edge/corner diffusion. *Phys. Rev. B*, 73:035423, 2006.

[80] H. Brune, K. Bromann, H. Röder, K. Kern, J. Jacobsen, P. Stoltze, K. Jacobsen, and J. Norskov. Effect of strain on surface diffusion and nucleation. *Phys. Rev. B*, 52:R14380, 1995.

[81] H. Brune. Microscopic view of epitaxial metal growth: nucleation and aggregation. *Surf. Sci. Rep.*, 31:121, 1998.

[82] S. van Dijken, G. Di Santo, and B. Poelsema. Growth-induced uniaxial anisotropy in grazing-incidence deposited magnetic films. *Appl. Phys. Lett.*, 77:2030, 2000.

[83] J. G. Yu, J. G. Amar, and A. Bogicevic. First-principles calculations of steering forces in epitaxial growth. *Phys. Rev. B*, 69:113406, 2004.

[84] J. Seo, S. M. Kwon, H. Y. Kim, and J. S. Kim. Steering effect on the shape of islands for homoepitaxial growth of Cu on Cu(001). *Phys. Rev. B*, 67:121402, 2003.

[85] S. M. Foiles, M. I. Baskes, and M. S. Daw. Embedded-atom-method functions for the fcc metals Cu, Ag, Au, Ni, Pd, Pt, and their alloys. *Phys. Rev. B*, 33:7983, 1986.

[86] M. S. Daw, S. M. Foiles, and M. I. Baskes. The embedded-atom method: a review of theory and applications. *Mater. Sci. Rep.*, 9:1993, 1993.

[87] A. Kara and T. Rahman. Vibrational dynamics and thermodynamics of surfaces and nanostructures. *Surf. Sci. Rep.*, 56:159, 2005.

[88] S. van Dijken, G. Di Santo, and B. Poelsema. Influence of the deposition angle on the magnetic anisotropy in thin Co films on Cu(001). *Phys. Rev. B*, 63:104431, 2001.

[89] Y. Shim and J. G. Amar. Effects of shadowing in oblique-incidence metal (100) epitaxial growth. *Phys. Rev. Lett.*, 98:046103, 2007.

[90] A. Bogicevic, S. Ovesson, P. Hyldgaard, B. I. Lundqvist, H. Brune, and D. R. Jennison. Nature, strength, and consequences of indirect adsorbate interactions on metals. *Phys. Rev. Lett.*, 85:1910, 2000.

[91] T. Michely and J. Krug. *Islands, Mounds and Atoms.* Springer, 2004.

[92] J. Krug. On the shape of wedding cakes. *J. Stat. Phys.*, 87:505, 1997.

[93] M. Kalff, P. Smilauer, G. Comsa, and T. Michely. No coarsening in Pt(111) homoepitaxy. *Surf. Sci.*, 3:L447, 1999.

Dankwoord

Het is gelukt! Wederom heb ik een voor mij schijnbaar onmogelijke klus geklaard. Ik citeer het College van Promoties: "*... de voor uw promotie ingestelde promotiecommissie heeft beslist dat u door middel van uw proefschrift een zodanig bewijs van bekwaamheid tot het zelfstandig beoefenen van de wetenschap hebt geleverd ...*". Op 29 februari 2008 weten de mensen of ik echt Doctor ben geworden.

In mijn eentje had ik deze klus niet geklaard. Ik ben een heleboel mensen dankbaar voor het bereiken van mijn doel. Allemaal waren ze onmisbaar voor dit succes. Ik bedank ze allemaal in gedachte, enkele ga ik nu bedanken in woord.

Herbert, ik wil je als dagelijkse begeleider vooral bedanken voor je aanstekelijke enthousiasme voor het doen van onderzoek. Je was er vaak als de kippen bij als ik nieuwe resultaten had. Je was ook een lopende encyclopedie. Daarnaast bewonder ik je als de PR machine naar de wetenschappelijke buitenwereld voor mijn onderzoek wat zeker een positief effect had op de externe aandacht voor mijn onderzoek en de prijzen die ik gewonnen heb op conferenties.

Professor Bene, ik wil u als promotor bedanken voor het vertrouwen waarmee u het mogelijk maakte dat ik mij kon ontwikkelen tot Doctor. Door u ben ik kritischer gaan nadenken bij wat ik zeg en schrijf. Ik vond het altijd prettig dat ik mijn ei kwijt kon bij u (als de deur open stond); of het nu persoonlijk was of werkgerelateerd was, dat maakte niet uit.

Professor Talat Rahman and Dr. Kara Abdelkader showed me the real simulation world. The visits in Manhattan, Kansas, were a pleasure. Thanks.

Zonder technische staf geen experimentele opstelling. Vele uurtjes gingen zitten in het goed genoeg werkend krijgen van de opstelling met de veelzeggende naam "de

Kater". Geert, bedankt voor de elektronica kennis die we onder andere nodig hadden om "de Kater" te besturen. Hans, het blijven mooie trillings-isolatoren die je thuis in je vrije tijd hebt gemaakt. Herman, zonder jouw geen snelheidsselektor en geen hoge flux bron. Bedankt voor de buitengewoon hoge inzet tijdens de laatste fase in mijn onderzoek.

De experimentele opstelling had ook vele knoppen die bestuurd moesten worden. Een foute beslissing kan cathastrofale gevolgen hebben. Mischa, Agnes, Frank en Herbert bedankt voor het wegwijs worden in een goede bediening.

Dan moest er van alles worden ingeklopt in een computer en er was een server nodig voor al mijn simulaties. Dit was kats onmogelijk voor mij zonder de hulp van enkele slimme itc mensen: Gerard, Stefan en Teun. Bedankt.

Een tijd lang mocht ik genieten van een team van zeer slimme studenten. Tegelijkertijd werkten Teun, Frank en Tjeerd mee aan mijn onderzoek. Bedankt voor jullie team werk en natuurlijk mooie resultaten. Tjeerd, je hebt mij geholpen met de "condensatie regel", een essentieel element in het simulatie programma. Teun, speciaal bedankt voor het verbeteren van het simulatie programma en het opzetten van een server. Frank, bedankt voor het mee helpen sleutelen aan "de Kater" en de mooie resultaten die we ermee hebben gekregen.

Onderzoek doen is leuk. Schrijven daarentegen is niet mijn hobby en niet mijn sterkste kant. Veel steun heb ik gekregen van Esther, Agnes, Dennis, Herbert en Bene bij het schrijven. Nico Veer bedankt voor de Duits-Nederlands vertalingen.

Wat een geluk dat er een Rianne was. Bedankt voor alle secretariële ondersteuning.

Alle vakgroepgenoten in mijn afgelopen promotie periode wil ik bedanken voor hun gedeelde kennis, opbouwende kritiek, hun gezelligheid en hun aan Frits ter beschikking gestelde computers.

Soms krijg je een kater van "de Kater". Een kater moet je wegdrinken met bier. En gelukkig werd en wordt ik al jarenlang gesteund door een groep vrienden die zich Brak en/of Bracque noemen. Hun (onovertreffelijke) bier, hun gezelligheid, hun bemoedigingen en hun natuurkunde kennisnetwerk waren ook onmisbaar voor het halen van mijn doel.

Ik wil speciaal ook de clan Rabbering bedanken en natuurlijk Nathalie, en daarnaast mijn "schotland groep" en andere vrienden, voor hun monikkengeduld en hun altijd aanwezige steun. Jullie hebben samen met mij de last in zware tijden gedragen.